博士学位論文

Electrochemical and Thermal Investigation of Li-ion Secondary Cells Using Electrochemical Impedance Spectroscopy and Accelerating Rate Calorimetry

(電気化学インピーダンス測定と走査型断熱式熱量測定によるリチウムイオン二次電池の電気化学および熱的特性の研究)

長岡技術科学大学大学院工学研究科

エネルギー・環境工学専攻

Omar Samuel Mendoza Hernandez

Contents

Motivation:

Our planet is facing environmental problems and I want to contribute to the solution of these problems by developing technology that helps to keep a balance between comfort and nature. The increase of world population and urbanization can represent a threat to the global environment and a shortage of limited natural resources if appropriate measures are not taken.

The combination of natural sources of energy with energy storage devices is an excellent alternative to reduce the emissions generated by traditional power generation systems. Li-ion secondary cells have dominated the field of advanced power sources and have replaced the use of other batteries, particularly in the case of powering large applications such as electric vehicles (EV) or hybrid electric vehicles (HEV).

A wider spread use of EVs and HEVs depends on the development of Li-ion secondary cells. These cells require a long cycle and calendar life, high performance and safe operation. The safety of the cells should not be influenced by the degradation of these, but there are still some concerns regarding to the performance of degraded Li-ion cells.

This research studies the electrochemical and thermal properties of different types of Li-ion secondary cells with the aim of developing safe Li-ion cells with a long calendar life and high performance.

Preface:

In this work, the electrochemical and thermal properties of single Li-ion secondary cells are analyzed by using electrochemical impedance spectroscopy (EIS) and accelerating rate calorimetry (ARC). EIS is a nondestructive method that allows the in-situ analysis of electroactive materials of Li-ion cells. By carrying out EIS measurements at different temperatures and state of charges using Li-ion cells incorporating a reference electrode, kinetic parameters of Li-ion insertion/deinsertion reactions are analyzed. The thermal behavior of a Li-ion cell is dominated by exothermic reactions between the electrolyte and electroactive materials, the use of ARC allows to analyze the thermal behavior of these reactions. By using ARC, the thermal behavior of Li-ion cells using different cathode materials is analyzed at different state of charges, including over charge. Non-self-heating, self-heating and thermal runaway regions are identified as a function of temperature and state of charge.

Chapter 1 provides a general background for Li-ion secondary cells. It describes the development, configuration and materials for Li-ion cells. Electrochemical and accelerating rate calorimetry techniques used in research are explained in this chapter.

Chapter 2. The experimental methodology is described in this chapter.

Chapter 3 analyzes graphitized-carbon-based electrode (anode) reactions of Li-ion secondary cells incorporating a reference electrode are analyzed before and after cycling degradation by carrying out electrochemical impedance spectroscopy (EIS) measurements at different SOCs and temperatures.

Chapter 4 analyzes Li-ion insertion/deinsertion reactions of $LiCoO_2$ and $LiMn_2O_4$ cathode materials are analyzed by carrying out electrochemical impedance spectroscopy (EIS) measurements at different SOCs and temperatures. Kinetic parameters of the Li-ion insertion/deinsertion reactions are obtained and compared with crystal structural of $LiCoO_2$ and $LiMn_2O_4$ cathode materials.

Chapter 5 compares the thermal runaway behavior of two widely used cathode materials in commercial Li-ion cells, $LiCoO_2$ and $LiMn_2O_4$, at different state of charges including overcharge (120% SOC), using 18650 Li-ion cells and carrying out accelerating rate calorimetry measurements. In parallel with the calorimetry measurements, the internal resistance and open circuit voltage of the cells were monitored.

Chapter 6 analyzes the thermal runaway behavior of 18650 Li-ion cells before and after storage and cycling degradation at high temperatures. The thermal behavior of the cells is analyzed using accelerating rate calorimetry. Non-self-heating, self-heating and thermal runaway regions of the cells as a function of state of charge and temperature are identified and compared among the cells.

Chapter 7 compares the thermal behavior of small and large laminated Li-ion cells using accelerating rate calorimetry.

Chapter 8. This chapter describes the general conclusions of this research.

Chapter 1 “Introduction”

1.1 Lithium-ion secondary cells

A battery stores chemical energy that is converted into external electrical energy on discharge. In a rechargeable (secondary) cell, the internal chemical energy is restored on charge by the application of external electrical energy, which means that the chemical reactions inside the battery must be reversible [1].

Research into lithium cells began in the 1950s when it was noticed that Li-metal was stable in a number of non-aqueous electrolytes such as fused salts, liquid SO_2 or organic electrolytes such as $LiClO_4$ in propylene carbonate. The formation of a passivation layer that prevents the direct chemical reaction between lithium metal and the electrolyte but still allows for ionic transport is the origin of the stability of non-aqueous electrolytes [2-3].

The concept of lithium-ion cells (or lithium rocking-chair cells) was proposed in the late 1970s, when different intercalation compounds were used as positive and negative electrodes, in the so-called rocking chair battery the lithium ions being transferred from one side to the other [4]. This concept has gained renewed attention following the success of Japanese industries. Exploiting the idea for large scale production, Sony Energytec Inc., commercialized in June 1991 a Li-ion battery including a $LiCoO_2$ cathode and a non-graphitic carbon anode. Li-ion cells have been marketed by several battery companies in the word [3].

1.1.1 Development of Lithium-ion secondary cells

Lithium-metal anode primary batteries based on nonaqueous electrolytes such as propylene carbonate-lithium perchlorate and lithium negative electrodes were developed in the early 1970s, with Matsushita introducing a lithium-carbon monofluoride (Li-CF_x) primary cell in 1973, followed by Sanyo which commercialized lithium-manganese dioxide primary cells (Li-MnO_2) in 1975. These cells were used for LED fishing floats, cameras, and memory backup applications. A strong research effort then was mounted to convert lithium primary cells into rechargeable cell with high energy density. In the 1970s and 1980s most efforts concentrated on the development of inorganic cathode compounds [1-4].

The early rechargeable lithium cells were plagued with safety problems caused by the tendency of lithium-metal anodes to form dendrites and power deposits on recharging. In 1989, Moli Energy had the heat generation related to lithium metal in an AA-size cell. There was a shift to Li-Al alloy anode for improving the safety in coin cells [4]. However, the metallurgy of the alloy proved unacceptable for wound AA-size cells. The lithium metal rechargeable cells now are restricted mainly to small capacity coin cells.

Since lithium metal constituted a safety problem, attention shifted to the use of a lithium intercalation material as an anode. Ikeda of Sanyo was the first to patent an intercalation material in an organic solvent such as graphite in June 1981. Kuribayashi and Yoshino developed a new cell design using an intercalation carbon anode and $LiCoO_2$ cathode and filed patents worldwide. Using a pilot plant developed for rechargeable Li-MnO_2 cells, Sony Energytec Inc., began to produce commercials cells (called the Li-Ion Battery). They also introduced an electronic circuitry to control the

charge-discharge, the use of a current interrupt device to interrupt current flow on buildup of excessive internal cell pressure, and the use of a shut-down polymer separator [5].

The name “lithium-ion” now is accepted by the battery community worldwide, although there is no lithium metal in the cell. However, very often lithium metal deposition occurs during charging with the graphite anode and it may cause the many troubles on the lithium ion batteries. Both electrodes operate by intercalation of lithium ions into the structure of the active materials.

Figure 1.1 describes the increase in capacity of the cylindrical 18650 cell (18 mm in diameter and 65 mm long) from 1992 to 2006. The early lithium ion batteries had a capacity of 800 mAh and end of charge of 4.1 V. The initial cells used hard carbon anode materials which has a capacity of about 200 mAh/g, and $LiCoO_2$ has a capacity of nearly 130 mAh/g due to 4.1 V charging voltage. The early lithium ion cells used propylene carbonate based electrolyte. The energy density of lithium ion cells improved rapidly and increased on average by 10% per year and has approached 2.6 Ah in 2005. Responding to pressure from device manufactures, the cell capacity improved through engineering and the introduction of graphite anodes, improved $LiCoO_2$-based cathode materials, and the introduction of graphite additives [2].

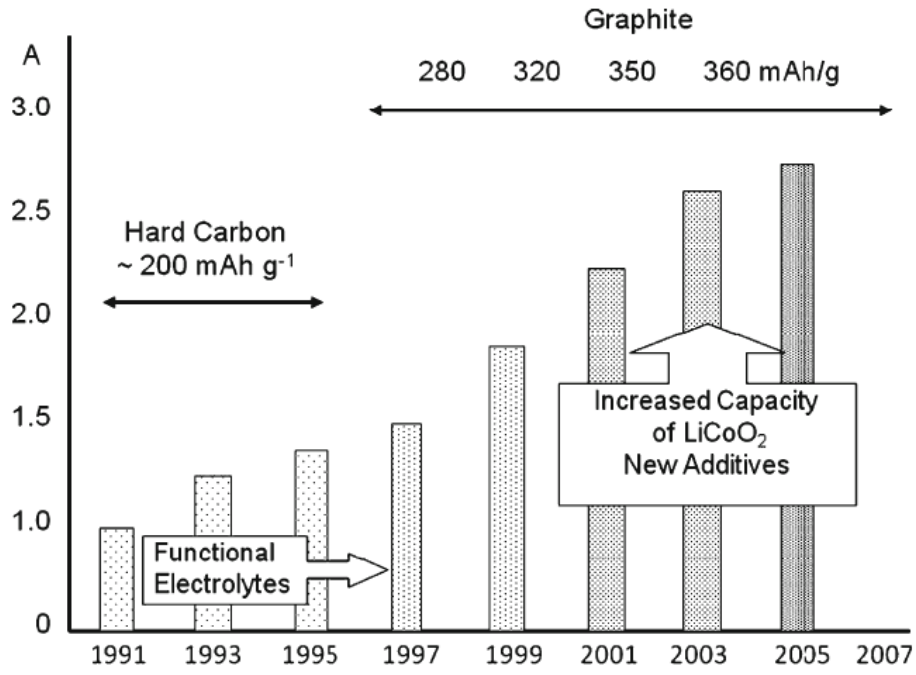

Fig. 1.1 Capacity increase resulting from changes in materials and charging procedures.

Nowadays, the lithium ion secondary cells are considered as one of the most promising energy storage devices for many electrical applications. However, the commercialized cells have to be much improved in order to satisfy the future challenging requirements.

1.1.2 Configuration of Lithium-ion secondary cells

A lithium ion rechargeable cell, which is also known as a swing battery or rocking chair battery, since two way movements of lithium ions between anode and cathode through the electrolyte occurs during charge and discharge processes. The mainly components of lithium ion cells are the negative electrode, positive electrode, electrolyte and the separator.

As it is shown in Fig. 1.2, during charging under applied voltage, deintercalation of some of the lithium ions from the cathode ($LiCoO_2$) into electrolyte

liquid occurs and simultaneously and equivalent amount of lithium ions from the electrolyte intercalate into the carbon anodes. During discharge, the reverse reaction proceeds spontaneously. On both charge and discharge, charge compensation occurs through the external circuit.

Anode reaction: $Li(C) \rightleftharpoons Li^+ + e^-$

Cathode reaction: $Li^+ + e^- + CoO_2 \rightleftharpoons LiCoO_2$

Total reaction: $Li(C) + CoO_2 \underset{charge}{\overset{discharge}{\rightleftharpoons}} LiCoO_2$

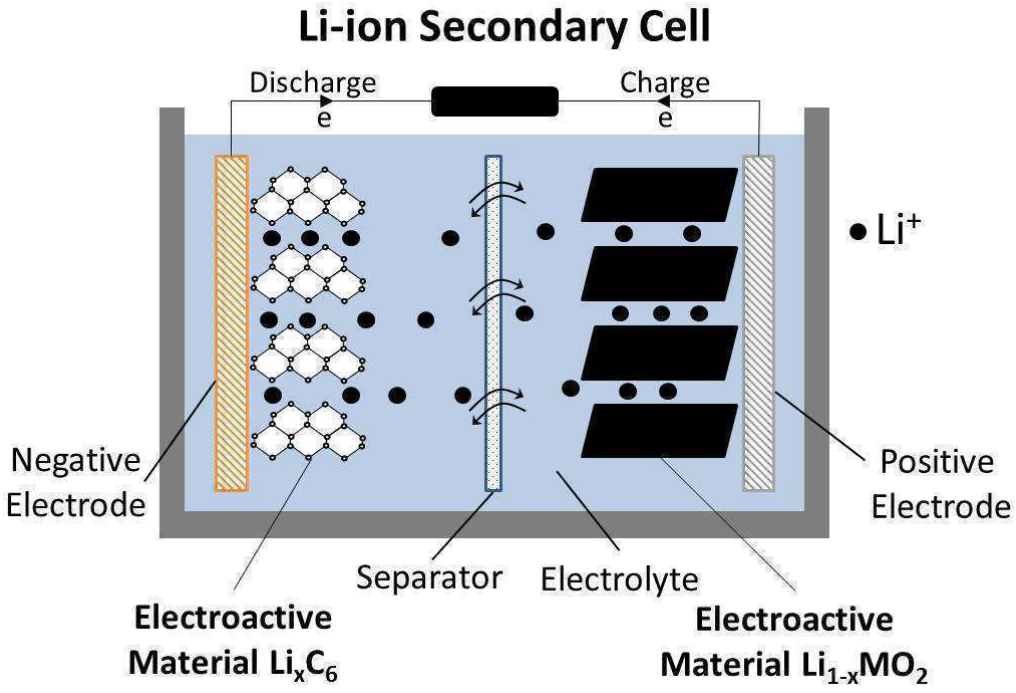

Fig. 1.2 Principle of lithium ion secondary cell.

1.1.3 Materials of Lithium-ion secondary cells

Intercalation compounds have been using in lithium ion secondary cells marketed now, these compounds have shown excellent cycle life and usually no morphology modifications are observed.

Table 1.1 Electrochemical equivalents of negative and positive electrodes used in lithium ion secondary cells.

Material	Molar weight	Density (g/cm^3)	Specific capacity (mAh/g)
	Negative electrodes		
Li_xC_6 (c)	72.06	2.0	186
Li_xC_6 (g)	72.06	2.25	372
WO_2	215.8	12.11	124
MoO_2	127.9	6.47	105
	Positive electrodes		
$LiMn_2O_4$	180.8	5.16	148
$LiCoO_2$	97.9	4.28	137
$LiNiO_2$	97.6	4.78	192

Table 1.1 gives some examples of negative and positive electrode materials which are used in lithium ion secondary cells. There are three promising cathode materials for lithium ion secondary cells: $LiCoO_2$, $LiNiO_2$ and $LiMn_2O_4$. They are lithiated materials synthesized in the discharge state. These compounds are air and water stable and exhibit potential at about 4 V vs. Li/Li^+. $LiCoO_2$ and $LiNiO_2$ have a rhombohedral structure, shown in Fig. 1.3, the rhombohedral unit cell has a geometric feature that has three axes of an equal length, and that each angle between any two axes is the same [6-7]. Usually, this cell unit is expressed by the hexagonal structure. $LiMn_2O_4$ has a spinel structure and can be viewed as a combination of the rock salt and zinc blende structure, Fig. 1.4.

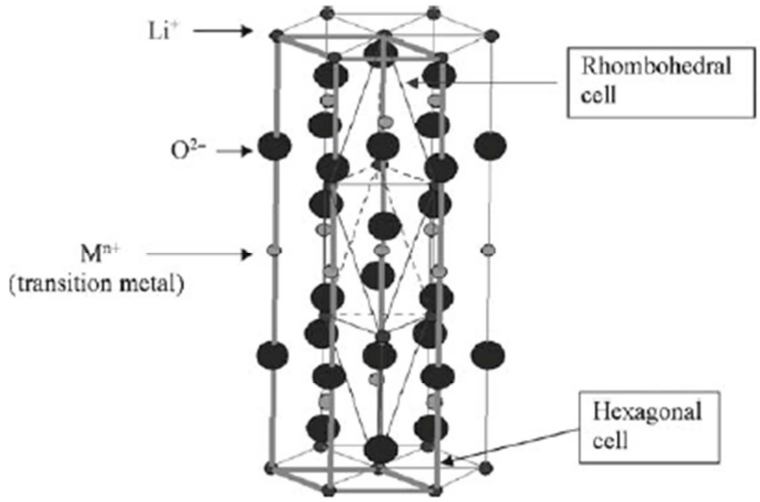

Fig. 1.3 Relation between rhombohedral cell and hexagonal cell.

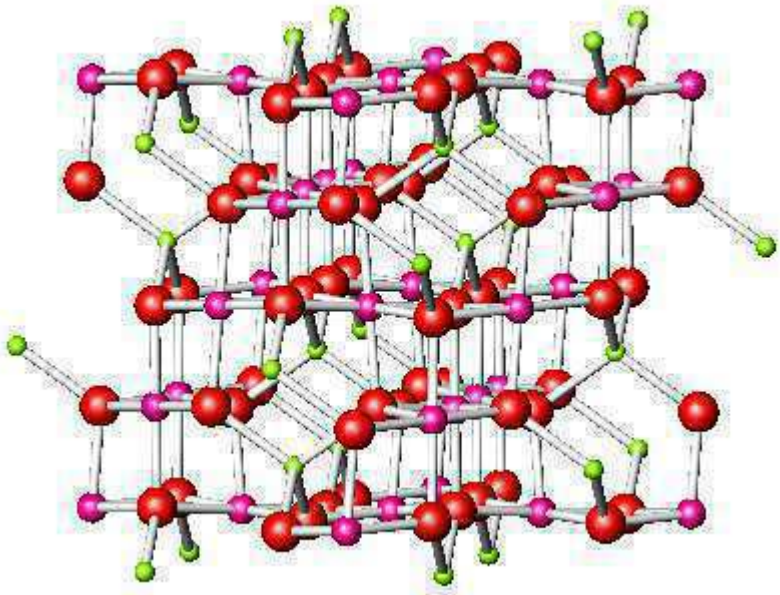

Fig. 1.4 $LiMn_2O_4$ structure. The green atoms correspond to lithium, the pink atoms to manganese and the red atoms to oxygen.

This spinel compound exhibits a high conductive potential, this is attributed to the multiple oxidation states of manganese. The $LiMn_2O_4$ structure consists of manganese atoms octahedrally coordinated to six oxygens and lithium atoms tetrahedrally coordinated to four oxigens [8].

One of the most common anode materials used in lithium ion secondary cells are carbonaceous materials. Graphite is the most thermodynamically stable form of carbon structure. The graphite possess many advantages, such as a good thermal and electrical conductivities, low density, adequate corrosion resistance, low thermal expansion, low elasticity, low cost and high purity. Carbonaceous materials are generally constituted from repeating sp^2 bonding C-C atoms, which construct the planar hexagonal networks of C atoms called graphene layers. Each graphene layer can be considered to be a superconjugated macromolecule. Van der Waals force stacks these sheets into ordered structures. The crystal structure of graphite is shown in Fig. 1.5 [9]. Insertion and extraction intercalation reactions of lithium atoms into graphite occur at potential of 1.0 – 0 V vs. Li/Li^+, according to the follow reaction:

$$6\,C + xLi^+ + xe^- \underset{\longleftarrow}{\longrightarrow} Li_xC_6 \quad [0<x<1]$$

The electrolyte of a lithium ion secondary cell can be a non-aqueous liquid electrolyte, a polymer or a solid fast ionic conductor. The electrolyte has to have a high ionic conductivity over a wide range of temperature and an electrochemical stability in the voltage range of 0-5 V vs. Li/Li^+. A typical electrolyte consists of a lithium salt dissolved in aprotic solvent mixture [10-12].

The separator in a lithium ion secondary cell is typically a thin microporous polypropylene film. It prevents the electrodes from shorting directly or through Li microdentrite growth on overcharge and it also serves as a thermal shut down safety device. When heated above 150℃ the separator melts and its pores close, thus preventing current flow and thermal runaway [13-15].

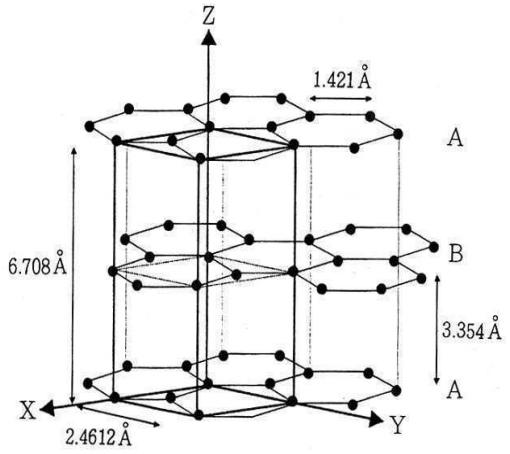

Fig. 1.5 Crystal structure of graphite.

1.2 Accelerating rate calorimeter

The accelerating rate calorimeter (ARC) is an adiabatic calorimeter for hazard evaluation of reactive chemicals. Its primary function is to permit a sample to undergo thermal decomposition due to self-heating while recording the time, temperature and pressure relationships of the runaway process.

The key factor in the design and construction of the ARC is the maintenance of near perfect adiabatic conditions. To accomplish this, the sample holder is placed inside a nickel-plated, copper jacket that is equipped with thermocouples and heating elements to produce a uniform jacket temperature and to maintain zero temperature difference between the sample holder and jacket [16].

The ARC is also equipped with a means of heating which is used to automatically step the temperature up to a value where the self-heat rate is detectable. Once a self-heat rate is detected above a pre-selected threshold the sample is automatically maintained under adiabatic conditions for the duration of the exotherm. A pressure sensor permits the measurement of the sample pressure. From recorded data, various relationships may be obtained such as: adiabatic temperature rise, temperature of maximum self-heat rate, time to maximum self-heat rate, self-heat rate vs. temperature, pressure vs. temperature, pressure rate vs. temperature and pressure rate vs. temperature rate.

Further post-run calculations can then be used to make predictions about the behavior of the isolated chemical as well as the behavior of the chemical in other environments. In addition, the various kinetic parameters which describe the decomposition reaction may be determined. For normal analyses the ARC is fully automated, and for special analysis needs, manual control of the ARC is possible.

1.3 Electrochemical measurements

1.3.1 Electrochemical impedance spectroscopy

By carrying out the electrochemical impedance spectroscopy (EIS) measurements, it is possible to record spectral analysis on the lithium ion secondary cells electrodes by using an alternating current signal of a wide range of frequency. The impedance spectrum of a lithium ion secondary cell appears in the frequency region of 100 kHz – 0.1 kHz, which can be analyzed quantitatively according to an equivalent circuit. The analysis of the impedance spectra changes is useful to investigate the electrode reaction processes, and by using a lithium ion secondary cell with a reference

electrode it is possible to study the anode and cathode reactions in a separate way [17].

The shutdown behavior of the cell separator is investigated by measuring the cell impedance changes, at 1 kHz, dependent on temperature.

1.3.2 Current-potential curves (d*Q*/d*E* vs. *E* curves)

The analysis of the electrochemical measurements of the positive and negative electrode materials is very interesting. Conventionally, the reactions of the electrode materials using a single particle measurement method and electrostatic spray deposition (ESD) have been carried out ex-situ. However, these methods do not necessarily measure the reactions that are occurring in-situ. In particular, it is difficult to evaluate and analyze the degradation of the cell under real conditions using a half-cell. The in-situ measurements mean that the electrochemical measurements are conducted for the Li-ion cell without any disassembling procedure. For these proposes, the use of a cell with a reference electrode is essential. The use of these types of cells is attractive in order to separately analyze the positive and negative electrode reactions, thus these reaction analyses can be carried out using techniques such as cyclic voltammetry, d*Q*/d*E* vs. *E* curves, chronopotentiometry, etc.

Consistent with the above discussion, using a lithium ion secondary cell incorporating a reference electrode, the d*Q*/d*E* vs. *E* curves of the anode and cathode active materials can be obtained and compared to the conventional half-cell that have been reported.

References

[1] Jasinski, R. (1967) *High-energy Batteries*, Plenum, New York.

[2] M. Yoshio, R. J. Brodd and A. Kozawa (2009) Lithium-ion Batteries, *Science and Technologies*, Springer.

[3] C. R. Park (2010) Next Generation Lithium ion Batteries for Electrical Vehicles, In-Tech.

[4] G. A. Narzri, G. Pistoia (2009), Lithium Batteries Science and Technology, Springer.

[5] C. Julien and Z. Stoynov. (1999) Materials for Lithium-ion Batteries, Springer.

[6] J. N. Reimers, J. R. Dahn, *J. Electrochem. Soc.*, 139, 2091 (1992).

[7] J. N. Reimers, J. R. Dahn, U. von Sacken, *J. Electrochem. Soc.*, 140, 2752 (1993).

[8] T. Ohzuku, M. Kitagawa, T. Hirai, *J. Electrochem. Soc.*, 137, 769 (1990).

[9] Z. Ogumi, M. Inaba, *Bull. Chem. Soc. Jpn.*, 71, 521 (1998).

[10] E. Peled, *J. Elecrochem. Soc.* 126, 2047 (1979).

[11] J. O. Besenhard, M. Winter, J. Yang, W. Biberacher, *J. Power Sources*, 54, 228 (1995)

[12] M. Winter, G. H. Wrodnigg, J. O. Besenhard, W. Biberacher, P. Novak, *J. Electrochem. Soc.* 146, 470 (1999).

[13] G. Venugopal, *J. Power Sources*, 101, 231 (2001).

[14] F. C. Laman, M. A. Gee, J. Denovan, *J. Electrochem. Soc.* 140, L51 (1993).

[15] A. J. Bradley and R. E. White, *J. Power Sources*, 70, 48 (1998).

[16] Arthur D. Little Inc. Accelerating rate calorimeter operation, maintenance and parts manual.

[17] A. J. Bard and L. R. Faulkner (2001), *Electrochemical Methods Fundamentals and applications.*

Chapter 2 “Experimental Methodology”

2.1 Lithium ion secondary cell charging/discharging methods

Lithium ion secondary cells were charged/discharged using a battery charging/discharging equipment, PFX2011 manufactured by KIKUSUI. The states of charge (SOC) adjustments were carried using the same equipment. Charging/discharging tests and SOC adjustments were done at 25 °C.

2.1.1 Charging

Normally, the charging tests of the lithium ion secondary cells are carried out using a constant-current constant-voltage (CC/CV) method, where a constant current rate is applied to the cell under charge until the maximum voltage is reached. Li-ion cells charging conditions are described in the corresponding chapter.

2.1. 2 Discharging

The discharging tests of the lithium ion secondary cells are carried out using a constant current (CC) method, where the cell is discharged at a constant current rate until reaches the lower voltage value. Li-ion cell discharging conditions are described in the corresponding chapter.

2.2 Electrochemical measurements

2.2.1 Electrochemical impedance spectroscopy

Electrochemical impedance spectroscopy (EIS) is a precise method for studying electrochemical kinetics. The impedance is defined by the term of the ratio between an input voltage and alternating current. EIS studies the system response to the application of a periodic small amplitude ac signal, the measurements are carried out at different ac frequencies. The analysis of the system response contains information about

the interface and reactions taking place there.

The impedance is divided into real and imaginary components, according to the following equation:

$$Z = Z' + jZ''$$

The real part, Z', is plotted on the X axis and the imaginary part, Z'', on the Y axis. The resulting complex plane is known as a Nyquist plot. Notice that in this plot, the Y axis is negative and that each point on the Nyquist plot is the impedance at one frequency. The EIS data are commonly analyzed by fitting them to an equivalent circuit model. Most of the circuit elements in the model are common electrical elements such as resistors, capacitors and inductors. To be useful, the elements in the model must have a basis in the physical electrochemistry of the system. The figures 2.1 and 2.2 show an example of an impedance spectrum (Nyquist plot) and an equivalent circuit, respectively.

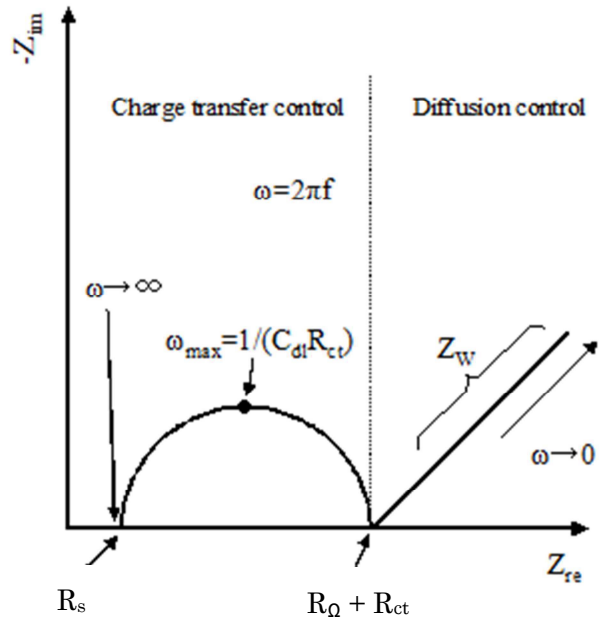

Fig. 2.1 Example of an impedance spectrum.

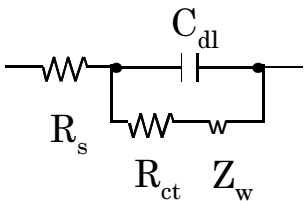

Fig. 2.2 Equivalent circuit example.

R_s corresponds to the electrolyte resistance, C_{dl} represents a double layer capacitance that exists at the interface between an electrode and its surrounding electrolyte. R_{ct} and Z_w are components of a Faraday impedance, R_{ct} corresponds to the charge transfer resistance in the electrode interface and Z_w is known as Warburg impedance that is created by a diffusion. Each component of the equivalent circuit is described in the impedance spectrum, Fig. 2.1. The electrochemical kinetics is studied by analyzing the spectra changes and correlating the impedance data with the corresponding equivalent circuit.

2.2.2 EIS measurements of Li-ion Secondary Cells Incorporating a Reference Electrode

By using a lithium ion secondary cell incorporating a reference electrode, it is possible to analyze the anode and cathode reactions of the cell in a separate way. A lot of phenomena take place when the lithium ion is inserting into the active materials. In order to analyze these phenomena, EIS measurements are carried out using Li-ion cells incorporating a reference electrode at different SOCs and temperatures.

EIS measurements are carried out using a frequency response analyzer (Solartron 1260) in combination with a potentiostat (Solartron, 1286 Electrochemical Interface), shown in Fig. 2.3. The applied frequency range and AC voltage were 100

kHz-10 mHz and 5 mV_{rms} respectively. Before recording the EIS measurements, the cell was charged to the desired SOC using a battery charging/discharging equipment (KIKUSUI, PFX2011). The cell was tested inside a constant temperature chamber (FL414P). The tests were carried out at 20, 30, 45 and 60 °C, there was a waiting time of 1 h after setting each temperature. In order to obtain the spectra between anode-reference and cathode-reference, the connections of the potentiostat were configured in a special way. The spectra obtained were fitted according to an equivalent circuit.

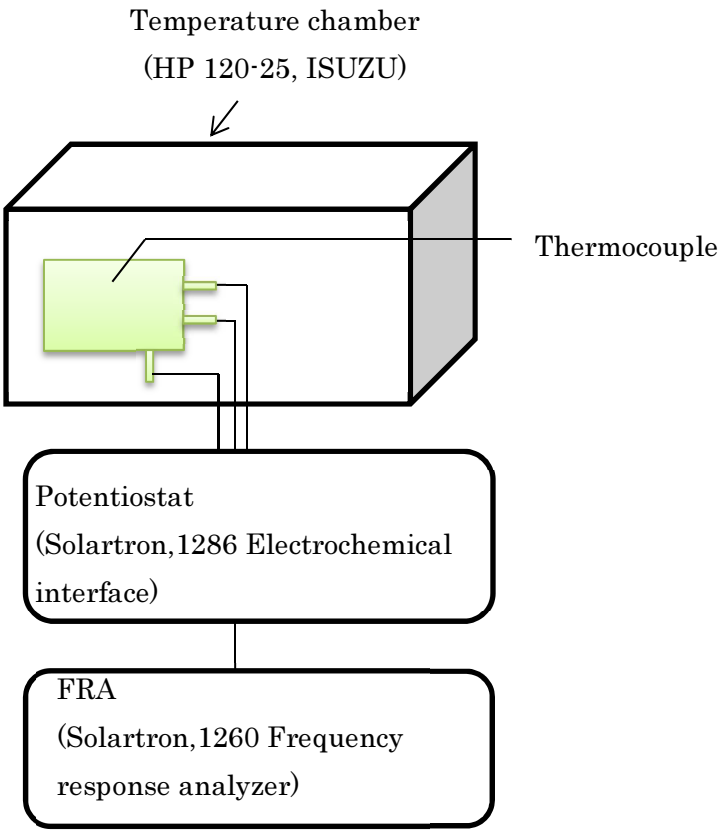

Fig. 2.3 Schematic illustration of the potentiostat in combination with a frequency response analyzer and temperature chamber.

In order to get the cathode and anode spectra in a separate way, the potentiostat connections have to be configured in certain ways, shown in Fig. 2.4.

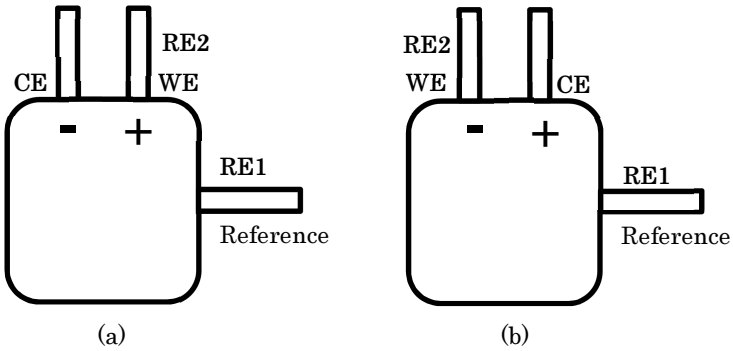

Fig. 2.4 Potentiostat connections (a) cathode configuration (b) anode configuration.

2.3 Accelerating rate calorimeter (ARC) measurements

By using the ARC is possible to identify and analyze the exothermic reactions of lithium ion secondary cells, as well as analyze the temperature dependency on electrochemical measurements.

Fig. 2.5 Accelerating rate calorimeter.

2.3.1 Thermal runway tests

Thermal runaway tests are carried out inside the ARC. The cells were placed inside the ARC cavity, being first charge to the desired SOC, as seen in Fig. 2.6.

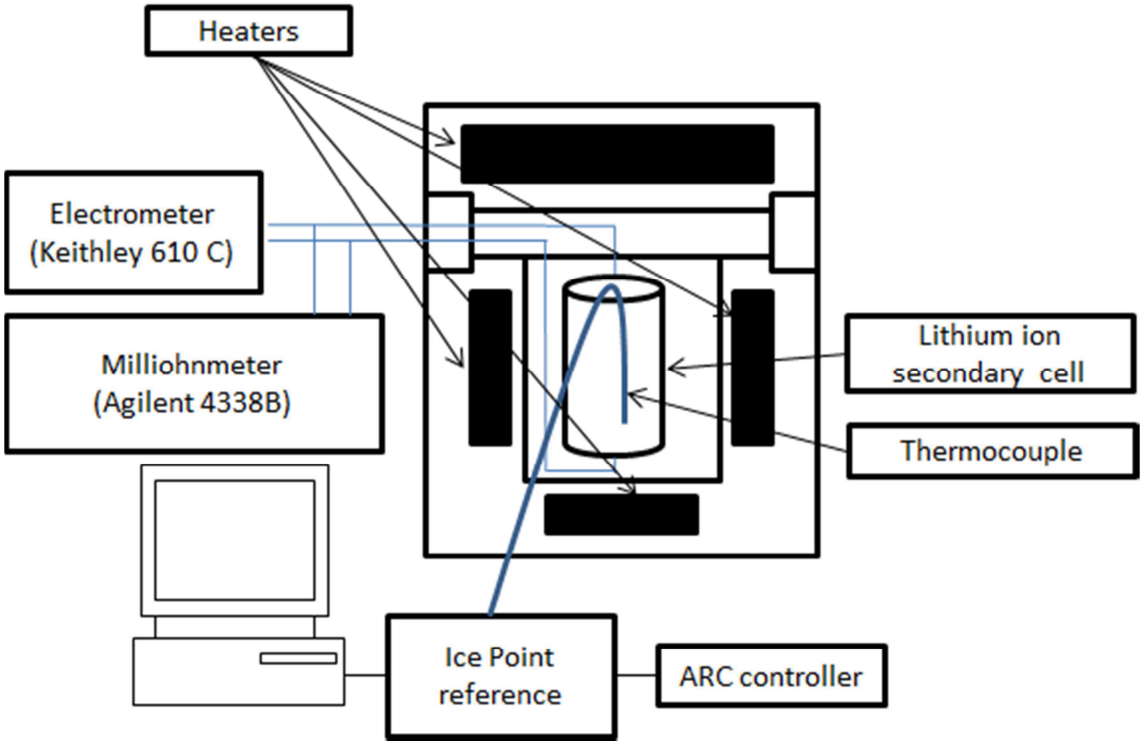

Fig.2.6 Schematic diagram of ARC.

The temperature inside the ARC was raised according to a method called Heat-Wait-Search mode. During the heating mode, ARC interior is heating up until reach the target temperature. In the wait mode, there is a waiting period of 30 min. In the search mode, if the heating rate of the cell is greater than 0.05 °C per minute, it is considered an indication of the onset of an exothermic reaction (self-heating). When the self-heating is observed, the ARC shuts down the heating and tracks the cell temperature until the end of the thermal runaway process. The thermal runaway analysis

is carried out until the cell surface temperature reached 200 °C. Besides, the open circuit voltage (OCV) was measured using an electrometer (HE-104A, HOKUTO DENCO) connected to a multimeter (KEITHLEY 2100) and the data were recorded by a KEITHLEY data acquisition software. The internal resistance of the cells was measured with a milliohnmeter (Agilent 4338B), the data were recorded by a program developed in Agilent VEE Pro 9.3.

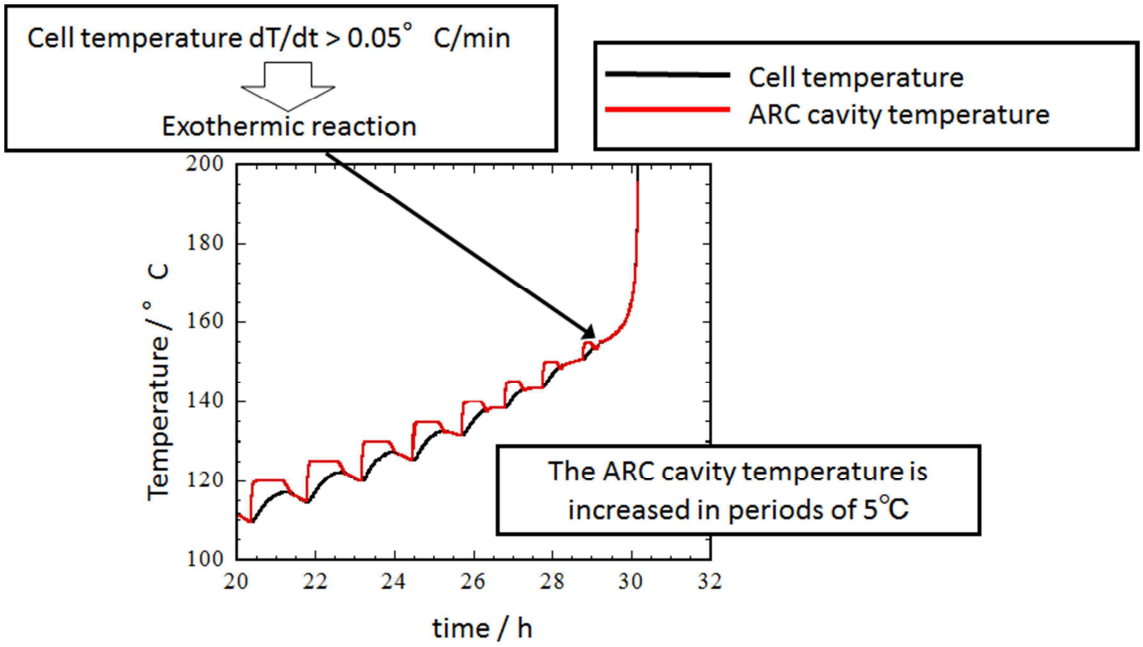

Fig. 2.7 ARC Heat-Wait-Search mode.

2.4 Lithium ion secondary cell chronopotentiometric measurements

A Li-ion cell incorporating a reference electrode was placed inside a constant temperature chamber (HP120-25, ISUZU), the temperature was fixed at 20 °C. In order to monitor the potential changes of the cathode and anode electrodes during charging and discharging, two electrometers and two multimeters were connected to electrodes, as is shown in Fig. 2.8.

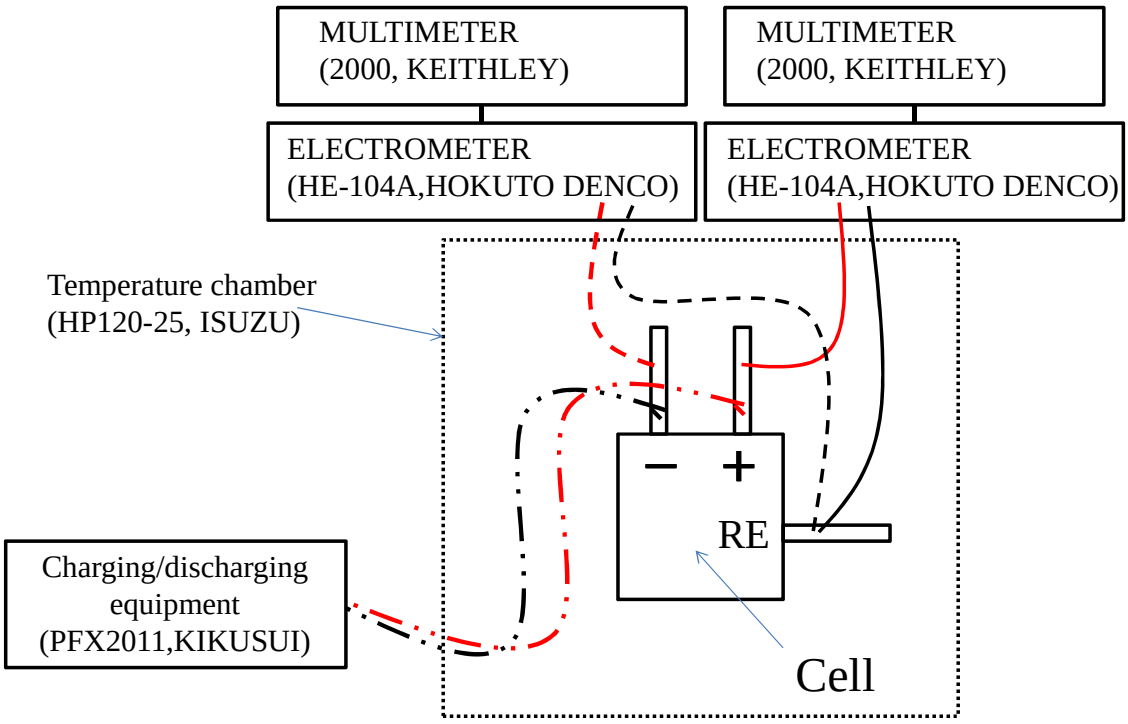

Fig. 2.8 Schematic diagram of the equipment used for recording choropotentiometric tests.

Before recording the chronopotentiometric measurements, the cell was cycled using a CC/CV and CC methods, in order to determine the cell capacity. After obtaining the capacity of the cell *C*, a constant current charging and discharging test was carried out. The charging and discharging conditions were set at 0.2 C current rates, using the charging/discharging battery equipment (PFX2011, KIKUSUI). During the charging and discharging, the potential changes of the cathode and anode were monitored using the electrometers and multimeters. The data were recorded using a KEITHLEY data acquisition software. By plotting the potential (*E*) and the capacity (*Q*) vs. time, dQ/dE vs. E curves were obtained.

2.5 Types of lithium ion secondary cells tested

Different types of lithium ion secondary cells were used in the tests. Li-ion laminated cells incorporating a reference electrode manufactured by ENAX Co., Ltd; 18650 and laminated Li-ion secondary cells manufactured by Shin-kobe Electric Machinery Co., Ltd; 18650 Li-ion cells manufactured by Panasonic. The details of each cell are shown in the tables 2.1-2.4.

Table 2.1 ENAX Co Li-ion cells incorporating a reference electrode.

	LCO cell	**LMO cell**
Cathode material	$LiCoO_2$-based	$LiMn_2O_4$-based
Anode material	Graphite-based	Graphite-based
Reference electrode material	Lithium foil	Lithium foil
Electrolyte	1 M $LiPF_6$ Ethylene carbonate : Diethyl carbonate = 1:1	1 M $LiPF_6$ Ethylene carbonate : Diethyl carbonate = 1:1
Dimensions (mm)	65 x 70	65 x 70
Capacity (mAh)	20	20

Fig. 2.9 Li-ion cell incorporating a reference electrode.

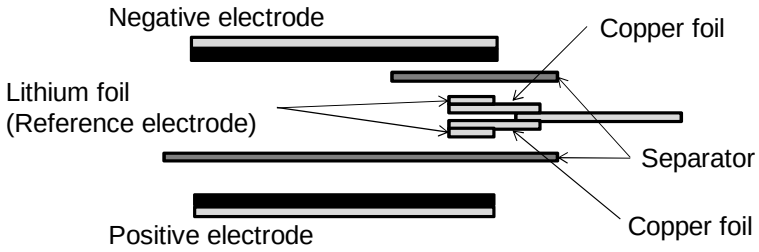

Fig. 2.10 A schematic diagram of a Li-ion cell incorporating a reference electrode.

Table 2.2 Shin-kobe Electric Machinery 18650 Li- ion secondary cells.

	LCO-Gr cell	**LMO-Gr cell**
Cathode material	$LiCoO_2$-based	$LiMn_2O_4$-based
Anode material	Graphite-based	Graphite-based
Dimensions (mm)	18 x 65	18 x 65
Capacity (mAh)	854	739

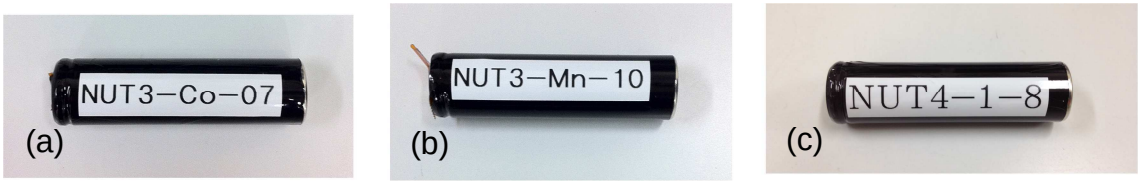

Fig. 2.11 18650 lithium ion secondary cells (a) LCO-Gr cell (b) LMO-Gr cell (c) LMO-Gr cell with anti-flammable agent.

Table 2.3 Shin-kobe Electric Machinery Laminated Li- ion secondary cells.

	LCO-Gr cell	**LCO-Gr cell**
Cathode material	$LiCoO_2$-based	$LiCoO_2$-based
Anode material	Graphite-based	Graphite-based
Dimensions (mm)	30 x 45	30 x 45
Capacity (mAh)	30	700

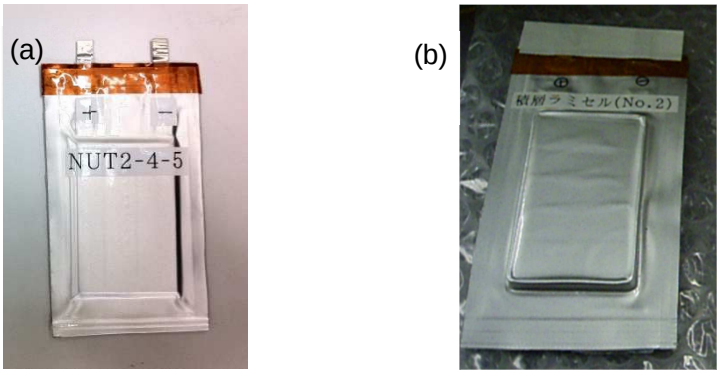

Fig. 2.12 Shin-kobe Electric Machinery 30 mAh (a) and 700 mAh (b) Laminated Li- ion secondary cells.

Table 2.4 Panasonic 18650 Li- ion secondary cells.

	Panasonic LCO
Cathode material	$LiCoO_2$-based + additives
Anode material	Graphite-based
Dimensions (mm)	18 x 65
Capacity (mAh)	2550

Fig. 2.13 Panasonic Li-ion secondary cell

References

[1] E. Barsoukov and J. R. Macdonald (2005) *Impedance Spectroscopy Theory, Experiment and Applications.*

[2] C. Julien and Z. Stoynov. (1999) *Materials for Lithium-ion Batteries.*

[3] H. Maleki, Jaosn N. Howard, J. Power Sources **160** (2006).

Chapter 3 “Kinetic Analysis of Graphitized-Carbon-Based Electrode Reactions in Lithium-ion Secondary Cells Before and After Cycling Degradation”

3.1 Introduction

Electroactive materials play an important role in cell performance, but, when a Li-ion is inserted into an electroactive material many reactions take place [1]. The crystal structure of the electroactive materials tends to change with the state of charge (SOC) of the cell, and the resulting changes affect the Li-ion insertion/deinsertion reactions [2-4]. Since the analysis of the electroactive materials is essential to design Li-ion cells with high performance, the techniques for evaluating the reactions of the electroactive materials are extremely important. Many efforts have been made to analyze the process of Li-ion insertion into electroactive materials using techniques such as XRD, cyclic voltammetry and single particle voltammetry [5-8]. However, these studies have been carried out using half-cells, and did not necessarily measure the reactions that are occurring in situ. Therefore, the development of a method that allows the in-situ analysis of the electroactive material reactions of a Li-ion cell is necessary, and is crucial to the analysis of the dependence of the electroactive material reactions on the SOC. For that purpose, the use of a Li-ion cell with a reference electrode is very helpful to analyze the positive and negative electrode reactions, separately.

Electrochemical impedance spectroscopy (EIS) is an in-situ and non-destructive method that allows the analysis of the electrode reactions of a Li-ion cell [9, 10]. Some kinetic studies of the characterization of the electrochemical properties of Li-ion secondary cell electrodes have been reported, where the Li-ion insertion/deinsertion reactions are analyzed at different SOCs [11-18]. But, these studies were carried out using half-cells and other special cells that do not essentially measure

the reactions that are occurring in situ.

In this work, the term “Li-ion secondary cell incorporating a reference electrode” refers to a sealed Li-ion cell that contains a positive electrode, a negative electrode and a reference electrode. The use of these cells allows in situ analysis of the interfaces between the electroactive materials and electrolyte in a separate way. So far, a few EIS studies that use Li-ion secondary cells incorporating a reference electrode are reported. M. Dolle et al., carried out EIS using a Li-ion secondary cell incorporating a reference electrode, they compared the impedance measurements of the electroactive materials with the impedance measurements of the full cell, validating the use of a Li-ion cell incorporating a reference electrode to analyze the electroactive materials in a separate way [19]. J. Y. Song et al., carried out EIS measurements using half-cells and a Li-ion cell incorporating a reference electrode and compared the results among the cells [20]. However, these works did not analyze the kinetic of the electroactive material reactions and their dependency on the state of charge.

In this chapter the graphitized-carbon-based electrode (anode) reactions of Li-ion secondary cells incorporating a reference electrode are analyzed before and after cycling degradation by carrying out electrochemical impedance spectroscopy (EIS) measurements at different SOCs and temperatures. By recording EIS measurements at different temperatures and SOCs, it is possible to analyze the kinetic of the anode reactions and the dependency of these on the SOC. To analyze the electrochemical behavior of the process of the Li-ion insertion/deinsertion into a graphitized carbon electrode, and to evaluate how the structural changes of graphitized carbon affect the Li-ion insertion/deinsertion process, the kinetic behavior of the anode reactions are compared with the anode dQ/dE vs. E curves.

3.2 Experimental methodology

3.2.1 Cell specifications

We tested a laminated lithium ion secondary cell containing a reference electrode. A schematic illustration of the cell is shown in Fig. 3.1. The cell consists of a negative electrode, a separator, a reference electrode, and a positive electrode. The size and position of the reference electrode were optimized so that it does not affect the charge and discharge performance of the cell. This cell used lithium cobalt oxide and graphitized carbon as the cathode and anode materials, respectively. The positive electrode consists of a mixture of an active material, an electroconductive material, and a binder resin, at a weight ratio of 90:3:7. The negative electrode consists of a mixture of an active material and a binder resin, at a weight ratio of 90:10. The capacities of the anode and cathode active materials were 1520 and 1200 mAh cm^{-3}, respectively. Lithium foil was used as the reference electrode, which was inserted between the positive and negative electrodes. The electrolyte contained 1 mol dm^{-3} $LiPF_6$, the solvent was ethylene carbonate: diethyl carbonate = 7:3 (volume), and the size of the cell electrodes was 46 mm × 46 mm (including the laminate package). The capacity of this lithium ion secondary cell with the reference electrode was 20 mAh.

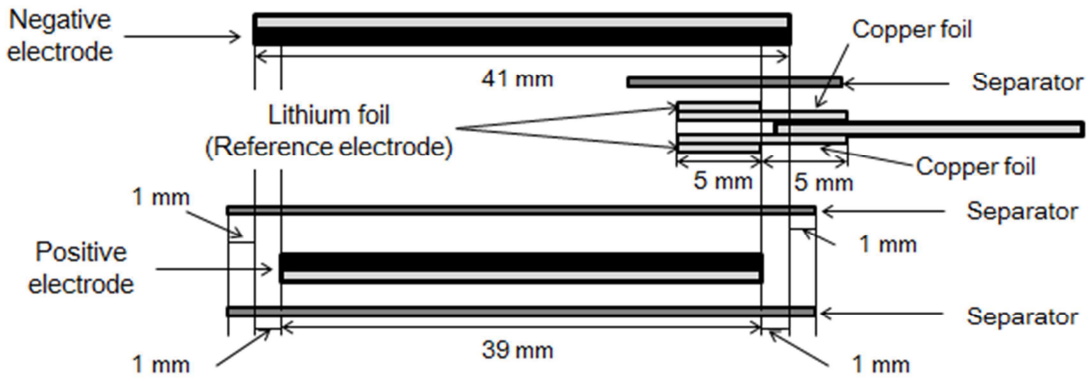

Fig. 3.1 Schematic illustration of a Li-ion secondary cell incorporating a reference electrode.

3.2.2 Cycling degradation

A Li-ion secondary cell incorporating a reference electrode was charged and discharged in a thermostatic chamber (ETAC, FL414P) at 35 °C. The cell was charged following a constant current / constant voltage process with a charging current of 10 mA, maximum voltage 4.2 V and a constant voltage time of 1 h. The cell was discharged to 25% depth of discharge (DOD) following a constant current process with a discharging current of 10 mA. The total charging/discharging cycles were 94.

3.2.3 Electrochemical Impedance Spectroscopy measurements

Electrochemical impedance spectroscopy (EIS) measurements were carried out using a frequency response analyzer (Solartron 1260) in combination with a potentiostat (Solartron 1286), the frequency range and AC amplitude were 100 kHz-10 mHz and 5 mV_{rms}, respectively. Before recording the EIS measurements, the cells were charged at the desired SOC using the battery tester. The cells were tested inside a constant temperature chamber (ETAC, FL414P). The tests were carried out at 20, 30, 45 and 60 °C, so that the reaction kinetics could be evaluated accurately by using the proposed equivalent circuit. All measurements were carried out after the Li-ion cells were activated (aging by potential cycling).

3.3 Chronopotentiometric measurements, d*Q*/d*E* vs. *E* curves

To obtain the capacity of the lithium ion secondary cell incorporating the reference electrode, the cell was cycled using a battery tester (KIKUSUI, PFX2011). The cell was charged using a constant current step to 4.2 V at a rate of 4.2 mA followed by a constant voltage step of 1 hour 30 minutes. The cell was discharged using a constant current process at a rate of 4.2 mA until to 2.7 V.

After obtaining the value of the capacity C of the cell using the above method, a constant current charging and discharging test was carried out. The charging/discharging conditions were set at 0.2 C for the current and 2.7 V for the discharging voltage. dQ/dE vs. E curves were obtain by plotting the electrode potential (E) and the electrode capacity (Q).

dQ/dE vs. E curve represents the change of the crystal structure of the electrode active material. dQ/dE is equal to the current (I) divided by (dE/dt), as it is shown in the following equation:

$$\frac{\mathrm{d}Q}{\mathrm{d}E} = \frac{\mathrm{d}Q/\mathrm{d}t}{\mathrm{d}E/\mathrm{d}t} = \frac{\mathrm{d}(It)/\mathrm{d}t}{\mathrm{d}E/\mathrm{d}t} = \frac{I}{\mathrm{d}E/\mathrm{d}t}$$

Therefore, it is possible to obtain a pseudo-voltammogram. dQ/dE vs. E curves of cell before and after cycling degradation were obtained.

Fig. 3.2 shows the potential profile at a constant current versus time for the anode of the lithium ion secondary cell with a reference electrode that does not contain any deterioration. These data can be analyzed in detail by analyzing the change in the capacity (Q) vs. the potential dQ/dE, and by plotting these values versus the electric potential (E), then the curve of dQ/dE vs. E can be obtained. This plot is shown in Fig. 3.3.

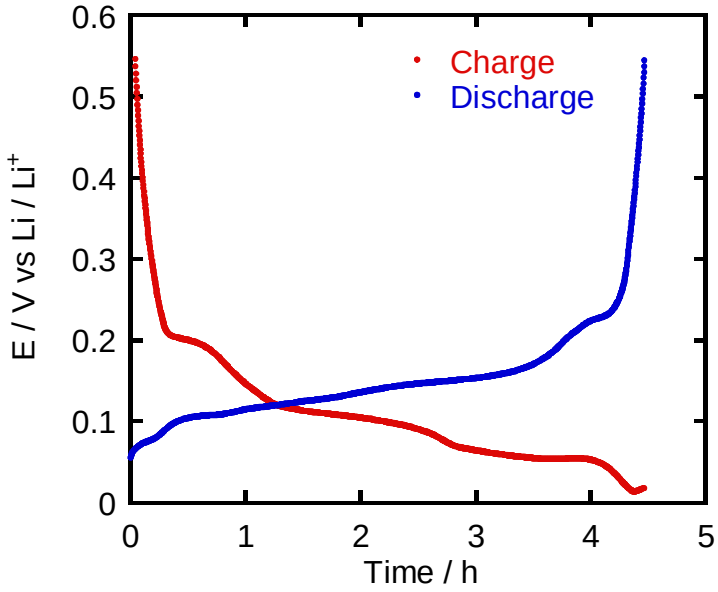

Fig. 3.2 Charging/discharging potential profile of the anode of a Li-ion secondary cell incorporating a reference electrode before cycling degradation

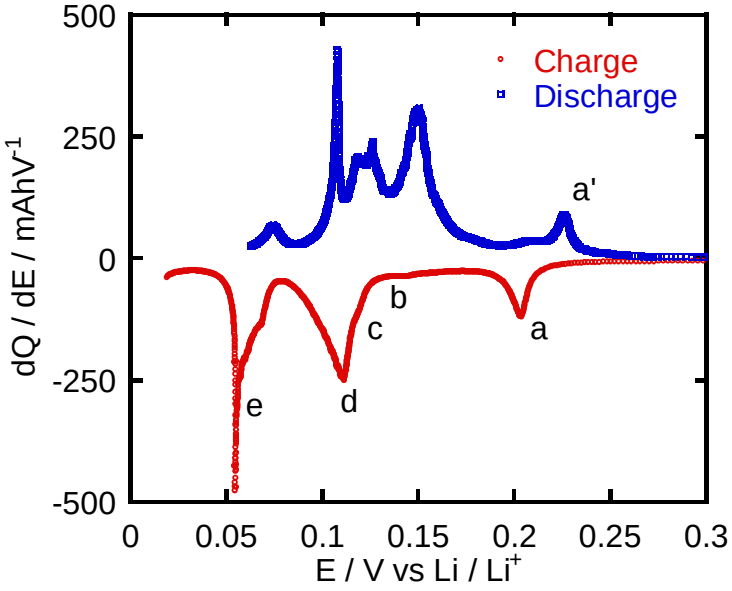

Fig. 3.3 dQ/dE vs. E curve of the anode of a Li-ion secondary cell incorporating a reference electrode before cycling degradation

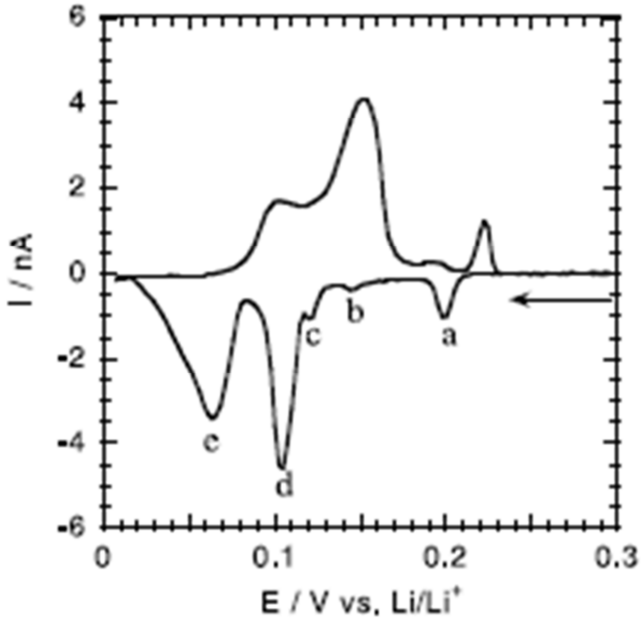

Fig. 3.4 Cyclic voltammogram of graphite single particle

Figure 3.3 shows the anode dQ/dE vs. E curve of the lithium ion secondary cell. The characteristic peaks a-e during the charging can be attributed to the structural changes in the graphite incorporated in the anode. Comparing the results with a reported ex-situ voltammogram, Fig. 3.4 [2, 7, 21], in the electrode potential range of 0.3~0.22 V vs. Li/Li^+, the Li ion density in graphite is very low, the Li ions are randomly inserted between all layers, and the graphite structure goes from the dilute stage-1 to stage-4 [2, 7, 21-25]. In the range of 0.18 ~ 0.22 V vs. Li/Li^+, a clear phase transition from stage-4 to stage-3 did not occur at peaks b and c. The phase transition from stage-3 to stage-2 occurs at peak d, and the phase transition from stage-2 to stage-1 occurs at peak e. By using a lithium ion secondary cell with a reference electrode, it is possible to obtain in-situ results that were similar to the half-cell ex-situ results [7].

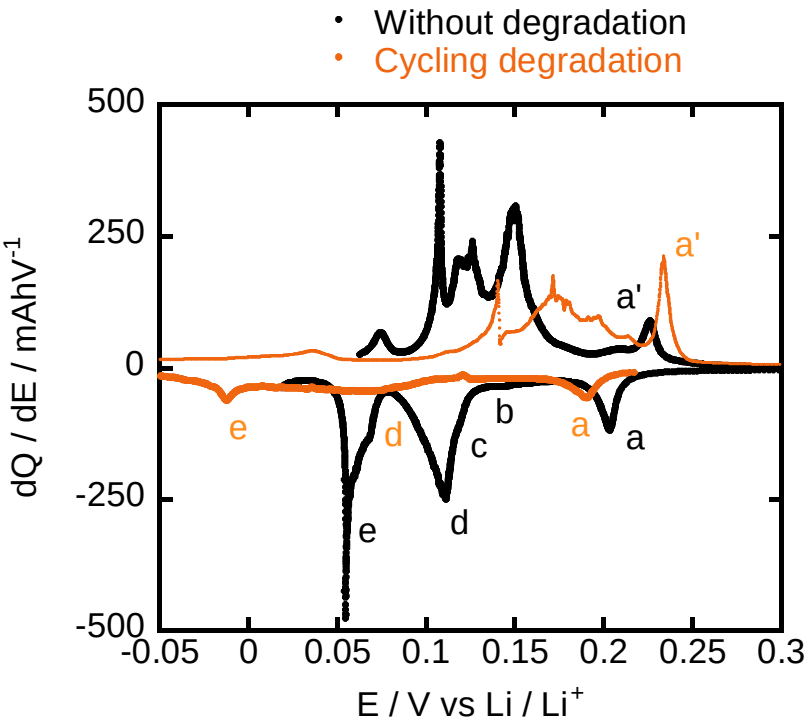

Fig. 3.5 d*Q*/d*E* vs. *E* curves of Li-ion secondary cells incorporating a reference electrode before (black) and after cycling degradation (orange)

Table 3.1 Comparison of d*Q*/d*E* vs. *E* curves of the cells before and after cycling degradation.

	△Ep (a - a') / V	*Qc'*/*Qc*	
		Peak a	Peaks b, c, d, e
Without degradation	0.018	---	---
Cycling degradation	0.042	0.700	0.568

Figure 3.5 shows the d*Q*/d*E* vs. *E* curves of Li-ion secondary cells incorporating a reference electrode before and after cycling degradation. In the case of the cell after cycling degradation, peaks b and c became too small and cannot be observed. Peaks a, b and e shifted to the negative potential side. Table 3.1 lists the difference in the oxidation and reduction peak potentials, △Ep (a - a'), and the charge coulomb ratio of the

degradation *Qc'*/*Qc*. *Qc*' expresses the quantity of coulombs for the reduction reaction peaks after degradation, and *Qc* expresses the ones before degradation. After cycling degradation △Ep (a - a') increased, indicating that the reversibility is reduced due to a possible damage in the crystal structure of the electroactive material. The reduction in the coulombic capacity of the charging peaks after cycling degradation is likely due to the decrease of Li-ion inventory contained in the electrolyte. During the cycling degradation test, the electrolyte reacts with the electroactive materials which generate the formation of a resistant film on the electroactive material causing a decrease of Li-ion inventory.

3.4 Electrochemical impedance spectroscopy measurements at different electro potentials and temperatures

EIS measurements at different temperatures and SOCs were carried out. Since a laminated Li-ion secondary cell incorporating a reference electrode was used, it is possible to obtain the impedance spectrum for the anode electroactive material vs. reference electrode and cathode electroactive material vs. reference electrode, shown in Fig. 3.6 (a). To confirm the effectiveness of these EIS measurements, the sum of anode vs. reference electrode and cathode vs. reference electrode impedance measurements with the full-cell impedance spectra (anode-cathode) were compared, shown in Fig. 3.6 (b). Less than 2% difference was found between the sums of electroactive materials vs. reference electrode impedance measurements and full-cell impedance measurements in the real part (Z') and less than 9% in the imaginary part (Z''). The difference found corroborates that the position of the reference electrode does not affect the performance of the cell, and it is possible to analyze the interphase between the electroactive materials and the electrolyte in a separate way.

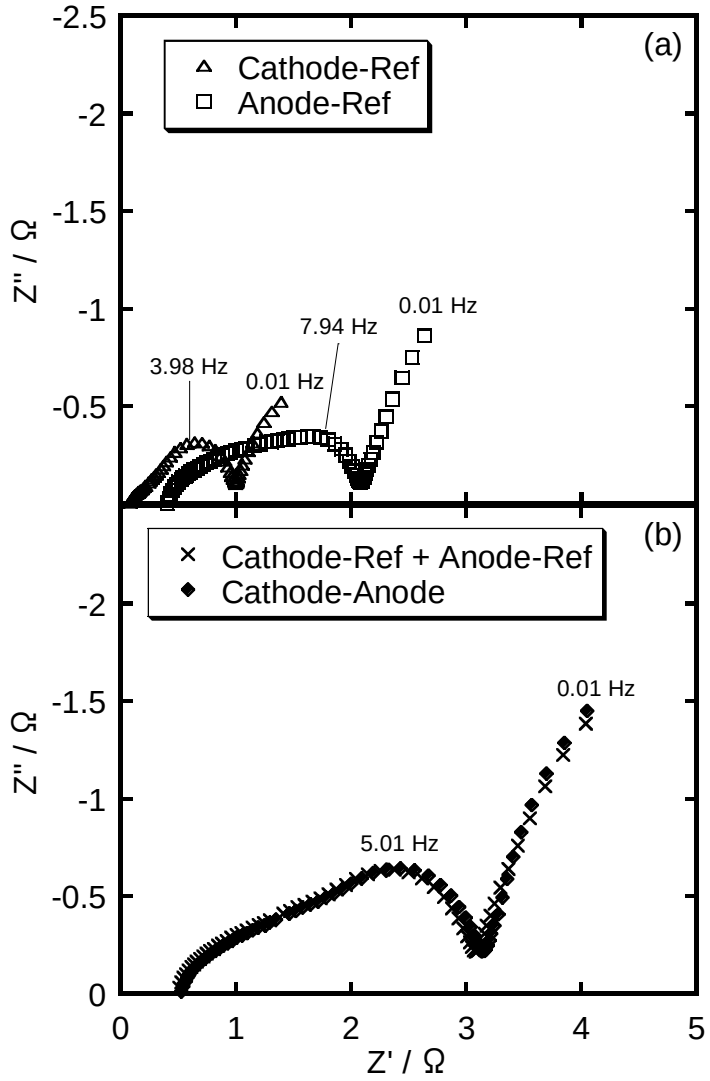

Fig. 3.6 (a) Impedance spectrum of the cathode-reference and anode-reference; (b) comparison between the anode-cathode spectra and the sum of cathode-reference and anode-reference impedance measurements of the $LiCoO_2$-Graphite Li-ion cell at 20℃ and at 50% SOC.

Figure 3.7 shows the impedance spectra for the anode of the lithium ion secondary cell before and after cycling degradation at 0, 25, 50, 75 and 100% SOC, and at 20, 30, 45 and 60 °C. The size of the semicircles tends to decrease with the temperature. The spectra exhibit three semicircles and a straight line having an angle of 45°, Fig. 3.8.

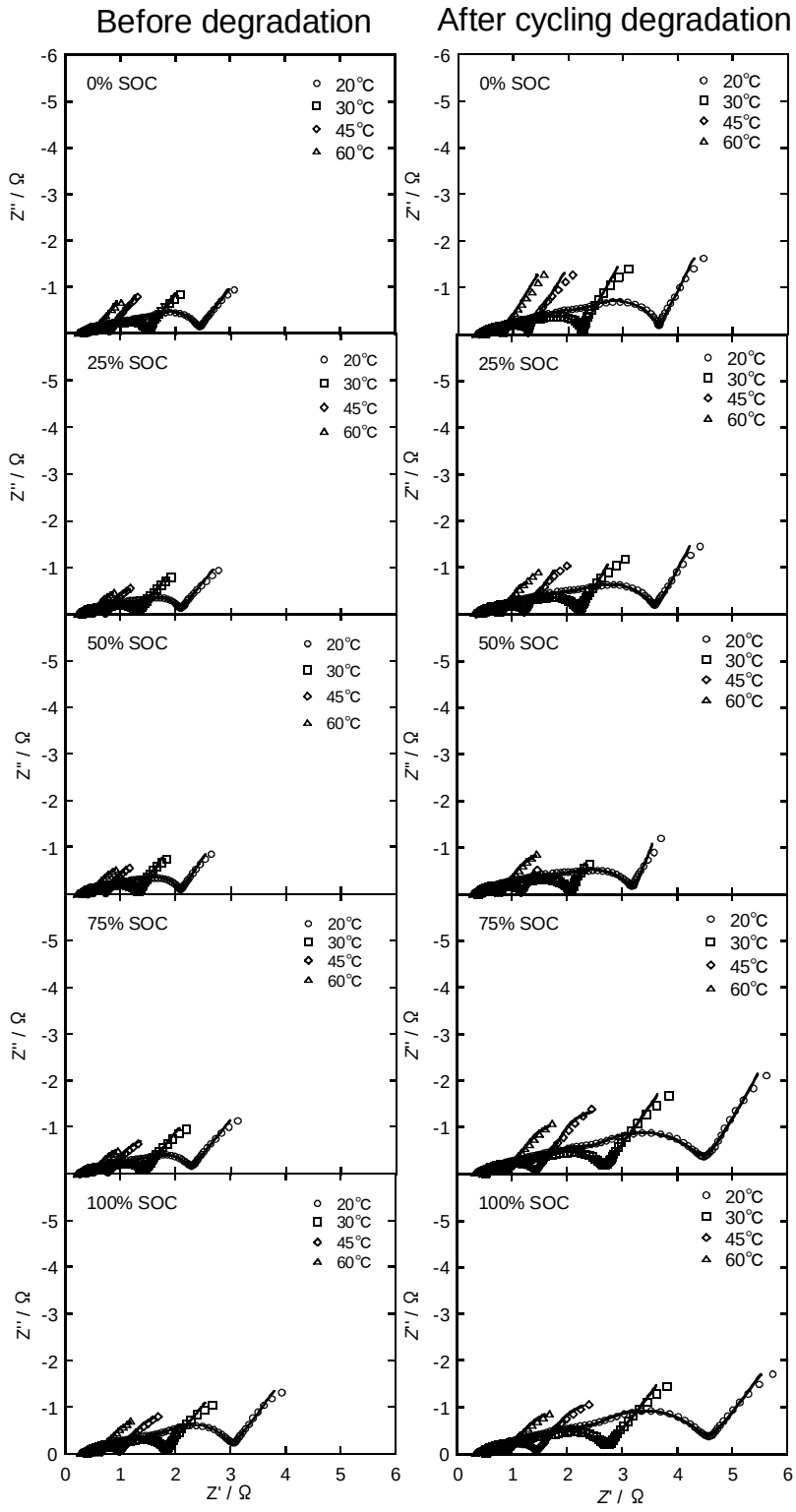

Fig. 3.7 Before and after cycling degradation impedance spectra for the anode electroactive material vs. reference electrode of the $LiCoO_2$-grahite Li-ion cell at 0, 25, 50, 75, 100% SOC and at 20, 30, 45 and 60 °C.

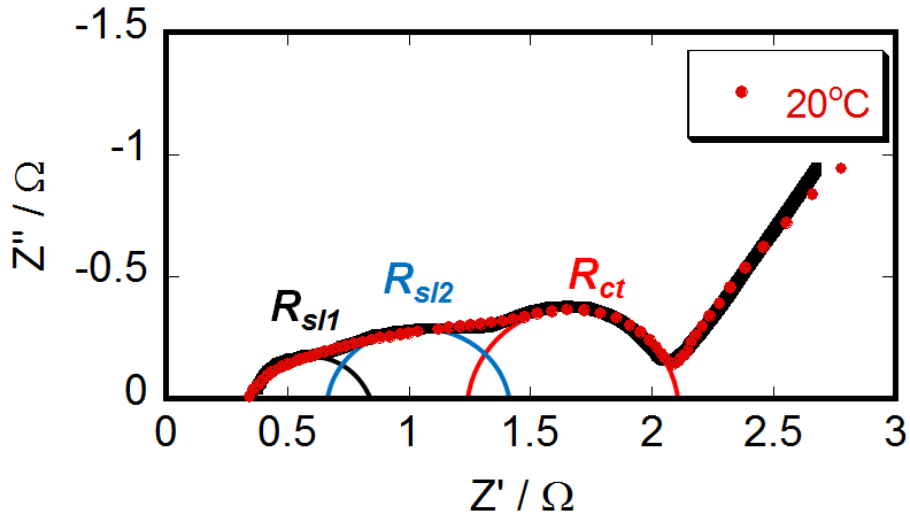

Fig. 3.8 Impedance spectra for the anode electroactive material vs. reference electrode of the $LiCoO_2$-grahite Li-ion cell at 50% SOC and 20 °C. R_{sl1}, R_{sl2} and R_{ct} correspond to lithium ion conduction, lithium ion desolvation and charge transfer resistances, respectively.

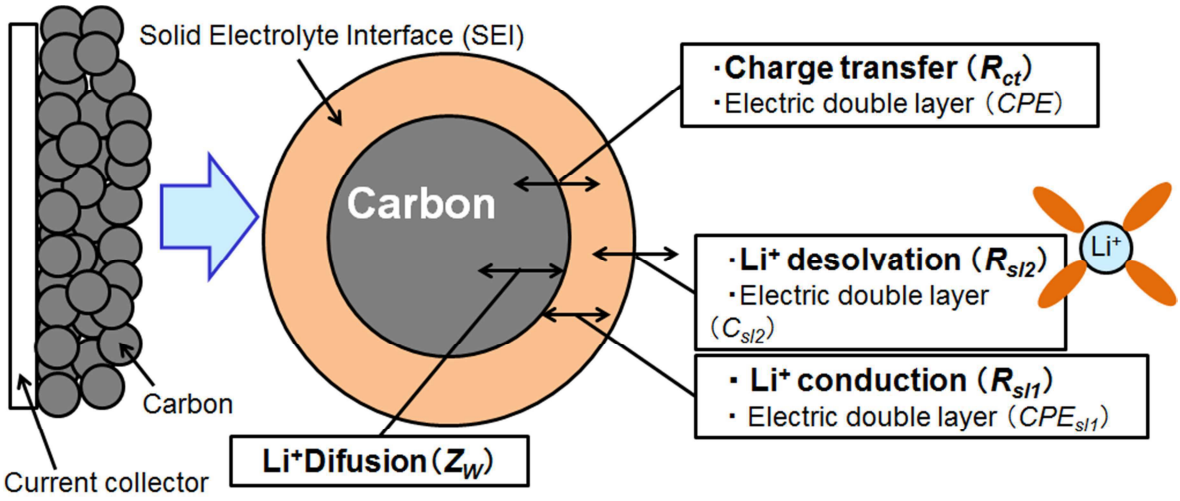

Fig. 3.9 Single particle model of the interphase reactions around solid electrolyte interphase.

Three main reactions take place on the solid electrolyte interphase (SEI) generated around the electroactive material, shown in Fig. 3.9. R_s corresponds to the resistance of the electrolyte. R_{sl1} is the resistance of Li-ion conduction in the SEI, and CPE_{sl1} represents the space charge capacitance of the SEI. R_{sl2} is the resistance of the Li-ion solvation/desolvation, and C_{sl2} corresponds to the solvation/desolvation capacitance. R_{ct} corresponds to the charge transfer resistance at the surface of the anode active material, and CPE is a constant phase element. The CPE was used to take into account the roughness of the anode material surface. Z_w represents the Warburg resistance due to the Li-ion diffusion in the anode particle. Electrochemical impedance spectra fittings were carried out using the equivalent circuit shown in Fig. 3.10. During the impedance spectra fitting, we followed a rigorous method to obtain the best possible fit from the experimental data. Zview 2 software (Scribner Associates Inc.) was used to carry out the impedance spectra fittings. The chi-squared function (χ^2) delivers a good indication of the quality of the fitting [26]. The χ^2 values of 10^{-5} – 10^{-4} show a reasonably good fit. The values of χ^2 in this study were in the range of 10^{-4}.

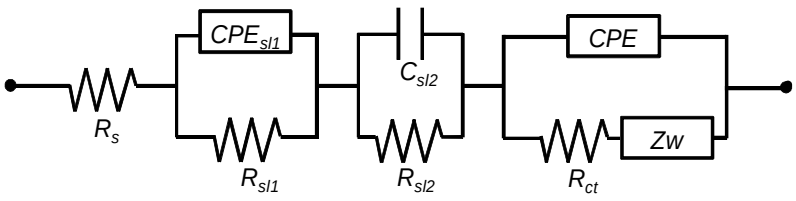

Fig. 3.10 Equivalent circuit used for the anode impedance spectra fittings. R_s, R_{sl1}, R_{sl2} and R_{ct} correspond to electrolyte, lithium ion conduction, lithium ion desolvation and charge transfer resistances, respectively.

3.5 Kinetic analysis of the anode reactions before and after degradation

Based on the proposed equivalent circuit, the activation energy and pre-exponential factor of the anode reactions were obtained by using the expression (1) [9],

$$\frac{RT}{nFR_{rct}} = k_0' exp\left(\frac{-E_a}{RT}\right) \qquad (1)$$

where E_a is the activation energy, k'_0 is the pre-exponential factor, R_{rct} is the reaction resistance, n is the reaction electrode, F is the Faraday constant, T is the absolute temperature and R is the gas constant. Arrhenius plots are made by plotting the resistance values obtained from the experimentally fitted data at different temperatures, and then the activation energy of each resistance is obtained from the Arrhenius plots. Figure 3.11 shows Arrhenius plots for Li-ion conduction, Li-ion solvation/desolvation and charge transfer resistances of the anode active material before and after cycling degradation at 50% SOC. The slope of the lines corresponds to the activation energy, defined by Eq. (1). The activation energy and pre-exponential factor of the reactions were obtained at 0%, 12%, 25%, 33%, 42%, 50%, 62%, 75%, 85% and 100% SOCs for the cell before degradation. For the cell after degradation the kinetic parameters were obtained at 0%, 25%, 50%, 75% and 100%. Anode potential of the Li-ion cell versus the reference electrode was measured at each SOC.

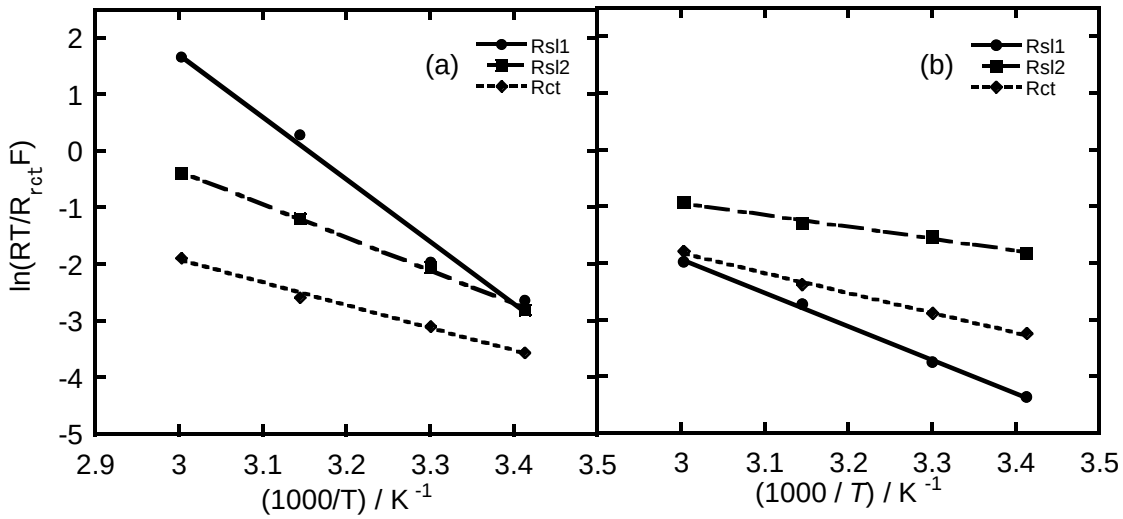

Fig. 3.11 Arrhenius plots of Li^+ conduction (R_{sl1}), Li^+ solvation/desolvation (R_{sl2}) and charge transfer (R_{ct}) before (a) and after (b) cycling degradation at 50% state of charge.

Figure 3.12 shows the activation energy of and pre-exponential factor of charge transfer (R_{ct}) before and after cycling degradation as a function of anode potential. The change of the activation energy and pre-exponential factor can be analyzed in detail by considering the changes in the graphite structure. To analyze the change of the activation energy based on the Li-ion insertion/deinsertion mechanism into graphite, the graphite staging process is highlighted by vertical lines in Fig.3.12. The activation energy and pre-exponential factor of R_{ct} tend to decrease with the potential, indicating that the staging phenomenon of graphite affects the charge transfer process. In the case where the Li-ions can be inserted anywhere in the graphitized carbon, the magnitude of the activation energy is relatively low. However, in stage-1, the Li-ion insertion/deinsertion accompanies a large structural change, where the activation energy is comparatively high. The behavior of activation energy and pre-exponential factor after degradation tend to decrease and increase without following any clear tendency, and this is likely due to a possible damage of the graphite crystal structure caused by cycling degradation, which may affect the Li-ion insertion/deinsertion reactions.

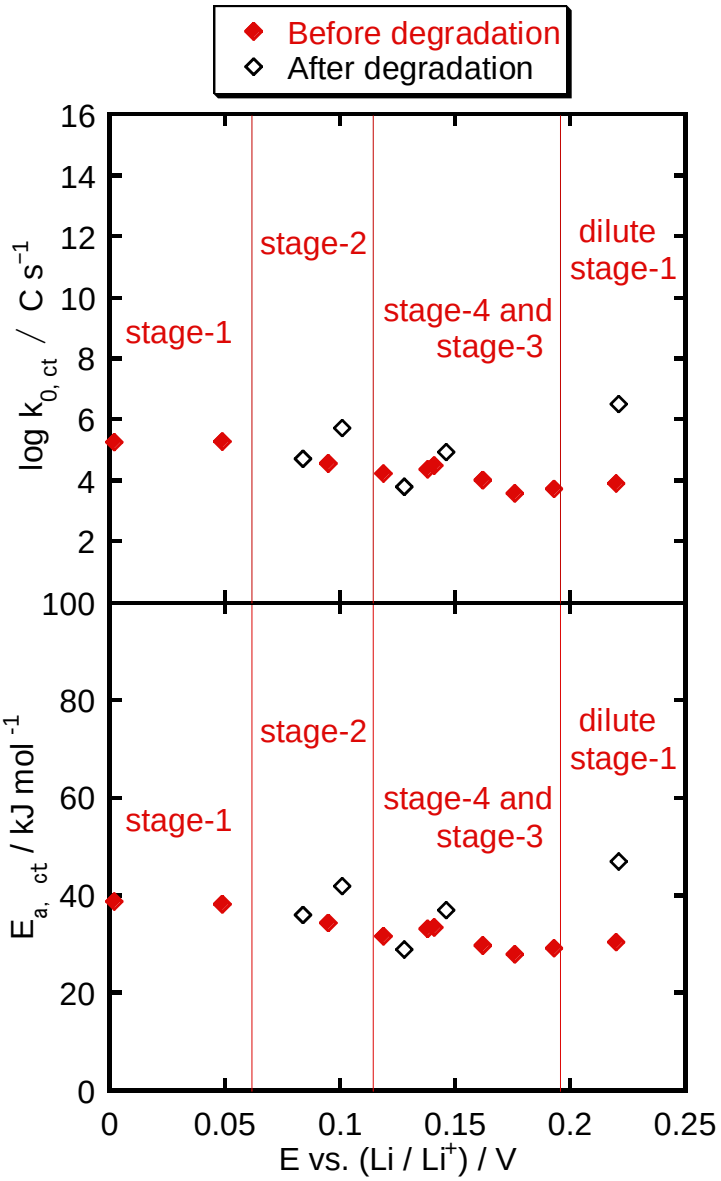

Fig. 3.12 Pre-exponential factor ($k_{0,\ ct}$) and activation energy ($E_{a,\ ct}$) of charge transfer reactions before and after degradation as a function of anode potential.

Figure 3.13 shows the change in the activation energy and pre-exponential factor of the Li-ion conduction reactions (R_{sl1}) before and after cycling degradation as a function of anode potential. Before degradation, the activation energy and pre-exponential factor of R_{sl1} shows a nearly constant behavior, some slightly changes are observed. This suggests that the solid electrolyte interphase (SEI), generated around the anode active

material, remains almost constant and does not change with the state of charge. After degradation, the behavior of activation energy and pre-exponential do not follow a clear tendency. This irregular behavior suggests that the SEI generated around graphite after cycling degradation tends to grow irregularly, affecting the Li-ion conduction reactions, where a partially solvated Li-ion moves through the SEI, shown in Fig. 3.14.

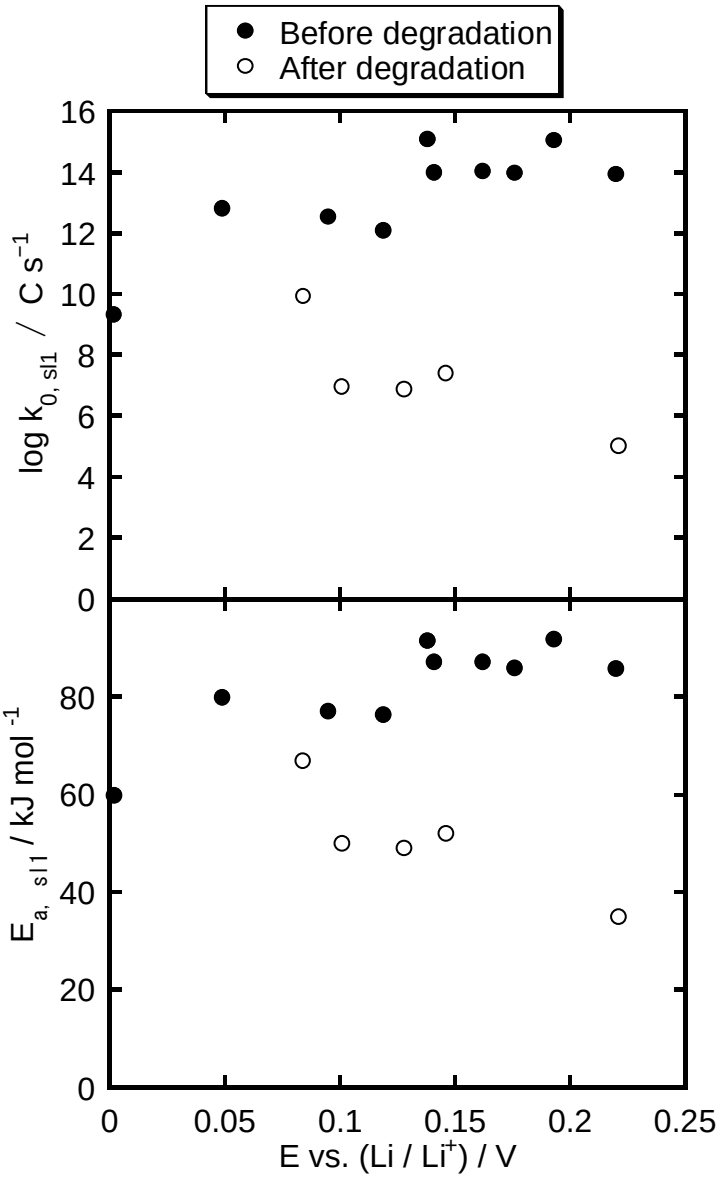

Fig. 3.13 Pre-exponential factor ($k_{0,\ sl1}$) and activation energy ($E_{a,\ sl1}$) of Li-ion conduction reactions before and after degradation as a function of anode potential.

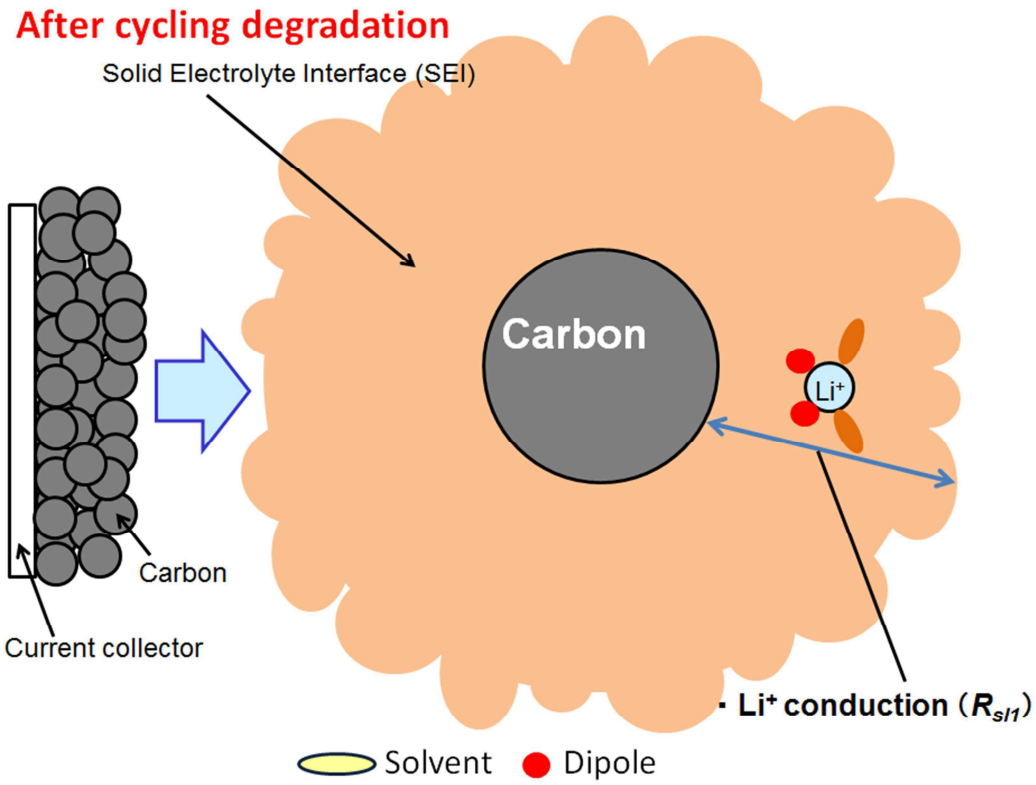

Fig. 3.14 Single particle model of Li-ion conduction reaction after cycling degradation.

R_{sl1} and R_{ct} describe the resistance of Li-ion conduction in the SEI and the charge transfer resistance at the surface of the anode active material, respectively. These reactions occur in the interface between the SEI and electroactive material. Meyers et al., developed a mathematical model to describe the impedance response of a single intercalation particle surrounded by a resistance film [27], they established that charge transfer and double layer charging across each interface (particle/film and film/solution) must be considered. Since R_{ct} corresponds to the charge transfer resistance between graphitized carbon and SEI, consequently, R_{sl2} corresponds to the resistance of Li-ion solvation/desolvation between the SEI and electrolyte.

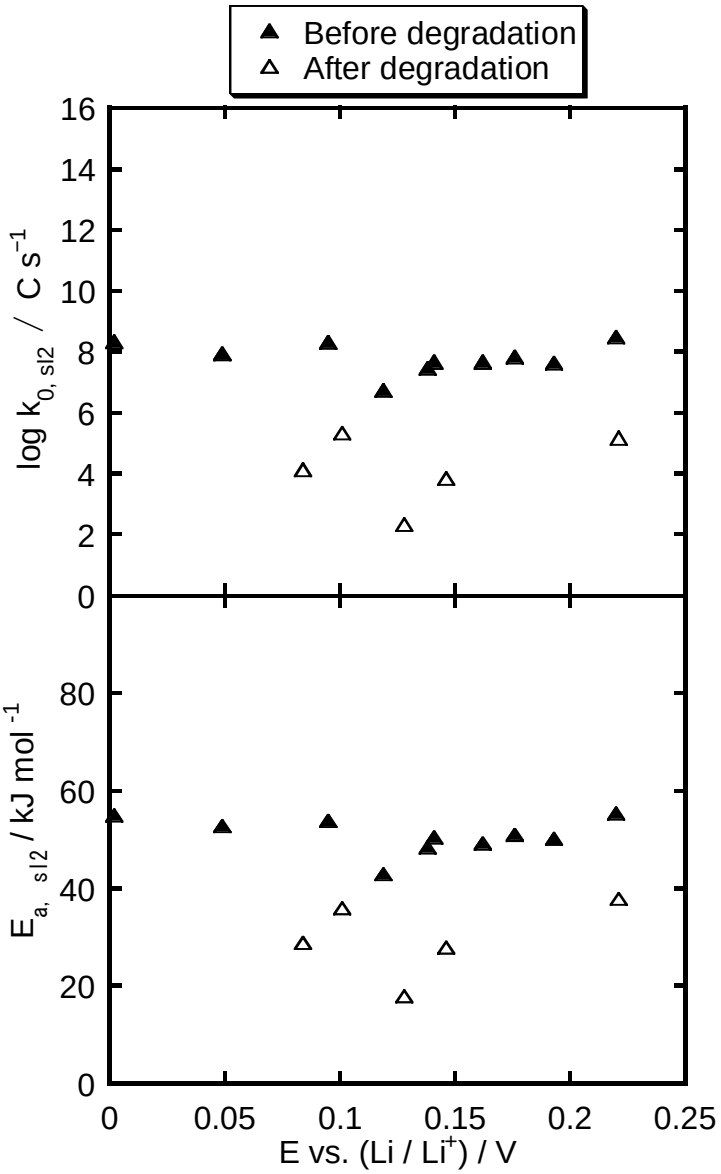

Fig. 3.15 Pre-exponential factor ($k_{0,\ sl2}$) and activation energy ($E_{a,\ sl2}$) of Li-ion solvation/desolvation reactions before and after degradation as a function of anode potential.

Figure 3.15 shows the activation energy and pre-exponential factor of Li-ion solvation/desolvation (R_{sl2}) before and after cycling degradation as a function of anode potential. The activation energy and pre-exponential factor of R_{sl2} before degradation shows a practically constant behavior before degradation, this kind of behavior is expected since the Li-ion solvation/desolvation should not change with the potential.

However, the behavior of activation energy and pre-exponential after degradation does not follow a constant tendency, this suggests that Li-ion solvation/desolvation reactions occurring at the interphase of electrolyte and SEI are affected by cycling degradation, where Li–ions are partially solvated/desolvated, shown in Fig. 3.16.

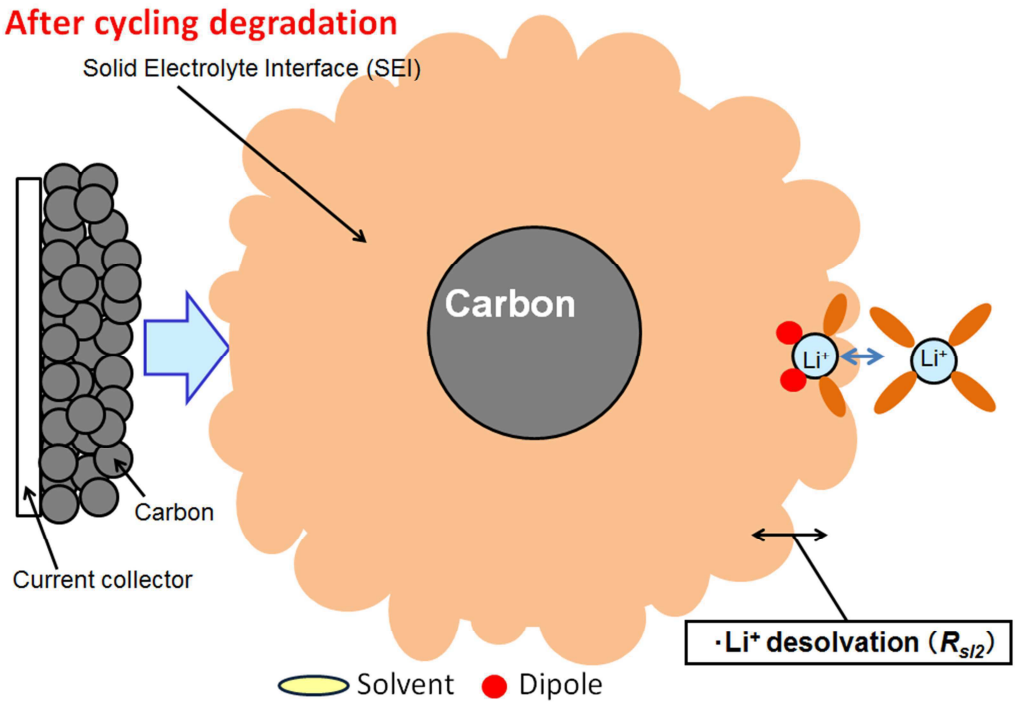

Fig. 3.16 Single particle model of Li-ion solvation/desolvation reactions after cycling degradation.

3.6. Comparison of the activation energy

To compare the activation energy with those previously reported, the overall activation energy of the anode reactions has to be obtained. By adding the resistance values of the charge transfer, Li-ion conduction and Li-ion solvation/desolvation reactions, a total resistance value is obtained (R_{total}). The overall activation energy of the anode reactions is obtained by making Arrhenius plots using the R_{total} values. Figure 3.17 shows the activation energy of R_{total} before and after cycling degradation as a

function of anode potential. The activation energy of R_{total} exhibits a constant behavior and does not change with anode potential. The activation energy of R_{total} is consistent according to the data that has been previously reported for graphitized carbons [9, 28].

Consequently, by recording EIS measurements, it is possible to independently analyze Li-ion solvation/desolvation, Li-ion conduction and charge transfer reactions from the anode of a Li-ion secondary cell incorporating a reference electrode.

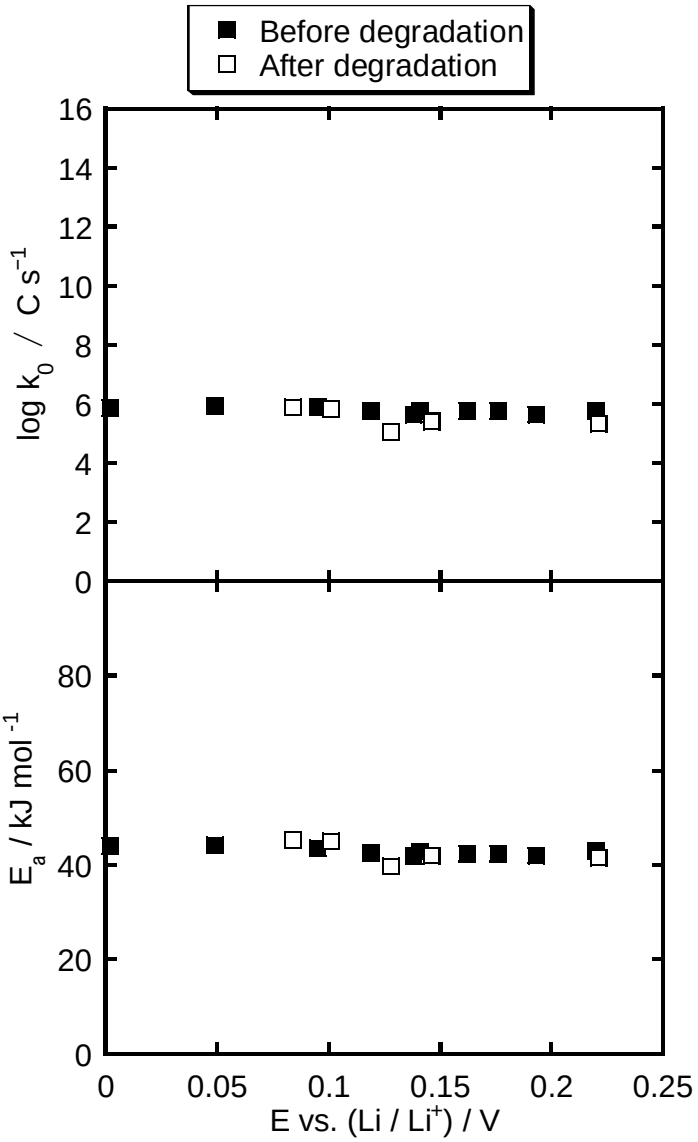

Fig. 3.17 Pre-exponential factor (k_0) and activation energy (E_a) of the overall anode reactions before and after degradation as a function of anode potential.

3.7 Conclusions

The process of lithium-ion insertion/deinsertion into graphitized carbon was analyzed at different temperatures and state of charge by carrying out EIS measurements using a Li-ion secondary cell incorporating a reference electrode. The activation energy of Li-ion conduction, Li-ion desolvation and charge transfer reactions were analyzed before and after cycling degradation as a function of SOC and anode potential. The results were evaluated using the staging process of graphite.

Charge transfer, Li-ion conduction and Li-ion desolvation/solvation reactions originating from SEI were analyzed as a function of SOC and anode electrode potential. The activation energy of charge transfer depends on SOC and anode potential, indicating that the staging process of graphite is affecting the charge transfer reaction. On the other hand, the activation energies of Li-ion conduction and Li-ion solvation/desolvation are independent on SOC and anode potential, showing that the staging process of graphite does not affect the Li-ion conduction and Li-ion solvation/desolvation reactions.

References

[1] M. S. Dresselhaus, G. Dresselhaus, Intercalation compounds of graphite, Adv. in Phys. 51 (1) (2002) 1.

[2] T. Ohzuku, Y. Iwakoshi, K. Sawai, Formation of lithium-graphite intercalation compounds in nonaqueous electrolytes and their application as a negative electrode for a lithium ion (shuttlecock) cell, J. Electrochem. Soc. 140 (1993) 2490.

[3] J. N. Reimers, J. R. Dahn, Electrochemical and in situ X-ray diffraction studies of lithium intercalation in Li_xCoO_2, J. Electrochem. Soc. 139 (1992) 2091.

[4] J. Choi, A. Manthiram, Structural and electrochemical characterization of the layered $LiNi_{0.5-y}Mn_{0.5-y}Co_{2y}O_2$ ($0 \leq 2y \leq 1$) cathodes, Solid State Ionics 176 (2005) 2251.

[5] G. Li, Z. Lu, B. Huang, H. Huang, R. Xue, L. Chen, An evaluation of lithium intercalation capacity into carbon by XRD parameters, Solid State Ionics 81 (1995) 15.

[6] K. Dokko, M. Mohamedi, Y. Fujita, T. Itoh, M. Nishikawa, M. Umeda, I. Uchida, Kinetic characterization of single particles of $LiCoO_2$ by AC impedance potential step methods, J. Electrochem. Soc. 148 (2001) A422.

[7] M. Umeda, K. Dokko, Y. Fujita, M. Mohamedi, I. Uchida, J. R. Selman, Electrochemical impedance study of Li-ion insertion into mesocarbon mircrobead single particle electrode Part. I. Graphitized carbon, Electrochim. Acta. 47 (2001) 885.

[8] K. Dokko, Y. Fujita, M. Mohamedi, M. Umeda, I. Uchida, J. R. Selman, Electrochemical impedance study of Li-ion insertion into mesocarbon mircrobead single particle electrode Part. II. Disordered carbon, Electrochim. Acta. 47 (2001) 933.

[9] P. Suresh, A. K. Shukla, N. Munichandraiah, Temperature dependence studies of ac impedance of lithium-ion cells, J. Appl. Electrochem. 32 (2002) 267.

[10] T. Hang, D. Mukoyama, H. Nara, N. Takami, T. Momma, T. Osaka, Electrochemical impedance spectroscopy analysis for lithium-ion battery using $Li_4Ti_5O_{12}$ anode, J. Power Sources. 222 (2013) 442.

[11] N. Schweikert, R. Heinzmann, A. Eichhöfer, H. Hahn, S. Indris, Electrochemical impedance spectroscopy of $Li_4Ti_5O_{12}$ and $LiCoO_2$ based half-cells and $Li_4Ti_5O_{12}/LiCoO_2$ cells: internal interfaces and influence of state of charge and cycle number, Solid State Ionics, 226 (2012) 15.

[12] D. Andre, M. Meiler, K. Steiner, Ch. Wimmer, T. Soczka-Guth, D. U. Sauer, Characterization of high-power lithium-ion batteries by electrochemical impedance spectroscopy. I. Experimental investigation, J. Power Sources. 196 (2011) 5334.

[13] J. Gomez, R. Nelson, E. E. Kalu, M. H. Weatherspoon, J. P. Zheng, Equivalent circuit model parameters of a high-power Li-ion battery: thermal and state of charge effects, J. Power Sources. 196 (2011) 4826.

[14] S. Zhang, M. S. Ding, K. Xu, J. Allen, Understanding Solid Electrolyte Interface Film Formation on Graphite Electrodes, Electrochem. Solid-State Lett. 4 (2001) A206.

[15] M. Itakagi, N. Kobari, S. Yotsuda, K. Watanabe, S. Kinoshita, M. Ue, In situ electrochemical impedance spectroscopy to investigate negative electrode of lithium-ion rechargeable batteries, J. Power Sources. 135 (2004) 255.

[16] C. Wang. A. J. Appley, F. E. Little, Criteria for Reliable Electrochemical Impedance Measurements on Li-ion Battery Anodes, J. Electrochem. Soc. 150 (2003) A143.

[17] Z. Ogumi, Interfacial Reactions of Lithium-ion Batteries, Electrochemistry, 78 (2010) 319.

[18] H. Manjunatha, K. C. Mahesh, G. S. Suresh, T. V. Venkatesha, The study of Lithium ion de-insertion/insertion in $LiMn_2O_4$ and determination of kinetic parameters in aqueous Li_2SO_4 solution using electrochemical impedance spectroscopy, Electrochim. Acta. 56 (2011) 1439.

[19] M. Dolle, F. Orsini, A. S. Gozdz, J. M. Tarascon, Development of Reliable Three-Electrode Impedance Measurements in Plastic Li-ion Batteries, J. Electrochem. Soc. 148 (2001) A851.

[20] J. Y. Song, H. H. Lee, Y. Y. Wang, C. C. Wan, Two and three-electrode impedance spectroscopy of lithium-ion batteries, J. Power Sources. 111 (2002) 255.

[21] J. R. Dahn, Phase diagram of Li_xC_6, Phys. Rev. B. 44 (1991) 9170.

[22] T. Abe, Y. Mizutani, M. Asano, In situ raman study on electrochemical Li intercalation into graphite, J. Electrochem. Soc. 142 (1995) 20.

[23] D. A. Totir, D. A. Scherson, Electrochemical and in situ raman studies of embedded carbon particle electrodes in nonaqueous liquid electrolytes, Electrochem. Solid-Sate Lett. 3 (2000) 263.

[24] R. Kanno, Y. Kawamoto, Y. Takeda, S. Ohashi, N. Imanishi, O. Yamamoto, Carbon fiber as a negative electrode in lithium secondary cells, J. Electrochem. Soc. 139 (1992) 3397.

[25] K. Zaghib, K. Tatsumi, Y. Sawada, S. Higuchi, H. Abe, T. Ohsaki, Li-NMR of well-graphitized vapor grown carbon fibers and natural graphite negative electrodes of rechargeable lithium-ion batteries, J. Electrochem. Soc. 146 (1999) 2784.

[26] B. A. Boukamp, A nonlinear least squares fit procedure for analysis of immittance data of electrochemical systems, Solid State Ionics. 20 (1986) 31.

[27] J. P. Meyers, M. Doyle, R. M. Darling, J. Newman, The Impedance Response of a Porous Electrode Composed of Intercalation Particles, J. Electrochem. Soc. 147 (2000) 2930.

[28] H. Ishikawa, O. Mendoza, Y. Sone, M. Umeda, Study of thermal deterioration of lithium-ion secondary cells using an accelerated rate calorimeter (ARC) and ac impedance method, J. Power Sources 198 (2012) 236.

Chapter 4 "Kinetic Comparison of $LiCoO_2$ and $LiMn2O_4$ Cathode Material Reactions in Li-ion Secondary Cells Incorporating a Reference Electrode"

4.1 Introduction

Electroactive materials are a critical part of Li-ion secondary cells and these play an important role in cell performance [1]. Exchange of Li-ions between the electroactive materials occurs at the electrode-electrolyte interface, so the performance of Li-ion secondary cells strongly depends on the electrochemical properties, morphology and microstructure of electroactive materials [2-4]. The kinetic analysis of the Li-ion insertion/deinsertion reactions, and its dependency on electroactive material structural changes, is very important to design cells with a high performance. Many efforts have been made to analyze the Li-ion insertion/deinsertion reactions in electroactive materials using many techniques such as XRD and cyclic voltammetry [5-8]. But these studies were carried out using half-cells or single particle electrodes, and did not measure the reactions that are occurring in situ.

The reactions of two different cathode materials using sealed Li-ion secondary cells incorporating a reference electrode are analyzed. $LiCoO_2$ and $LiMn_2O_4$ are widely used in commercial Li-ion cells, the lattice of these materials experience significant volume changes and phase transformation during the Li-ion insertion/deinsertion process, which could induce stress resulting in fracture inside the electroactive material, and it is known that a mechanical damage of electroactive materials leads to the degradation of cell performance and life [9]. A comparison of the kinetic characteristics of electroactive materials and is important for selecting an electroactive material for specific uses. Electrochemical impedance spectroscopy (EIS) is a non-destructive method that allows the in situ analysis of electroactive materials [10, 11]. By obtaining

dQ/dE vs. E curves, the structural changes of electroactive materials can be analyzed [12]. In this work, the activation energy, frequency factor and reaction rate constant dependency of the Li-ion insertion/deinsertion reactions on the structural changes of $LiCoO_2$ and $LiMn_2O_4$ are analyzed by carrying out EIS measurements at different state of charge and temperatures.

4.2 Experimental methodology

4.2.1 Cell specifications

Two laminated lithium ion secondary cells containing a reference electrode with different cathode electroactive materials were tested. One cell used $LiCoO_2$ as cathode material, and the other one $LiMn_2O_4$. Both cells used graphitized carbon as anode material. The cells consist of a negative electrode, separator, reference electrode and positive electrode. A schematic diagram of the cells is shown in Fig. 4.1. The size and position of the reference electrode were optimized so that it does not affect the charge and discharge performance of the cell. Lithium foil was used as the reference electrode, which was inserted between the positive and negative electrodes. The electrolyte contained 1 mol dm^{-3} $LiPF_6$, the solvent was ethylene carbonate: diethyl carbonate = 7:3 (volume), and the size of the cell electrodes was 46 mm × 46 mm (including the laminate package). The capacity of these lithium ion secondary cells with the reference electrode was 20 mAh.

4.2.2 Chronopotentiometric measurements (d*Q*/d*E* vs. *E* curves)

To obtain the capacity of the lithium ion secondary cell incorporating the reference electrode, the cell was cycled using a battery tester (KIKUSUI, PFX2011). The cell was charged using a constant current step to 4.2 V at a rate of 4.2 mA followed

by a constant voltage step of 1 hour 30 minutes. The cell was discharged using a constant current process at a rate of 4.2 mA until to 2.7 V.

After obtaining the value of the capacity C of the cell using the above method, a constant current charging and discharging test was carried out. The charging/discharging conditions were set at 0.2 C for the current and 2.7 V for the discharging voltage. d*Q*/d*E* vs. *E* curves were obtain by plotting the electrode potential (*E*) and the electrode capacity (*Q*).

d*Q*/d*E* vs. *E* curve represents the change of the crystal structure of the electrode active material. d*Q*/d*E* is equal to the current (*I*) divided by (d*E*/d*t*), as it is shown in the following equation:

$$\frac{\mathrm{d}Q}{\mathrm{d}E} = \frac{\mathrm{d}Q/\mathrm{d}t}{\mathrm{d}E/\mathrm{d}t} = \frac{\mathrm{d}(It)/\mathrm{d}t}{\mathrm{d}E/\mathrm{d}t} = \frac{I}{\mathrm{d}E/\mathrm{d}t}$$

Therefore, it is possible to obtain a pseudo-voltammogram. d*Q*/d*E* vs. *E* curves of cell before and after cycling degradation were obtained.

4.2.3 Electrochemical Impedance Spectroscopy measurements

Electrochemical impedance spectroscopy (EIS) measurements were carried out using a frequency response analyzer (Solartron 1260) in combination with a potentiostat (Solartron 1286), the frequency range and AC amplitude were 100 kHz-10 mHz and 5 mV_{rms}, respectively. Before recording the EIS measurements, the cells were charged at the desired SOC using the battery tester. The cells were tested inside a constant temperature chamber (ETAC, FL414P). The tests were carried out at 20, 30, 45 and 60℃, so that the reaction kinetics could be evaluated accurately by using the proposed equivalent circuit. All measurements were carried out after the Li-ion cells were activated (aging by potential cycling).

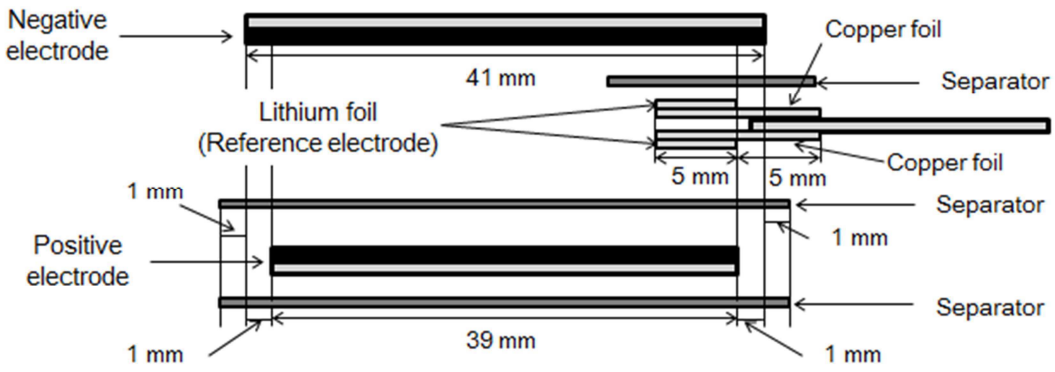

Fig. 4.1 Schematic illustration of the Li-ion secondary cell incoporating a reference electrode.

4.3 Results and discussion

4.3.1 dQ/dE vs. E curves

Fig. 4.2 shows the cathode dQ/dE vs. E curve of the $LiCoO_2$-graphite cell incorporating a reference electrode. The characteristic peaks are attributed to the crystal structural changes of $LiCoO_2$ during lithium ion intercalation/deintercalation. The obtained cathode dQ/dE vs. E curve is comparable with a reported $LiCoO_2$ half-cell ex-situ voltammogram [6]. By analyzing the characteristic peaks of the cathode dQ/dE vs. E curve with reported X-ray diffraction studies of lithium intercalation in $LiCoO_2$ [3, 13], four different structural regions are observed. In the first region, 3.8-3.91 V vs. Li/Li^+, a Hexagonal-I structure predominates. In the second region, 3.91-3.96 V vs. Li/Li^+, a structural transition phase between Hexagonal-I to Hexagonal-II is observed. In the third region, 3.96-4.1 V vs. Li/Li^+, a Hexagonal-II structure predominates. In the fourth region, 4.1-4.18 V vs. Li/Li^+, the crystal structure goes from Hexagonal-II to Monoclinic.

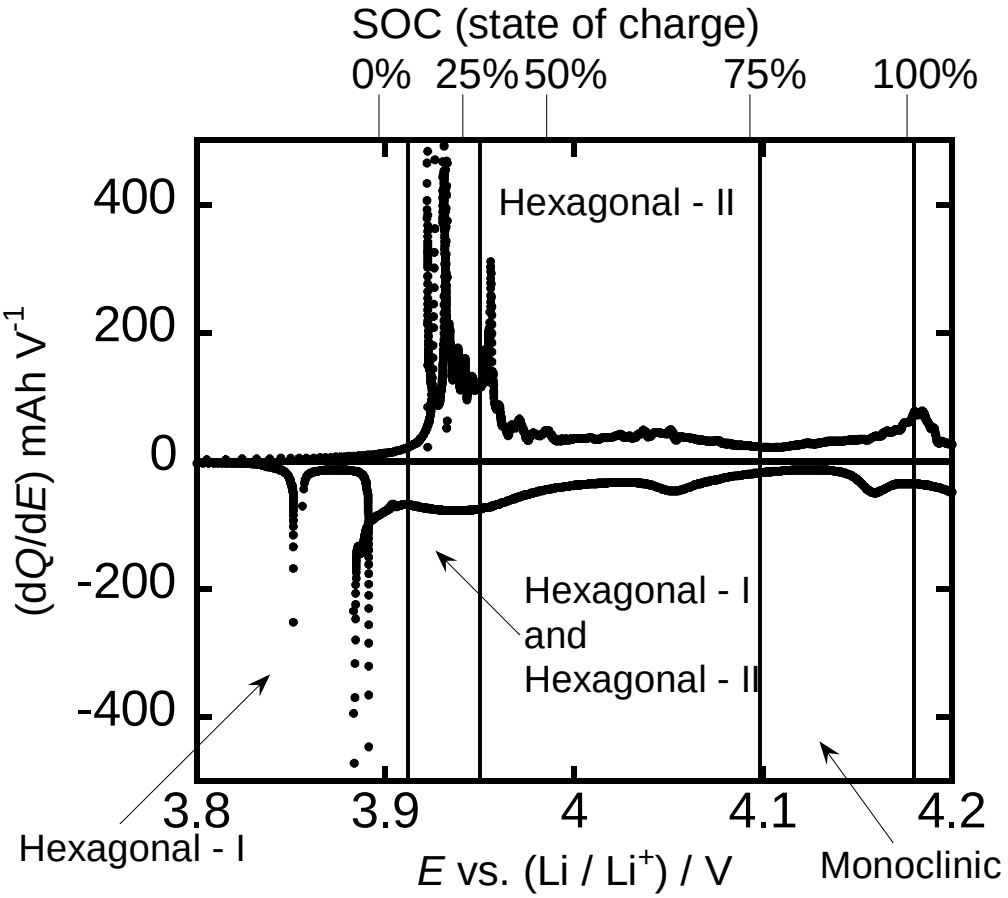

Fig. 4.2 Cathode d*Q*/d*E* vs. *E* curve of $LiCoO_2$-grahite Li-ion secondary cell.

Fig. 4.3 shows the cathode dQ/dE vs. E curve of the $LiMn_2O_4$-graphite cell incorporating a reference electrode. $LiMn_2O_4$ has a cubic spinel structure. The characteristic peaks are attributed to the lithium ion intercalation/deintercalation due to the redox of $Mn^{3+/4+}$ in the spinel structure [14]. The obtained dQ/dE vs. E curve is comparable with a reported a reported $LiMn_2O_4$ half-cell ex-situ voltammogram [14]. According to X-ray diffraction studies, lithium ion insertion and extraction in $LiMn_2O_4$ occur in two phases, both phases having the same structure with different lattice parameters, which produce dQ/dE vs. E curves with two peaks [15].

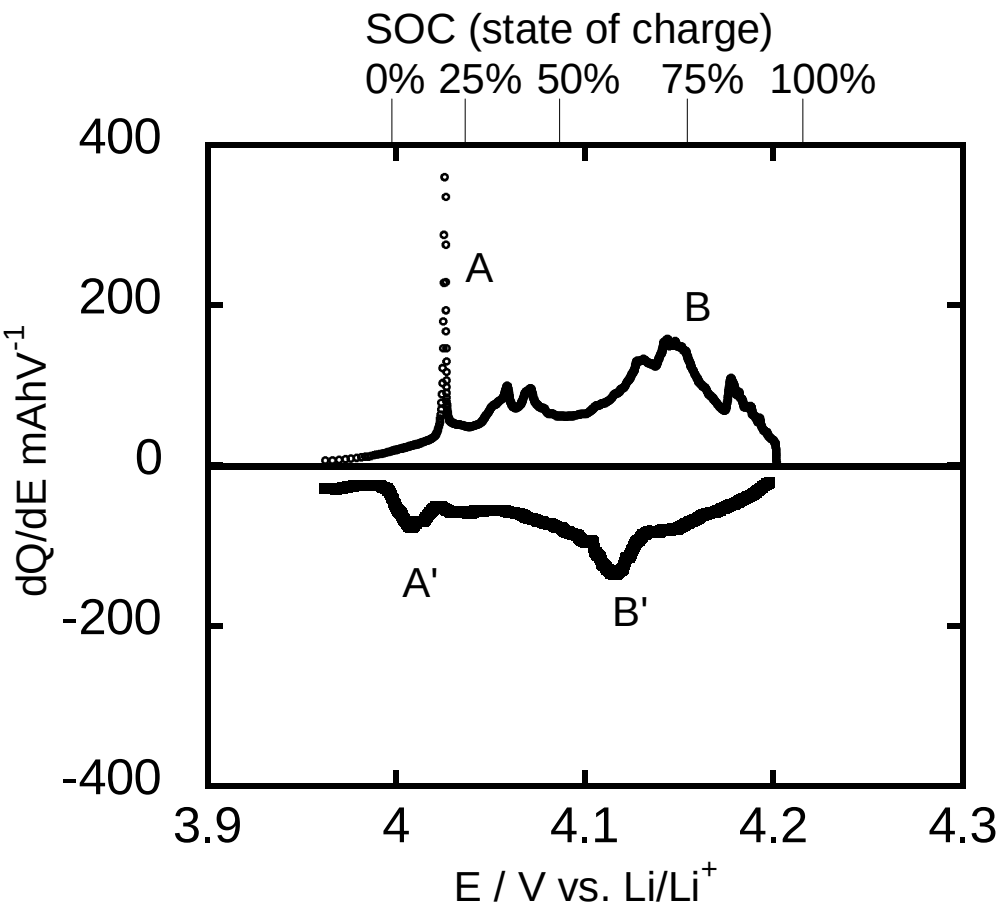

Fig. 4.3 Cathode dQ/dE vs. E curve of $LiMn_2O_4$-grahite Li-ion secondary cell.

4.3.2 Electrochemical Impedance Spectroscopy measurements

Fig. 4.4 (a) shows impedance spectra of the $LiCoO_2$ and $LiMn_2O_4$ cathode materials vs. reference and anode vs. reference electrode at 20℃ and 50% SOC. Since we used Li-ion secondary cells incorporating a reference electrode, it is possible to obtain the impedance spectrum of each electroactive material. To confirm the effectiveness of these impedance measurements, we compared the sum of anode vs. reference electrode and cathode vs. reference electrode impedance measurements with the full impedance spectra (anode-reference), Fig. 4.4 (b). For the $LiCoO_2$-Graphite

Li-ion cell, a difference of 1.93% was found between the sums of electroactive materials vs. reference electrode impedance measurements and full cell impedance measurements in the real part (Z') and 8.53% in the imaginary part (Z''). For the $LiMn_2O_4$-Graphite Li-ion cell, a difference of 1.19% and 2.16% were found in the real part and imaginary part respectively.

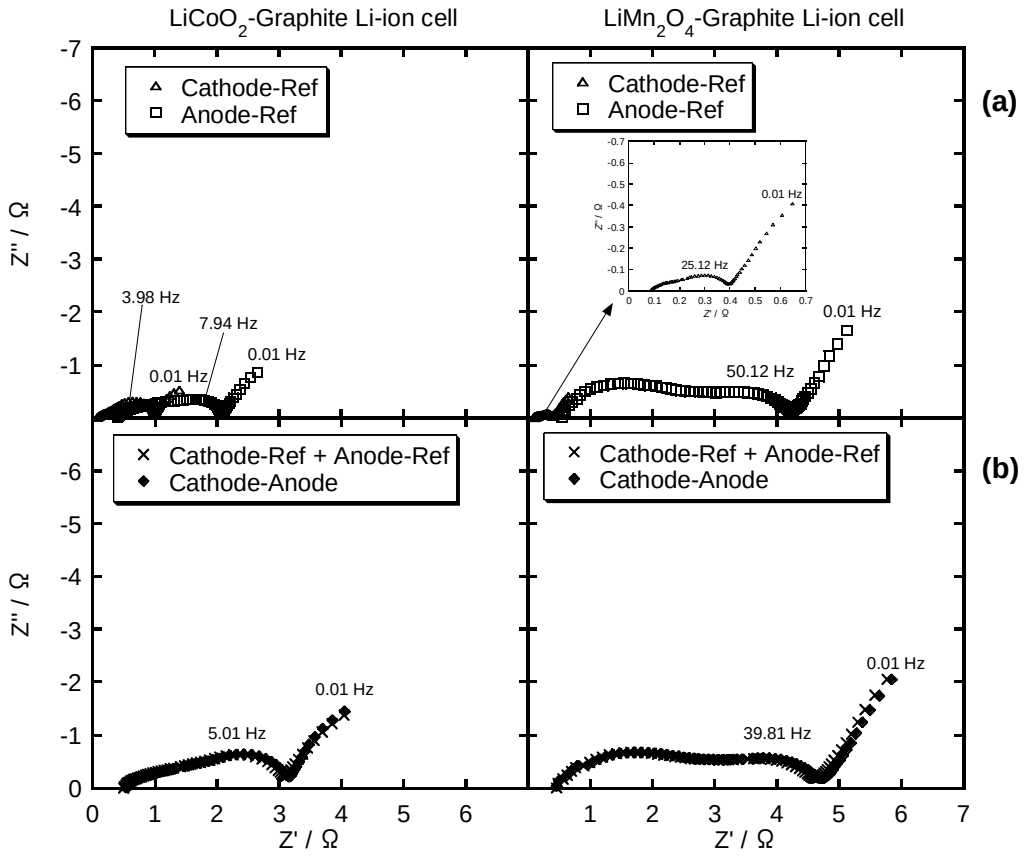

Fig. 4.4 (a) Impedance spectra of the cathode electroactive material vs. reference electrode and anode electroactive material vs. reference electrode; (b) comparison between the anode-cathode spectra and the sum of cathode-reference and anode-reference impedance measurements of the $LiCoO_2$-Graphite Li-ion cell and $LiMn_2O_4$-Graphite Li-ion cell at 20℃ and at 50% SOC.

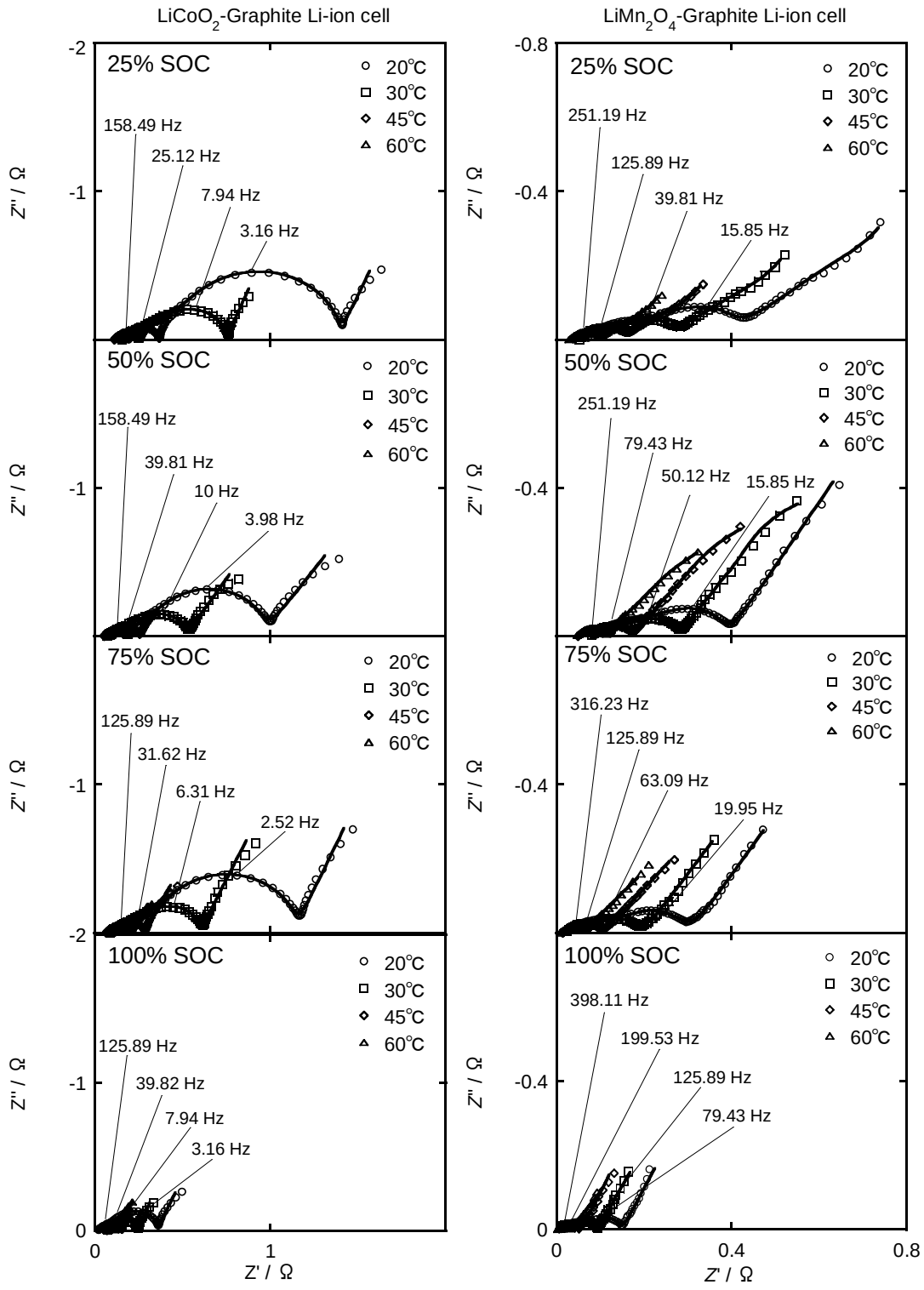

Fig. 4.5 Impedance spectra for the cathode electroactive material vs. reference electrode of the $LiCoO_2$-grahite Li-ion cell and $LiMn_2O_4$-graphite Li-ion cell at 25, 50, 75, 100% SOC and at 20, 30, 45 and 60℃.

Fig. 4.5 shows the impedance spectra for the $LiCoO_2$ and $LiMn_2O_4$ cathode materials vs. reference electrode at 25, 50, 75 and 100% SOC and at 20, 30, 45 and 60℃. Three main reactions take place on the solid electrolyte interphase (SEI) generated around the electroactive material, shown in Fig. 4.6. R_s corresponds to the resistance of the electrolyte. R_{sl1} is the resistance of Li-ion conduction in the SEI, and CPE_{sl1} represents the space charge capacitance of the SEI. R_{sl2} is the resistance of the Li-ion solvation/desolvation, and C_{sl2} corresponds to the solvation/desolvation capacitance. R_{ct} corresponds to the charge transfer resistance at the surface of the cathode active material, and CPE is a constant phase element. CPE was used to take into account the roughness of the cathode material surface. Z_w represents the Warburg resistance due to the Li-ion diffusion in the anode particle.

Impedance spectra fittings were carried out using the equivalent circuit shown in Fig. 4.7. During the impedance spectra fitting, we followed a rigorous method to obtain the best possible fit from the experimental data. Zview 2 software (Scribner Associates Inc.) was used to carry out the impedance spectra fittings. The chi-squared function (χ^2) delivers a good indication of the quality of the fitting [16]. The χ^2 values of 10^{-5} – 10^{-4} show a reasonably good fit. The values of χ^2 in this study were in the range of 10^{-4}.

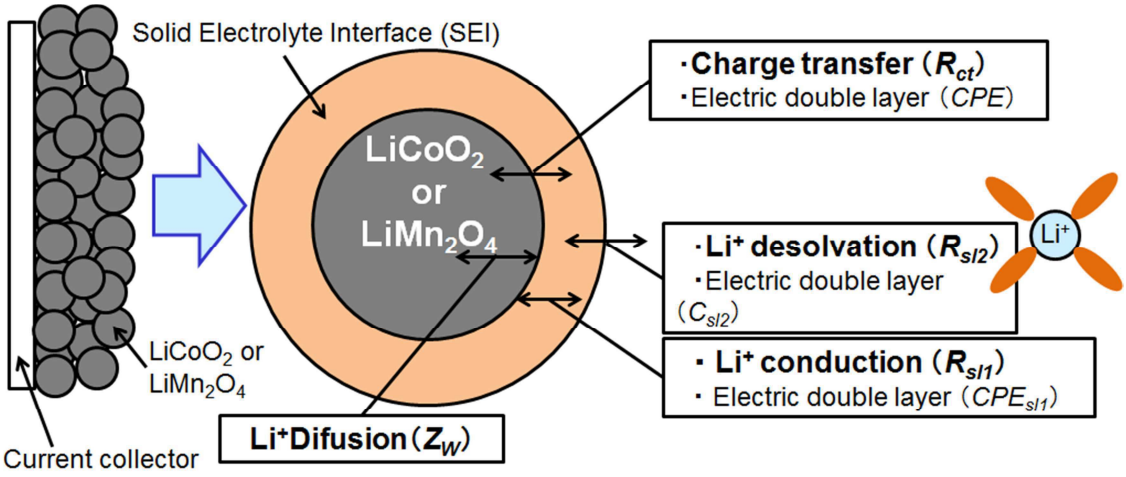

Fig. 4.6 Single particle model of interphase reactions around solid electrolyte interphase.

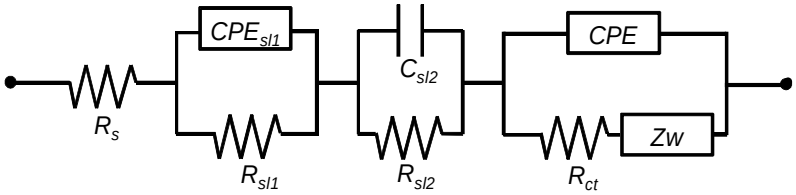

Fig. 4.7 Equivalent circuit used for the cathode impedance spectra fittings. R_s, R_{sl1}, R_{sl2} and R_{ct} correspond to electrolyte, lithium ion conduction, lithium ion desolvation and charge transfer resistances, respectively.

4.3.3 Kinetic Analysis of $LiCoO_2$ and $LiMn_2O_4$ cathode materials

Figure 4.7 shows the Arrhenius plots of Li^+ conduction (R_{sl1}), Li^+ desolvation (R_{sl2}) and charge transfer (R_{ct}) reactions at 50% state of charge of $LiCoO_2$ (a) and $LiMn_2O_4$ (b) cathode materials. Arrhenius plots are made by plotting the resistance values obtained from the experimentally fitted data at different temperatures using the expression (1) [10]

$$\frac{RT}{nFR_{rct}} = k_0' exp\left(\frac{-E_a}{RT}\right) \qquad (1)$$

where E_a is the activation energy, k'_0 is the pre-exponential factor, R_{rct} is the reaction resistance, n is the reaction electrode, F is the Faraday constant, T is the absolute temperature and R is the gas constant. Kinetic characteristics of the $LiCoO_2$ and $LiMn_2O_4$ Li-ion insertion/deinsertion reactions were obtained at different SOCs. The cathode potential of the Li-ion cells versus reference electrode was measured at each SOC.

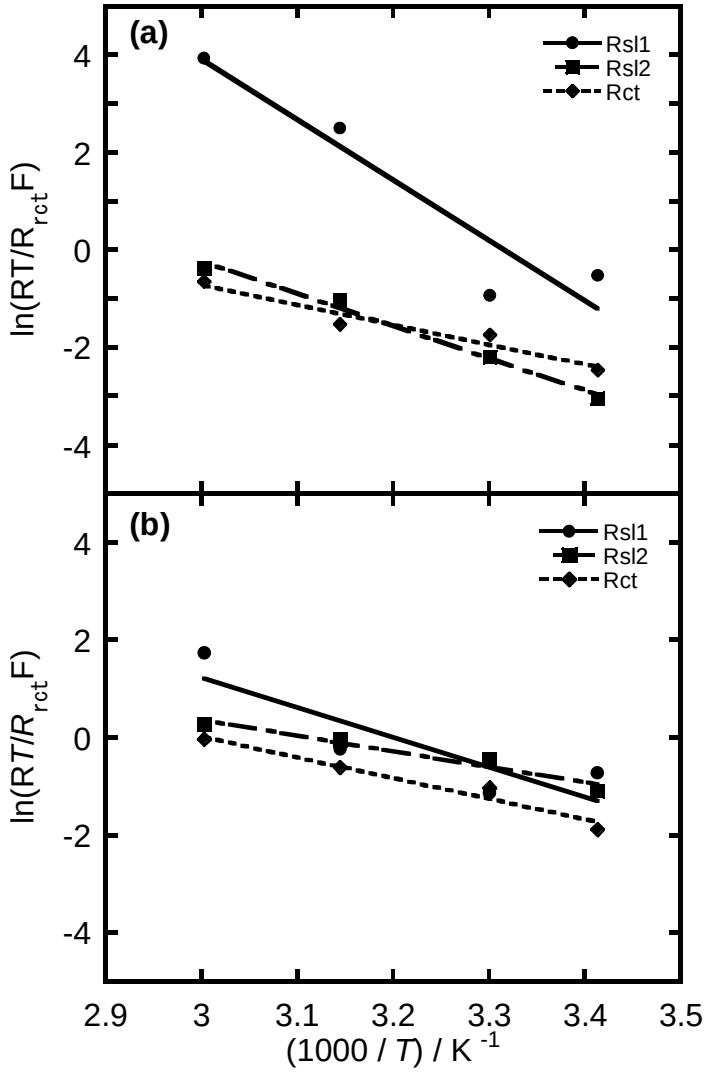

Fig. 4.7 Arrhenius plots of Li^+ conduction (R_{sl1}), Li^+ desolvation (R_{sl2}) and charge transfer (R_{ct}) reactions at 50% state of charge of $LiCoO_2$ (a) and $LiMn_2O_4$ (b) cathode materials.

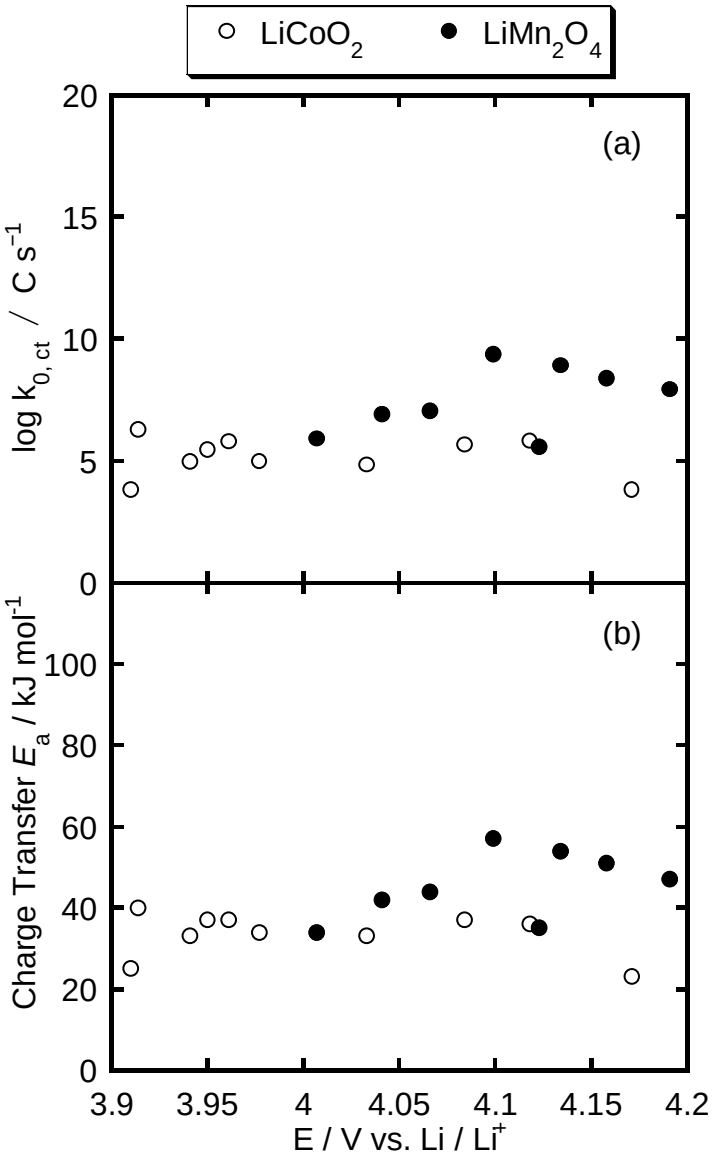

Fig. 4.8 Pre-exponential factor (a) and activation energy (b) of charge transfer reactions of $LiCoO_2$ and $LiMn_2O_4$ cathode materials as a function of cathode potential.

Fig. 4.8 shows the pre-exponential factor and activation energy of charge transfer reactions of $LiCoO_2$ and $LiMn_2O_4$ cathode materials as a function of cathode potential. The behaviors of activation energy and pre-exponential factor of $LiCoO_2$ change in a similar way. In the potential range of 3.90 – 3.95 V vs. Li/Li^+, the activation energy and frequency factor change without any clear tendency, while they remain

constant in the potential range of 3.95 – 4.10 V vs. Li/Li^+. The crystal structure of $LiCoO_2$ was reported to change from hexagonal-I to hexagonal-II forming an unstable transition phase, whereas the crystal structure remains hexagonal-II in the potential range of 3.95 - 4.10 V vs Li/Li^+ [3]. The constant behavior of the activation energy and pre-exponential factor between 3.95 and 4.10 V vs. Li/Li^+ seems to reflect the stability of the crystal structure of hexagonal-II. As in the case of $LiCoO_2$, the behavior of activation energy and pre-exponential of $LiMn_2O_4$ changes in a similar way. In the potential range of 4.01 – 4.07 V vs Li/Li^+, the activation energy and pre-exponential remain constant. In the potential range of 4.1 – 4.19 V vs Li/Li^+, the activation energy and pre-exponential tend to change in two ways. Li-ion insertion/deinsertion reactions in $LiMn_2O_4$ appear to occur in two stages due to the formation of two phases, where the lattice parameter of $LiMn_2O_4$ tends to change in two ways [15]. The formation of these two phases affects the kinetic behavior of Li-ion insertion/deinsertion reactions.

Fig. 4.9 shows the frequency factor and activation energy of Li-ion conduction reactions of $LiCoO_2$ and $LiMn_2O_4$ cathode materials as a function of cathode potential. The frequency factor and activation energy change with cathode potential without following a clear tendency. Since the solid electrolyte interphase (SEI) generated around the cathode materials is thinner, comparing with that generated around the anode materials [17], the change with potential of the frequency factor and activation energy of Li-ion conduction in $LiCoO_2$ and $LiMn_2O_4$ cathode materials, suggests that the structural changes of the cathode materials affect the Li-ion conduction reactions.

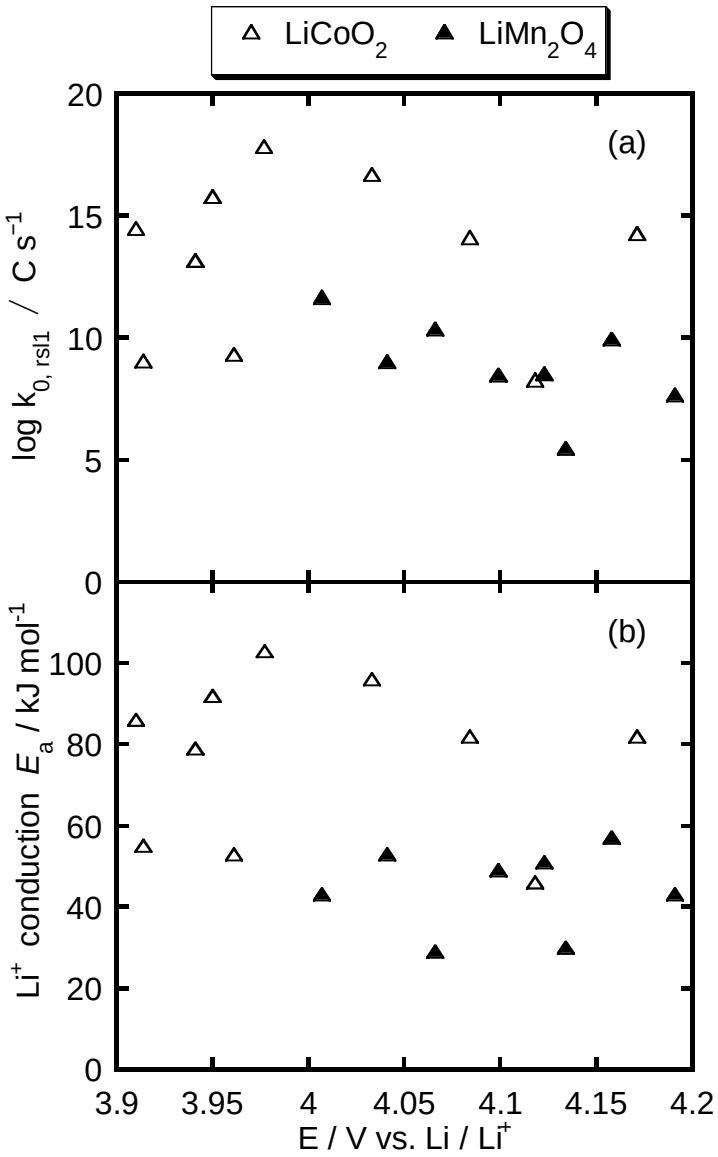

Fig. 4.9 Pre-exponential factor (a) and activation energy (b) of Li-ion conduction reactions of $LiCoO_2$ and $LiMn_2O_4$ cathode materials as a function of cathode potential.

Meyers et al., developed a mathematical model to describe the impedance response of a single particle surrounded by a resistance film [18], they established that charge transfer and double layer charging across each interface (particle/film and film/solution) must be considered. Charge transfer and Li-ion conduction correspond to the reactions that occur in the interface between cathode electroactive materials and SEI, therefore, Li-ion

solvation/desolvation correspond to the reactions in the interface between the SEI and electrolyte. Fig. 4.10 shows the pre-exponential factor and activation energy of Li-ion solvation/desolvation of $LiCoO_2$ and $LiMn_2O_4$ as a function of cathode potential. The frequency factor and activation energy of $LiCoO_2$ and $LiMn_2O_4$ tend to follow a constant behavior. A nearly constant behavior is expected due to the Li-ion solvation/desolvation reactions are not affected by the change in cathode potential.

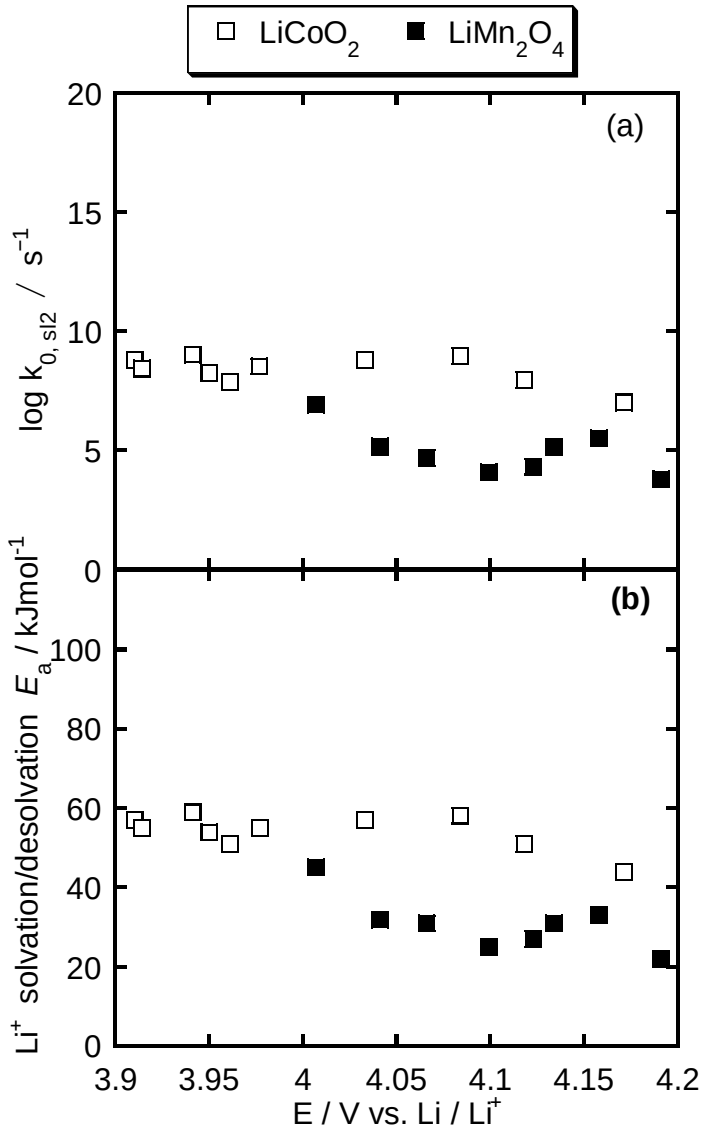

Fig. 4.10 Pre-exponential factor (a) and activation energy (b) of Li-ion solvation/desolvation reactions of $LiCoO_2$ and $LiMn_2O_4$ cathode materials as a function of cathode potential.

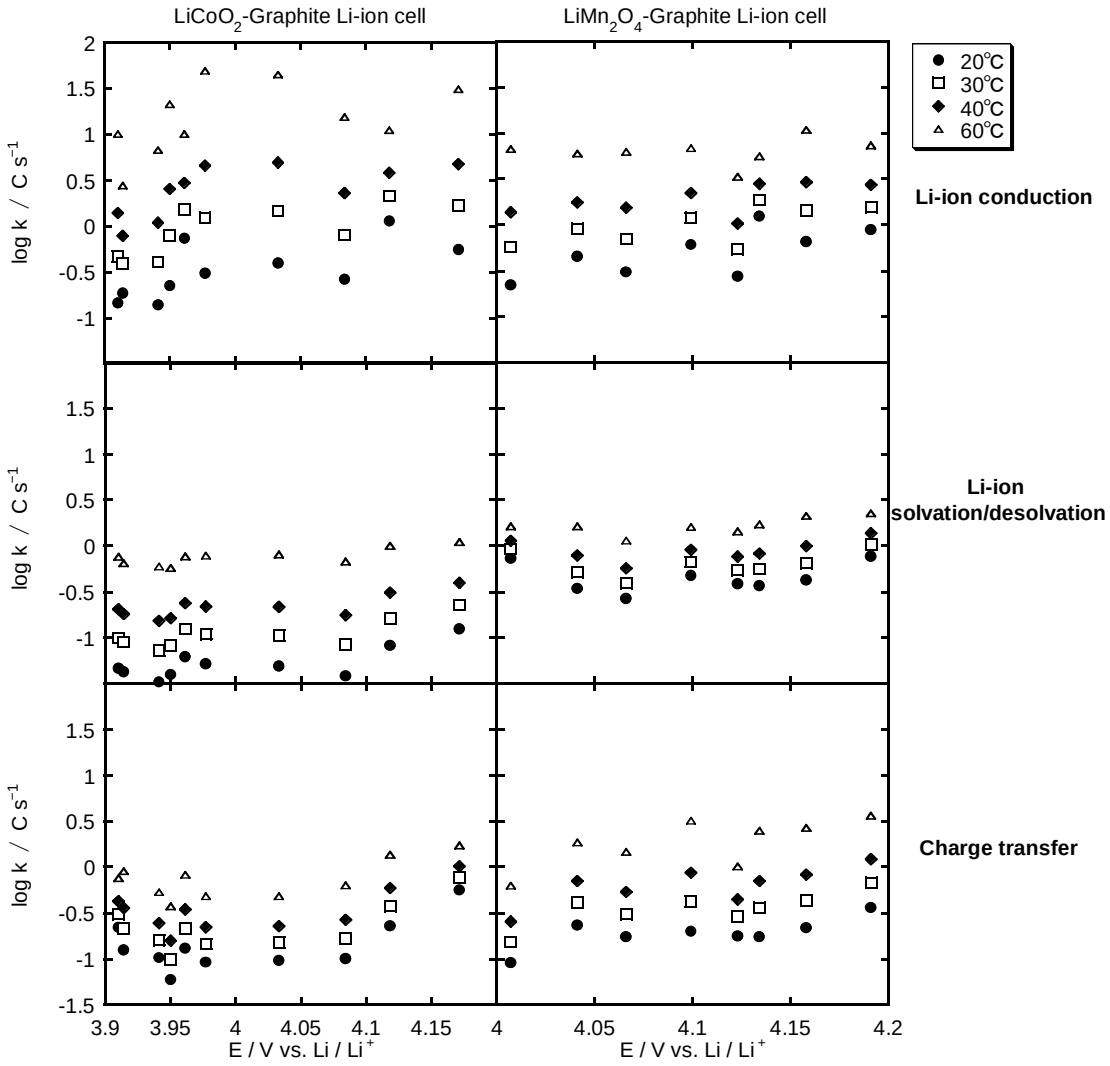

Fig. 4.11 Reaction rate constant of Li-ion conduction, Li-ion solvation/desolvation and charge transfer reactions of $LiCoO_2$ and $LiMn_2O_4$ cathode materials as a function of cathode potential.

Fig. 4.11 shows the reaction rate constants of Li-ion conduction, Li-ion solvation/desolvation and charge transfer reactions of $LiCoO_2$ and $LiMn_2O_4$ cathode materials as a function of cathode potential. The reaction rate constants were obtained by using the Arrhenius equation (2)

$$k = k'_0 \exp(-E_a/RT) \qquad (2)$$

where k is the reaction rate constant, E_a is the activation energy, k'_0 is the frequency

factor, T is the absolute temperature and R is the gas constant. The reaction rate constants were obtained at 20, 30, 40 and 60℃. The reaction rate constant of Li-ion conduction reactions of $LiCoO_2$ is larger than that of $LiMn_2O_4$, the SEI generated around $LiCoO_2$ electroactive material seems to be more thermally sensible than the one generated at $LiMn_2O_4$. The reaction rate constant of Li-ion solvation/desolvation reactions does not show big changes with temperature in comparison with that of Li-ion conduction. The reaction rate constants of charge transfer reactions of $LiCoO_2$ and $LiMn_2O_4$ electroactive materials change in a similar way, these do not exhibit big changes with temperature in comparison with that of Li-ion conduction reactions.

4.3.4 Comparison of the cathode apparent activation energy of $LiCoO_2$ and $LiMn_2O_4$ electroactive materials

Cathode apparent activation energy of $LiCoO_2$ and $LiMn_2O_4$ electroactive materials is obtained by making Arrhenius plots using a total resistance value (R_{total}) of each electroactive material. R_{total} is obtained by adding the resistance values of charge transfer, Li-ion conduction and Li-ion solvation/desolvation reactions. Fig. 4.12 shows the cathode apparent activation energy of $LiCoO_2$ and $LiMn_2O_4$, both electroactive materials exhibit a nearly constant behavior. These values of activation energy are consistent with data that has been previously reported for $LiCoO_2$ and $LiMn_2O_4$ [11, 19].

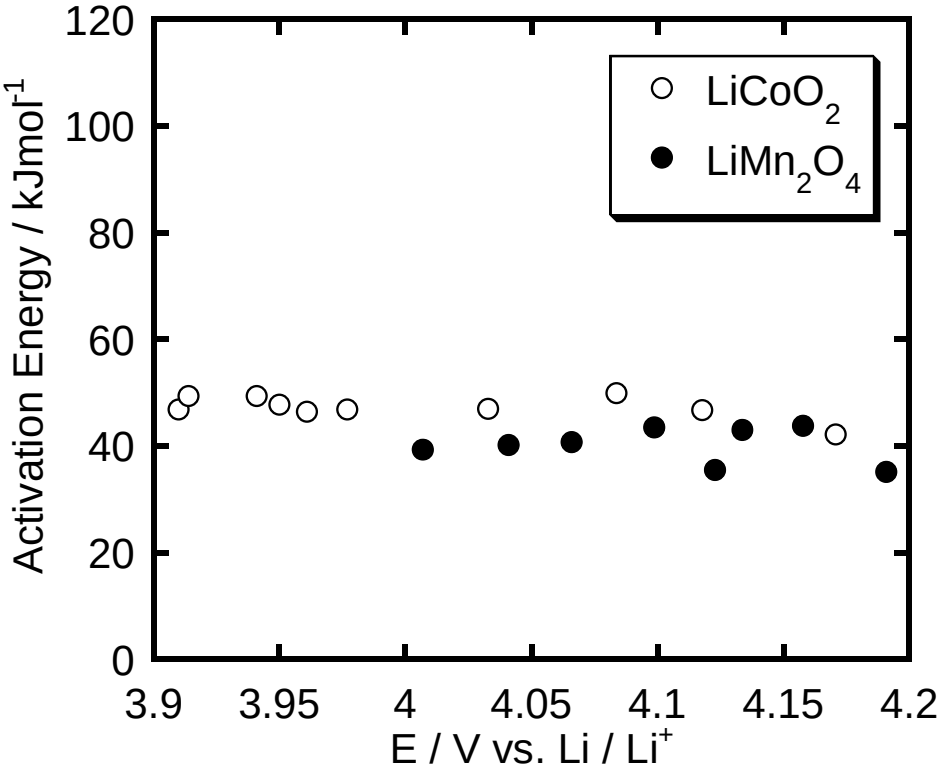

Fig. 4.12 Cathode apparent activation energy of $LiCoO_2$-Graphite and $LiMn_2O_4$-Graphite Li-ion cells as a function of cathode potential.

4.4 Conclusions

By carrying out EIS and chronopotentiometric measurements, using Li-ion secondary cells incorporating a reference electrode, the kinetic characteristics of $LiCoO_2$ and $LiMn_2O_4$ at different SOCs and temperatures were studied. It was to analyze kinetic characteristics of $LiCoO_2$ and $LiMn_2O_4$ as a function of cathode potential. The kinetic behavior of Li-ion conduction, Li-ion solvation/desolvation and charge transfer reactions of $LiCoO_2$ and $LiMn_2O_4$ and its dependency on the structural changes of cathode materials are studied. The charge transfer and Li-ion conduction reactions exhibit a dependency on the structural changes of cathode materials, while

Li-ion solvation/desolvation reactions do not.

According to the behavior of reaction rate constant for Li-ion conduction reactions of $LiCoO_2$ and $LiMn_2O_4$, the SEI generated around $LiCoO_2$ electroactive material seems to be more thermally sensible than the one generated at $LiMn_2O_4$.

References

[1] M. S. Dresselhaus, G. Dresselhaus, Adv. in Phys. 51 (1) (2002) 1.

[2] T. Ohzuku, Y. Iwakoshi, K. Sawai, J. Electrochem. Soc. 140 (1993) 2490.

[3] J. N. Reimers, J. R. Dahn, J. Electrochem. Soc. 139 (1992) 2091.

[4] J. Choi, A. Manthiram, Solid State Ionics 176 (2005) 2251.

[5] G. Li, Z. Lu, B. Huang, H. Huang, Solid State Ionics 81 (1995) 15.

[6] K. Dokko, M. Mohamedi, Y. Fujita, T. Itoh, M. Nishikawa, M. Umeda, I. Uchida, J. Electrochem. Soc. 148 (2001) A422.

[7] M. Umeda, K. Dokko, Y. Fujita, M. Mohamedi, I. Uchida, J. R. Selman, Electrochim. Acta. 47 (2001) 885.

[8] K. Dokko, Y. Fujita, M. Mohamedi, M. Umeda, I. Uchida, J. R. Selman, Electrochim. Acta. 47 (2001) 933.

[9] V. Malave, J. R. Berger, H. Zhu, R. J. Kee, Electrochim. Acta. 130 (2014) 707.

[10] P. Suresh, A. K. Shukla, N. Munichandraiah, J. Appl. Electrochem. 32 (2002) 267.

[11] T. Hang, D. Mukoyama, H. Nara, N. Takami, T. Momma, T. Osaka, J. Power Sources. 222 (2013) 442.

[12] O. S. Mendoza-Hernandez, H. Ishikawa, Y. Nishikawa, Y. Maruyama, Y. Sone, M. Umeda, Electrochim. Acta. 131(2014) 168.

[13] J. S. Hong, J. R. Selman, J. Electrochem. Soc. 147(2000) 3183.

[14] K. Dokko, M. Mohamedi, M. Umeda, I. Ichida, J. Electrochem Soc. 150 (2003) A425.

[15] W. Lui, K. Kowal, G. C. Farrington, J. Electrochem. Soc. 145 (1998) 459.

[16] B. A. Boukamp, Solid State Ionics. 20 (1986) 31.

[17] J. Lei, L. Li, R. Kostecki, R. Muller, F. McLarnon, J. Electrochem. Soc. 152 (2005) A774.

[18] J. P. Meyers, M. Doyle, R. M. Darling, J. Newman, J. Electrochem. Soc. 147 (2000) 2930.

[19] H. Ishikawa, O. Mendoza, Y. Sone, M. Umeda, J. Power Sources 198 (2012) 236.

Chapter 5 “Cathode Material Comparison of Thermal Runaway Behavior of Li-ion Cells at Different State of Charges Including Over Charge”

5.1 Introduction

The use of Li-ion cells has been growing globally with a large number of cells powering a wide range of applications in different environments, and there have been several reported incidents raising safety concerns. Some of the cases have been related to overheating (thermal runaway) of Li-ion cells, leading to possible fire and explosion. The thermal behavior of a Li-ion cell is dominated by the exothermic reactions between the electrolyte and electroactive materials [1-3]. Thermal runaway occurs when the exothermic reactions go out of control, thus the self-heating rate of the cell increases to the point that it begins to generate more heat than what can be dissipated [4, 5].

There are safety concerns related to the upsizing of Li-ion cells and the use of oxide based cathode materials, since oxygen release from the cathode material at high temperatures can accelerate the combustion reactions in the cell driving its components into fire or explosion. Therefore, the thermal analysis of complete Li-ion secondary cells is important for ensuring their safety and reliability.

The use of accelerating rate calorimetry (ARC) allows the thermal analysis of Li-ion cells. Many researchers have investigated the thermal behavior of different cathode materials in contact with different solvents and electrolytes using ARC [2, 3, 5-9], however, a few results on the thermal behavior using complete Li-ion cells have been reported.

There are a few investigations on the thermal behavior of complete Li-ion cells [10, 11], and the analysis of cathode electroactive materials under outstanding conditions, as overcharge and high temperatures, is important to determine thermal

abuse characteristics of electroactive materials and precise risk assessments on Li-ion cells. In this work, the thermal runaway behavior of two widely used cathode materials in commercial Li-ion cells, $LiCoO_2$ (LCO) and $LiMn_2O_4$ (LMO), is compared at different state of charges including overcharge (120% SOC), using 18650 Li-ion cells and carrying out ARC measurements. In parallel with the ARC measurements, the internal resistance and open circuit voltage (OCV) of the cells were monitored. We were able to identify non-self-heating, self-heating and thermal runaway regions of LCO and LMO cells as a function of state of charge and temperature.

5.2 Experimental methodology

5.2.1 Li-ion cell specifications

Two types of commercial 18650 Li-ion cells with different cathode materials were used in this work. The first type used $LiCoO_2$ as cathode active material and graphite as anode active material (LCO-Graphite cell). The second type used $LiMn_2O_4$ (LMO) as cathode active material and graphite as anode active material (LMO-Graphite cell). The electrolyte consisted of a solution of 1 M of $LiPF_6$ in ethylene carbonate and dimethyl carbonate (1:1, w/w). The information of the composition of electroactive materials and electrolyte was taken from the corresponding Li-ion cell data sheet. The capacity of LCO-Graphite cell was 800 mAh and the capacity of the LMO-Graphite cell was 720 mAh.

5.2.2 Accelerating rate calorimetry

Before carrying out the ARC measurements, the cells were charged to the desired state of charge using a battery tester (KIKUSUI, PFX2011). Thermal runaway tests were carried out using an accelerating rate calorimeter (ARC) 2000^{TM} Columbia Scientific Industries. The cells were set to the desired SOC and placed inside the ARC

cavity. It is considered that a cell is full charged, 100% SOC, when this is charged to 4.1 V (defined by the cell manufacturer), using a charging current of 0.2 C and following a constant current–constant voltage (CC-CV) process, Fig. 5.1. To set the cells to the desired SOC, the cells were fully charged and then discharged to the corresponding SOC using a discharging current of 0.2 C following a constant current (CC) process. In the case of 120% SOC, the cells were fully charged to obtain their charging capacity, and then they were charged 20% according to the charging capacity obtained.

To record the temperature of the cell, a thermocouple was placed on the surface of this. The calorimetry measurements were conducted following a Heat-Wait-Search method. During the heat-step, the cell is heated in periods of 5 °C follow by a waiting-step of 30 min and a searching-step of 5 min. If during the searching-step, a self-heating with a heating rate higher than 0.05 °C min^{-1} is detected, the calorimeter shifts to adiabatic mode and tracks the cell temperature until the end the self-heating reaction. If no self-heating is detected, the next heat-step is immediately initiated. The thermal runaway measurements were carried out until surface of the cell reached a temperature of 200 °C. The ARC measurements were carried out at 0%, 25%, 50%, 75%, 100% and 120% SOC.

In parallel with the ARC measurements, the internal resistance at 1 kHz and the OCV of the cells were recorded using a milliohmmeter (Agilent 4338B) and a multimeter (Keithley 2100), respectively.

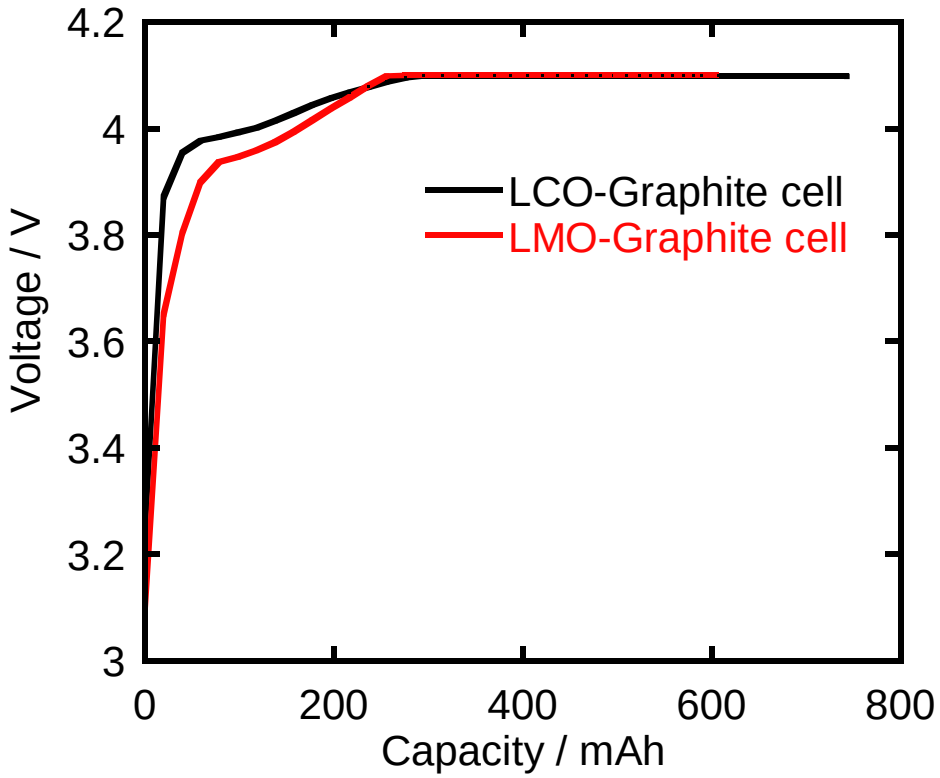

Fig. 5.1 Charging curves of LCO-Graphite and LMO-Graphite cells.

5.3 Results and discussion

Fig. 5.2 shows the thermal behavior of the LCO-Graphite cell during the ARC measurements at 0%, 25%, 50%, 75%, 100% and 120% SOCs. A temperature drop is observed at some SOCs, this drop in temperature is likely due to the volatilization of the electrolyte. A temperature drop is not observed when the heat generated by the cells is larger than the heat released by the volatilization of the electrolyte. Table 5.1 shows the onset temperatures of self-heating and thermal runway reactions of LCO-Graphite cell at different SOCs. The onset temperatures decrease by increasing the state of charge. The differences of the onset temperatures of the self-heating reactions are due to the influence of the state of charge on the thermal stability of the electroactive materials, where highly delithiated electroactive materials become more reactive [12, 13]. At 50%,

75%, 100% and 120% SOCs, self-heating reactions were followed by a thermal runaway behavior.

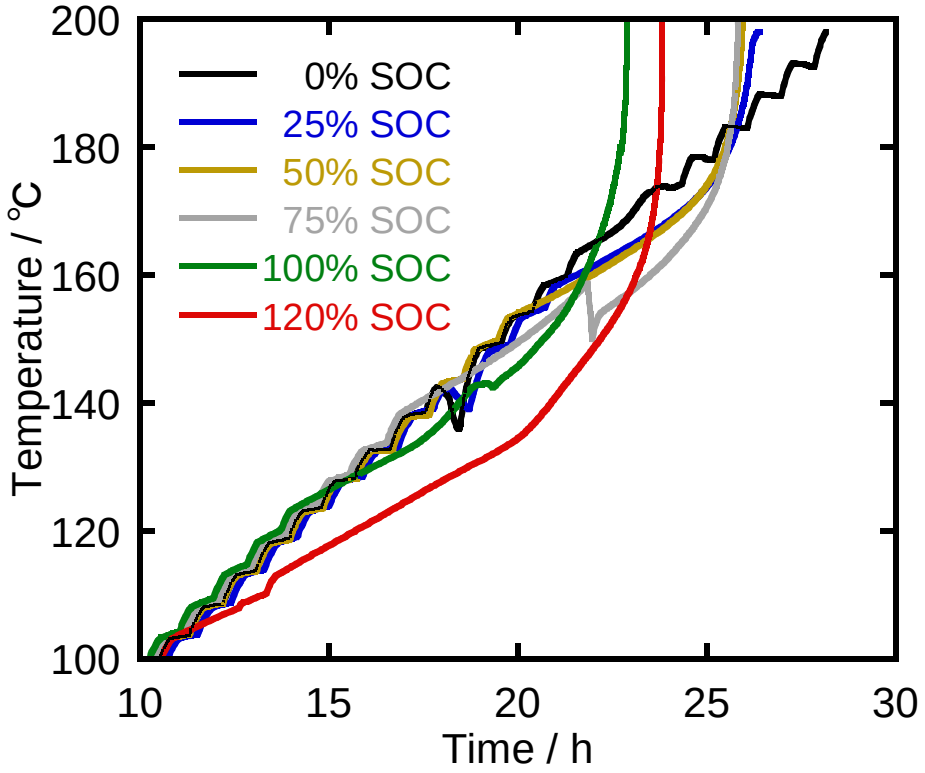

Fig. 5.2 ARC measurements of LCO-Graphite cell at 0%, 25%, 50%, 75%, 100% and 120% SOC.

Table 5.1 Onset temperatures of self-heating and thermal runaway reactions of LCO-Graphite cells

SOC (%)	Onset temperature of self-heating (°C)	Onset temperature of Thermal runaway (°C)
0	165.3	-
25	159.8	-
50	155.1	191.8
75	140.1	189.1
100	124.9	182.2
120	116.5	176.4

Fig. 5.3 shows the thermal behavior of the LMO-Graphite cell during the ARC measurements at 0%, 25%, 50%, 75%, 100% and 120% SOCs. As in the case of LCO-Graphite cells, a temperature drop is observed at some SOCs. Table 5.2 shows the onset temperatures of self-heating and thermal runway reactions of LMO-Graphite cell at different SOCs. At 0% SOC, self-heating and thermal runaway reactions are not observed. Self-heating reactions were followed by a thermal runaway behavior at 75%, 100% and 120% SOCs.

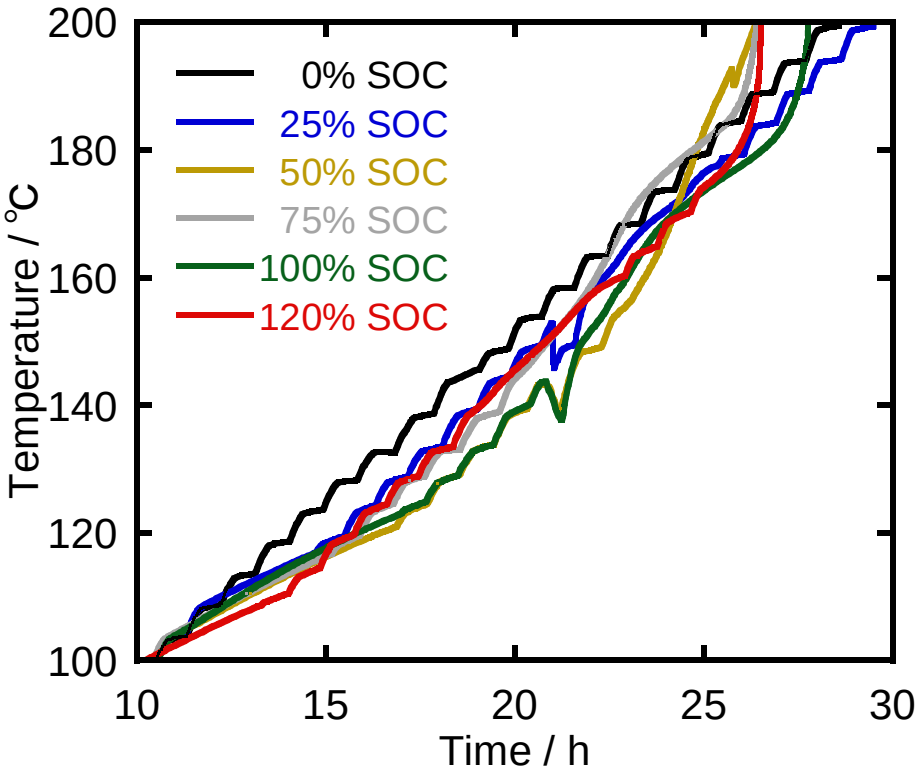

Fig. 5.3 ARC measurements of LMO-Graphite cell at 0%, 25%, 50%, 75%, 100% and 120% SOC.

Table 5.2 Onset temperatures of self-heating and thermal runaway reactions of LMO-Graphite cells

SOC (%)	Onset temperature of the first self-heating (°C)	Onset temperature of the second self-heating (°C)	Onset temperature of Thermal runaway (°C)
0	-	-	-
25	109.9	160.7	-
50	104.9	156.8	-
75	104.9	146.6	199.7
100	104.9	153.2	196.4
120	99.8	140.1	189.8

By comparing the thermal behaviors of LCO-Graphite and LMO-Graphite cells, some differences in the onset temperatures of self-heating and thermal runaway reactions are noticed. These differences are likely due to the amount of O_2 release by the cathode electroactive materials, which affects the combustion reactions in the cells [7, 14].

Figs. 5.4 and 5.5 show the heating rate vs. temperature of the LCO-Graphite and LMO-Graphite cells at 0%, 25%, 50%, 75%, 100% and 120% SOC. By comparing the heating rates of both cells, it is observed that the LCO-Graphite cell releases more heat than the LMO-Graphite cell. The heating rates at 0% SOC cannot be compared because self-heating reactions are not observed at this SOC. When the heating rate of a cell is higher than 0.05 °C min^{-1}, it is considered that a self-heating reaction has started. A thermal runaway behavior takes place when the self-heating rate of a cell is higher than 1 °C min^{-1} [2]. The LCO-Graphite cells exhibited a thermal runaway behavior from 50% to 120% SOC, while LMO-Graphite cells exhibited a thermal runaway behavior from 75% to 120% SOC. In the case of 120% SOC, overcharge, both cells presented a thermal runaway behavior, but there is a significantly difference between the onset

temperature of thermal runaway. The onset temperatures of thermal runaway behavior at 120% SOC of the LCO-Graphite and LMO-Graphite cells were 176.4 °C and 189.8 °C, respectively. The results shown in Fig. 4 and 5 suggest that although the anode-electrolyte reactions are initiated first, the kinetic reaction of the cathode-electrolyte dominates the thermal runaway behavior of the cells. LMO-Graphite cells exhibited a better thermal stability than that of LCO-Graphite cells, indicating that LMO cathode electroactive material is more thermally stable than LCO, even at overcharge conditions, which is consistent with previous reports [14-16]. The difference between the thermal stability between LCO and LMO cathode materials could be due to LMO tends to release less oxygen at high temperatures [14].

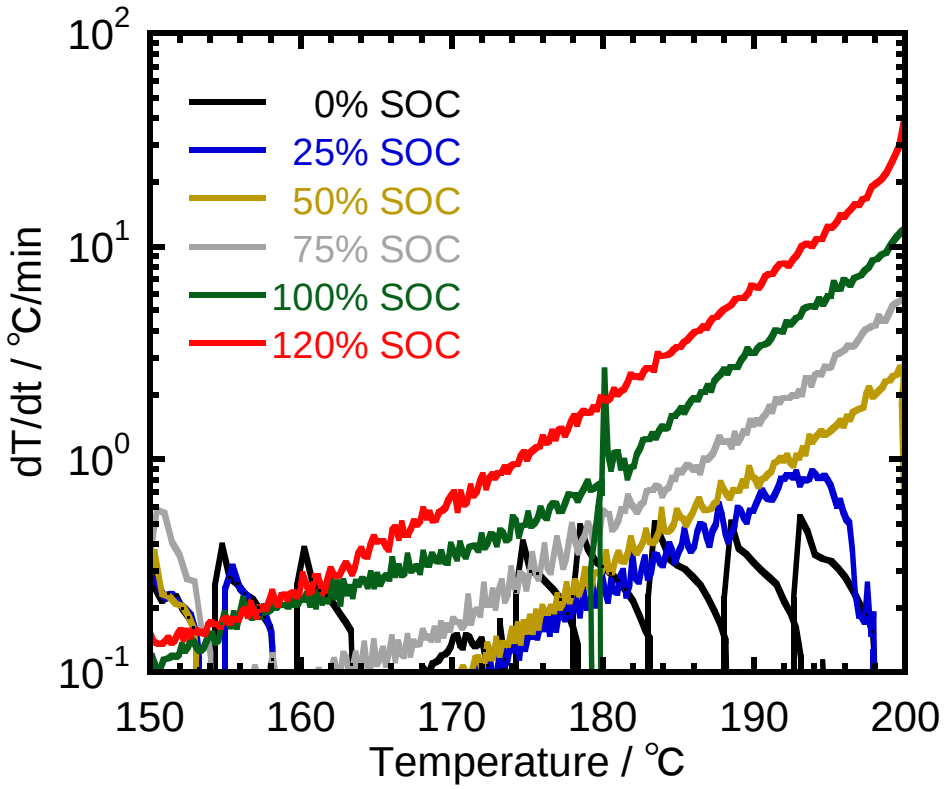

Fig. 5.4 Heating rate vs. temperature of LCO-Graphite cell at 0%, 25%, 50%, 75%, 100% and 120% SOC.

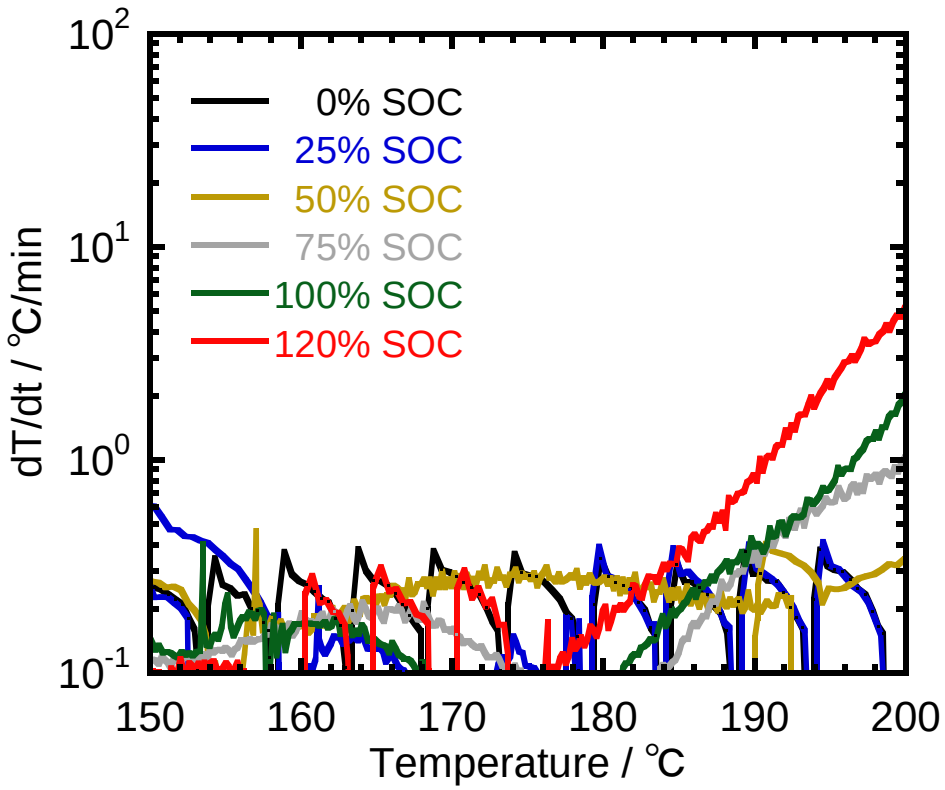

Fig. 5.5 Heating rate vs. temperature of LMO-Graphite cell at 0%, 25%, 50%, 75%, 100% and 120% SOC.

Figs. 5.6 and 5.7 show the thermal mapping plots of LCO-Graphite and LMO-Graphite cells as a function of SOC. By summarizing the ARC results, it is possible to distinguish non-self-heating (blue bars), self-heating (yellow bars) and thermal runaway (red bars) regions as a function of temperature and SOC. In the non-self-heating region, any exothermic reaction occurs. In the self-heating region, exothermic reactions with a heating rate larger than 0.05 °C min^{-1} occur. In the thermal runaway region, the heating rate is larger than 1 °C min^{-1} [2]. These plots are useful to compare the thermal characteristics of the LCO-Graphite and LMO-Graphite cells. In the thermal mapping of LCO-Graphite cell, figure 5.6, thermal runaway behavior is not observed at 0% and 25% SOC. It is noticed that the onset temperatures of self-heating reactions and thermal runaway decrease by increasing the SOC, which means that as

$LiCoO_2$ is more delithiated, the cell becomes more thermally unstable [14, 15]. In the thermal mapping of LMO-Graphite cell, figure 5.7, a thermal runaway behavior is not observed at 0%, 25% and 50% SOC and the onset temperatures of self-heating reactions and thermal runaway are almost constant, even at 120% SOC, reflecting the thermal stability of LMO.

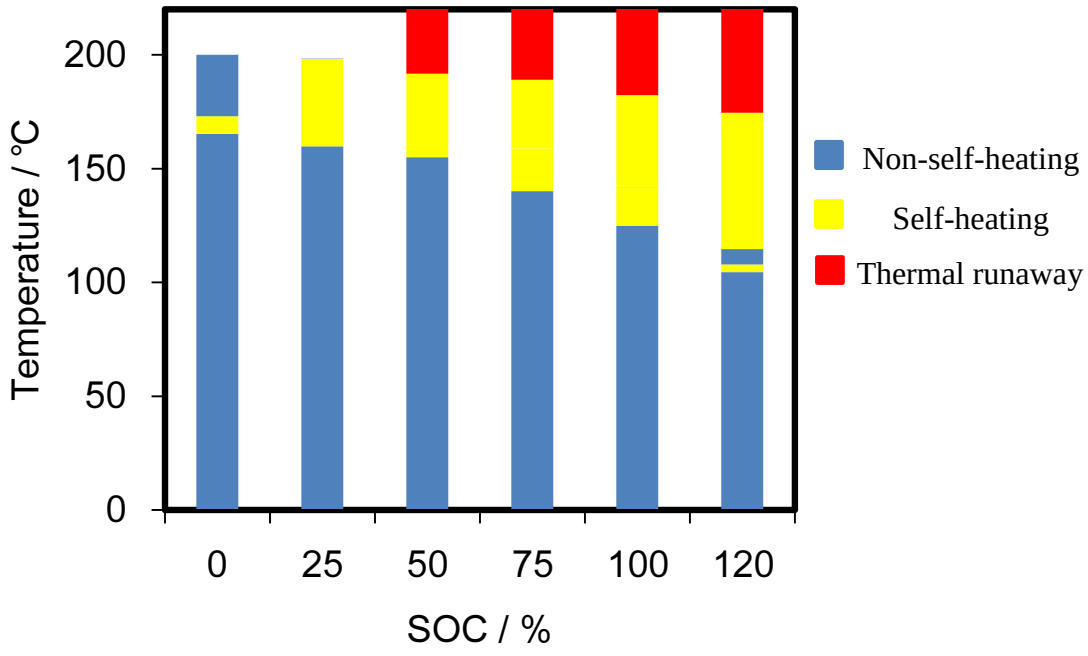

Fig. 5.6 Thermal mapping of LCO-Graphite cell as a function of SOC. Non-self-heating (blue), self-heating (yellow) and thermal runaway (red) regions are identified.

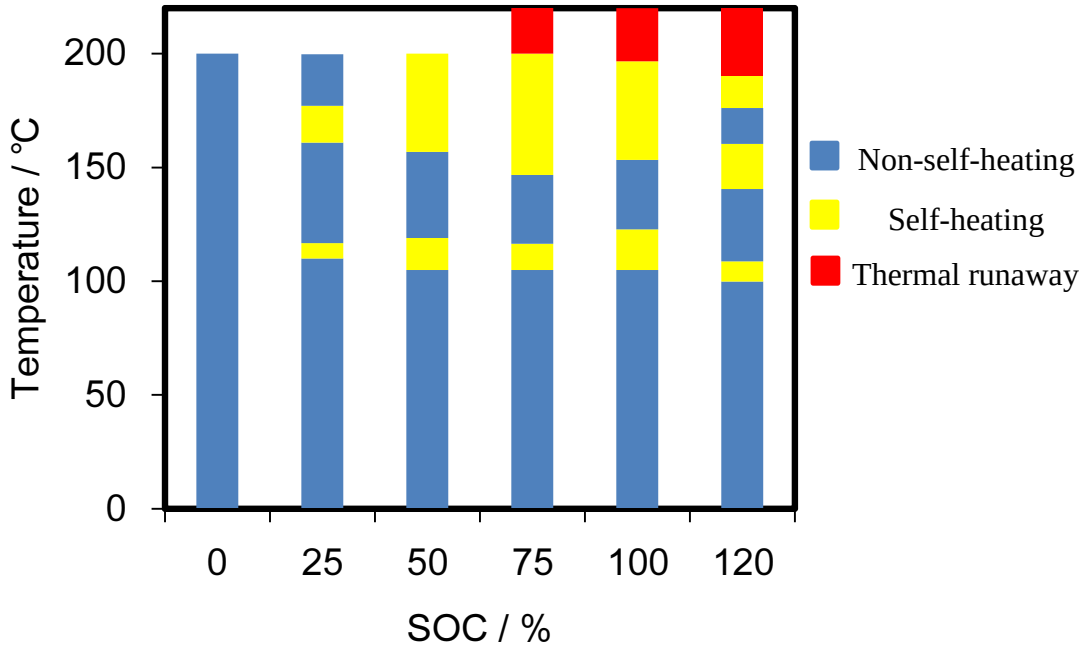

Fig. 5.7 Thermal mapping of LMO-Graphite cell as a function of SOC. Non-self-heating (blue), self-heating (yellow) and thermal runaway (red) regions are identified.

By comparing the figures 5.6 and 5.7, clear differences among the self-heating regions of LCO-Graphite and LMO-Graphite cells are noticed. In the case of LCO-Graphite cells a self-heating region is observed at each SOC, and the onset temperatures of these regions show a dependency on SOC. In the case of LMO-Graphite cells more than one self-heating region are observed from 25% to 120% SOCs, where the onset temperatures of the first self-heating regions are almost constant and the onset temperatures of the second self-heating regions present a slightly dependency on SOC.

Self-heating reactions occur when the SEI begins to react with the active material or electrolyte, this process generally takes place at the anode at a temperature above 120 °C [17], then the self-heating behavior is accelerated by the

cathode-electrolyte reactions and depending on the SOC a thermal runaway behavior occurs [15, 16], which is consistent with the self-heating regions of LCO-Graphite cell and the second self-heating regions of LMO-Graphite cell.

Before the SEI begins to decompose and react with the electrolyte or active materials, a first transformation takes place at around 105 °C, where some components of the SEI like lithium alkyl carbonates and semicarbonates convert to more stable ones [18]. The onset temperatures of the first self-heating regions observed for LMO-Graphite cells are almost constant, and these onset points coincide with the temperature of the first transformation of the SEI. According to this, the first self-heating regions of LMO-Graphite cells could be attributed to two possible reaction mechanisms: In the first one, when the SEI generated around the anode begins to transform some slightly exothermic reactions between the anode and LMO may take place. In the second one, the transformation of the SEI generated around LMO may occur exothermically.

Figs. 5.8 and 5.9 show the OCV and the internal resistance of the LCO-Graphite and LMO-Graphite cells as a function of temperature at 0%, 25%, 50%, 75%, 100% and 120% SOC. It is noticed that by increasing the temperature, the OCV decreases and the internal resistance increases. The OCV and the internal resistance start decreasing and increasing, respectively, at around 135 °C, this is likely due to the shutting down of the separator located between the cathode and anode materials [6,19]. A combination of polyethylene (158 °C melting point) and polypropylene (125 °C) materials are used as separator in this work [19-22]. The separator has many tiny holes and Li-ions pass through them. A separator shuts down when the melting point of this is reached, then the tiny holes of the separator are closed and there is no Li-ion transfer

between the electrodes, which causes a drop in the OCV and an increase in the internal resistance [23]. By comparing Fig. 5.8 and 5.9, some differences in the electrochemical behavior of the cells are noticed, which suggest that the state of charge and the type of cathode electroactive material are affecting the shutting down behavior of the cells.

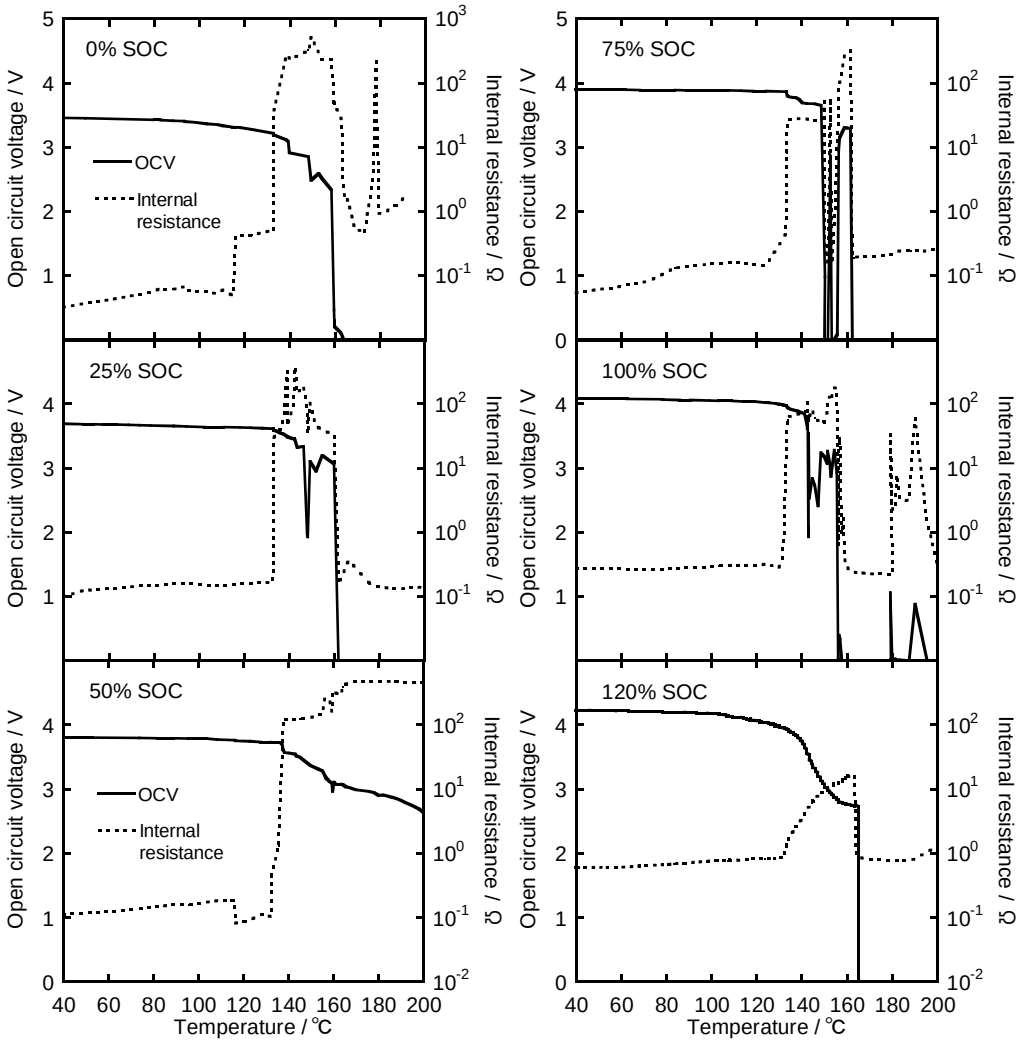

Fig. 5.8 Open circuit voltage and internal resistance of LCO-Graphite cell during ARC measurements as a function of temperature at 0%, 25%, 50%, 75%, 100% and 120% SOC.

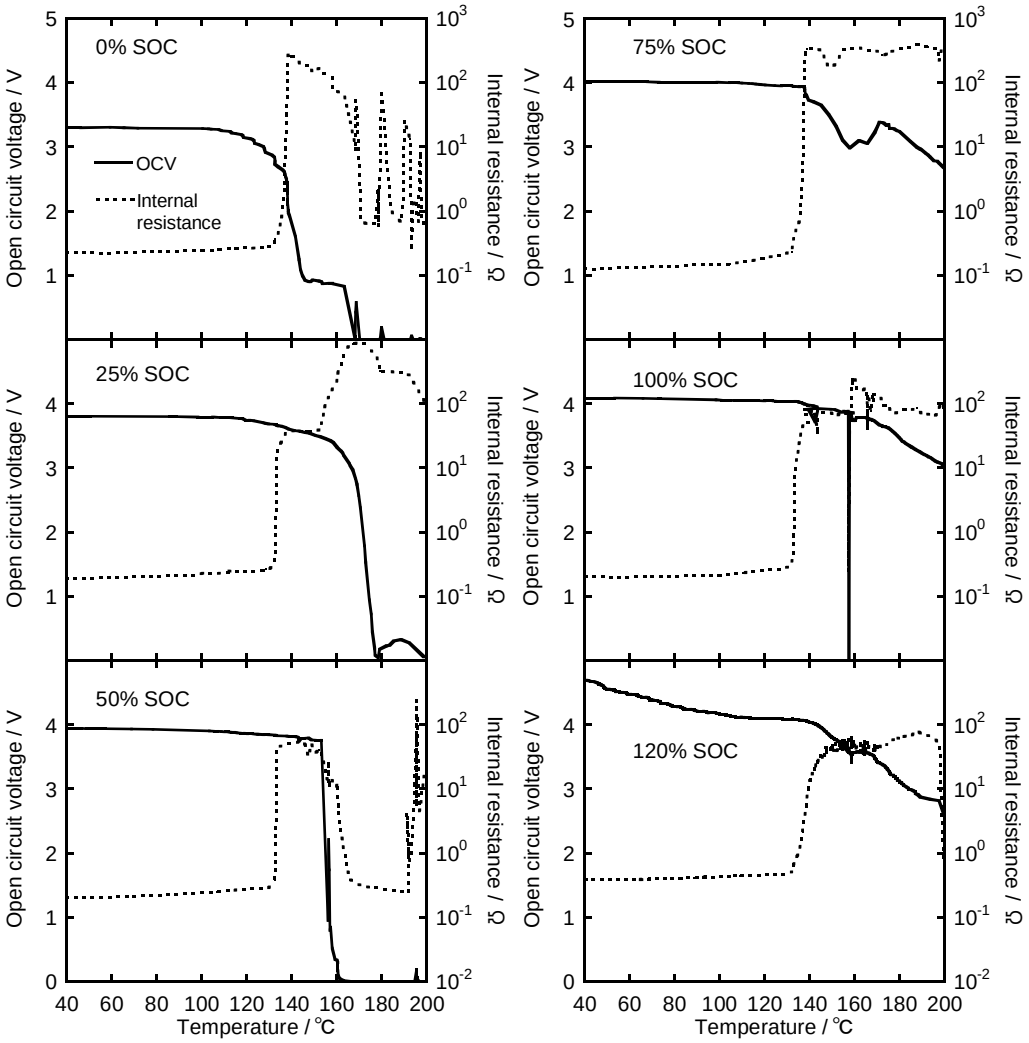

Fig. 5.9 Open circuit voltage and internal resistance of LMO-Graphite cell during ARC measurements as a function of temperature at 0%, 25%, 50%, 75%, 100% and 120% SOC.

5.4 Conclusions

By carrying out ARC measurements, the thermal behavior of $LiCoO_2$ and $LiMn_2O_4$ was compared using 18650 Li-ion cells. The ARC results were used to make thermal mapping plots, where non-self-heating, self-heating and thermal runaway regions are identified as a function of state of charge and temperatures. The use of thermal mapping plots allows a practical comparison of the thermal behaviors of the

cells. The cell using $LiCoO_2$ as cathode material was found to be more thermally unstable than the cell using $LiMn_2O_4$. Both cathode materials exhibited a thermal runaway behavior at overcharge, however, the onset temperature for $LiMn_2O_4$ was higher than that of $LiCoO_2$, suggesting that $LiMn_2O_4$ is relatively stable when it is highly delithiated.

In parallel with the ARC measurements, the OCV and internal resistance of the cells were monitored. By increasing the temperature, an increase in the internal resistance and a decrease in the OCV were noticed.

References

[1] T. D. Hatchard, D. D. MacNeil, A. Basu, J. R. Dahn, J. Electrochem. Soc. 148 (2001) A755-A761.

[2] I. Uchida, H. Ishikawa, M. Mohamedi, M. Umeda, J. Power Sources 119–121(2003) 821-825.

[3] J.S. Gnanaraj, E. Zinigrad, L. Asraf, H.E. Gottlieb, M. Sprecher, D. Aurbach, Schmidt, J. Power Sources 119–121 (2003) 794-798.

[4] R.M. Spotnitz, J. Weaver, G. Yeduvaka, D.H. Doughty, E.P. Roth, J. Power Sources 163 (2007) 1080–1086.

[5] B.K. Mandal, A.K. Padhi, Z. Shi, S. Chakraborty, R. Filler, J. Power Sources 161 (2006) 1341–1345.

[6] H. Ishikawa, O. Mendoza, Y. Sone, M. Umeda, J. Power Sources 198 (2012) 236-242.

[7] C.-Y. Jhu, Y.-W. Wang, C.-Y. Wen, C.-M. Shu, Appl. Energy 100 (2012) 127-131.

[8] A. Eddahech, O. Briat, J-M. Vinassa, Energy 61 (2013) 432-439.

[9] P. Roder, N. Baba, H. Wiemhofer, J. Power Sources 248 (2014) 978-987.

[10] H. Maleki, J. N. Howard, J. Power Sources 137 (2004) 117-127.

[11] Y. Saito, K. Takano, A. Negishi, J. Power Sources (2001) 693-696.

[12] Y. Furushima, C. Yanagisawa, T. Nakagawa, Y. Aoki, N. Muraki, J. Power Sources 196 (2011) 2260-2263.

[13] E. P. Roth, D. H. Doughty, J. Power Sources 128 (2004) 308-318.

[14] Z. Zhang, D. Fouchard, J. R. Rea, J. Power Sources 70 (1998) 16-20.

[15] D. D. MacNeil, Z. Lu, Z. Chen, J. R. Dahn, J. Power Sources 108 (2002) 8-14.

[16] E. P. Roth, D. H. Doughty, J. Franklin, J. Power Sources 134 (2004) 222-234.

[17] D. D. MacNeil, D. Larcher, J. R. Dahn, J. Electrochem. Soc. 146 (1999) 3596-3602.

[18] M. N. Richard, J. R. Dahn, J. Electrochem. Soc. 146 (1999) 2068-2077.

[19] G. Venugopal, J. Power Sources 101 (2001) 231-237.

[20] F. C. Laman, M. A. Gee, J. Denovan, J. Electrochem. Soc. 140 (1993) L51-L53.

[21] A. J. Bradley and R. E. White, J. Power Sources 70 (1998) 48-54.

[22] G. Venugopal, J. Moore, J. Howard, S. Pendalwar, J. Power Sources 77 (1999) 34-41.

[23] X. Liu, H. Kusawaka, S. Kuwajima, J. Power Sources 97-98 (2001) 661-663.

Chapter 6 “Thermal Runaway Behavior of Degraded and Non-degraded Commercial 18650 Li-ion Secondary Cells”

6.1 Introduction

The use of Li-ion cells has been growing globally with a large number of cells powering a wide range of applications in different environments, and there have been several reported incidents raising safety concerns. Some of the cases have been related to overheating (thermal runaway) of Li-ion cells, leading to possible fire and explosion. The thermal behavior of a Li-ion cell is dominated by the exothermic reactions between the electrolyte and electroactive materials [1-3]. Thermal runaway occurs when the exothermic reactions go out of control, thus the self-heating rate of the cell increases to the point that it begins to generate more heat than what can be dissipated [4, 5].

The use of accelerating rate calorimetry (ARC) allows the thermal analysis of Li-ion cells [2, 3, 5-9]. There are safety concerns related to the use of damaged or degraded Li-ion cells. Therefore, the thermal analysis of degraded Li-ion secondary cells is important for ensuring their safety and reliability. There are a few investigations on the thermal behavior of degraded Li-ion cells [10]. In this work, the thermal behavior of non-degraded and degraded commercial Li-ion cells is analyzed by carrying out ARC measurements. Two different types of degradation were analyzed, storage and cycling degradation at high temperatures.

6.2 Experimental methodology

6.2.1 Li-ion cell specifications

Commercial 18650 Li-ion cells containing $LiCoO_2$ + additives as cathode active material and graphite as anode active material were used in this work. The initial

capacity of the cells was 2550 mAh. The electrolyte consisted of a solution of 1 M of $LiPF_6$ in ethylene carbonate and dimethyl carbonate (1:1, w/w). The information of the composition of electroactive materials and electrolyte was taken from the corresponding Li-ion cell data sheet.

6.2.2 Storage degradation

Li-ion cells were fully charged (4.2 V) and stored in a thermostatic chamber (ETAC, FL414P) at 80 °C for 1 week.

6.2.3 Cycling degradation

Li-ion cells were charged and discharged in a thermostatic chamber at 80 °C for 1 week. The cells were charged and discharged following a constant current process with a charging/discharging current of 510 mA. During charging, the cells were charged until 4.2 V. The cells were discharged to 25% depth of discharge (DOD). The total charging/discharging cycles were 48.

6.2.4 Accelerating rate calorimetry

Before carrying out the ARC measurements, the cells were charged to the desired state of charge using a battery tester (KIKUSUI, PFX2011). Thermal runaway tests were carried out using an accelerating rate calorimeter (ARC) 2000^{TM} Columbia Scientific Industries. The cells were set to the desired SOC and placed inside the ARC cavity. To set the cells to the desired SOC, the cells were fully charged and then discharged to the corresponding SOC using a discharging current of 0.2 C following a constant current (CC) process.

To record the temperature of the cell, a thermocouple was placed on the surface of this. The calorimetry measurements were conducted following a Heat-Wait-Search method. During the heat-step, the cell is heated in periods of 5 °C follow by a

waiting-step of 30 min and a searching-step of 5 min. If during the searching-step, a self-heating with a heating rate higher than 0.05 °C min^{-1} is detected, the calorimeter shifts to adiabatic mode and tracks the cell temperature until the end the self-heating reaction. If no self-heating is detected, the next heat-step is immediately initiated .The thermal runaway measurements were carried out until surface of the cell reached a temperature of 200 °C. The ARC measurements were carried out at 0%, 25%, 50%, 75% and 100% SOC.

6.3 Results and discussion

Fig. 6.1 shows the thermal behavior of the non-degraded Li-ion cell during the ARC measurements at 0%, 25%, 50%, 75% and 100% SOCs. A temperature drop is observed at some SOCs, this drop in temperature is likely due to the volatilization of the electrolyte. A temperature drop is not observed when the heat generated by the cells is larger than the heat released by the volatilization of the electrolyte. Table 6.1 shows the onset temperatures of self-heating and thermal runway reactions of the non-degraded cell at different SOCs. The onset temperatures decrease by increasing the state of charge. The differences of the onset temperatures of the self-heating reactions are due to the influence of the state of charge on the thermal stability of the electroactive materials, where highly delithiated electroactive materials become more reactive [11, 12]. At 25%, 50%, 75% and 100% SOCs, self-heating reactions were followed by a thermal runaway behavior.

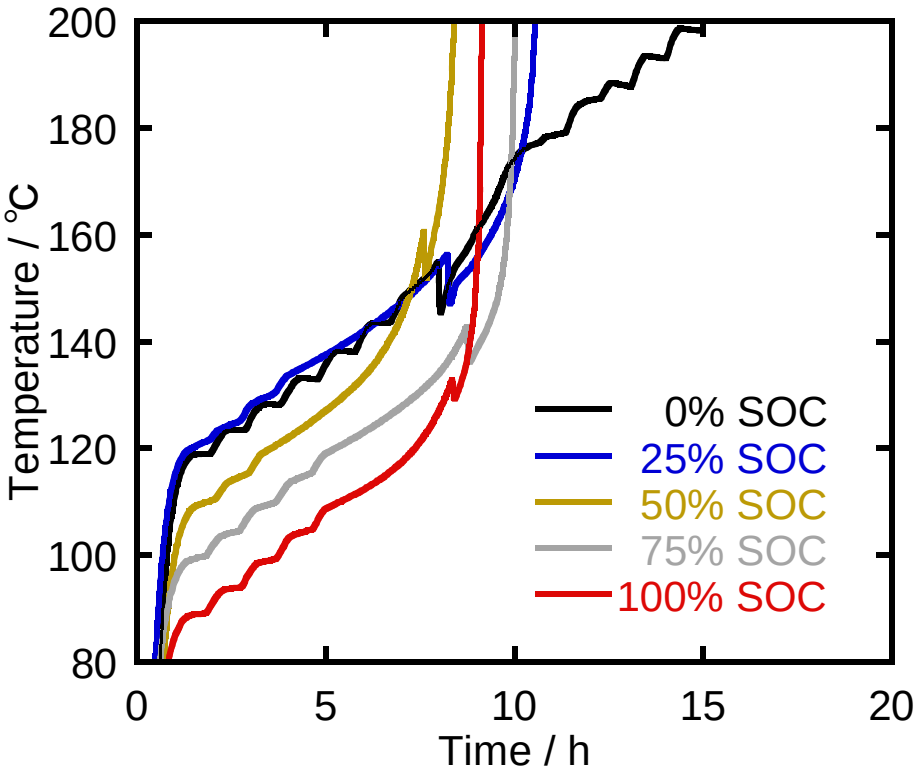

Fig. 6.1 ARC measurements of non-degraded cells at 0%, 25%, 50%, 75% and 100% SOC.

Table 6.1 Onset temperatures of self-heating and thermal runaway reactions of non-degraded cells

SOC (%)	**Onset temperature of self-heating (°C)**	**Onset temperature of Thermal runaway (°C)**
0	152.1	-
25	130.2	173.4
50	110.7	172.1
75	121.2	165.3
100	100.0	144.9

Figure 6.2 shows the thermal behavior of the degraded cells during the ARC measurements at 0%, 25%, 50%, 75% and 100% SOCs. Table 6.2 shows the onset temperatures of self-heating and thermal runway reactions. At 0% SOC, self-heating and thermal runaway reactions are observed.

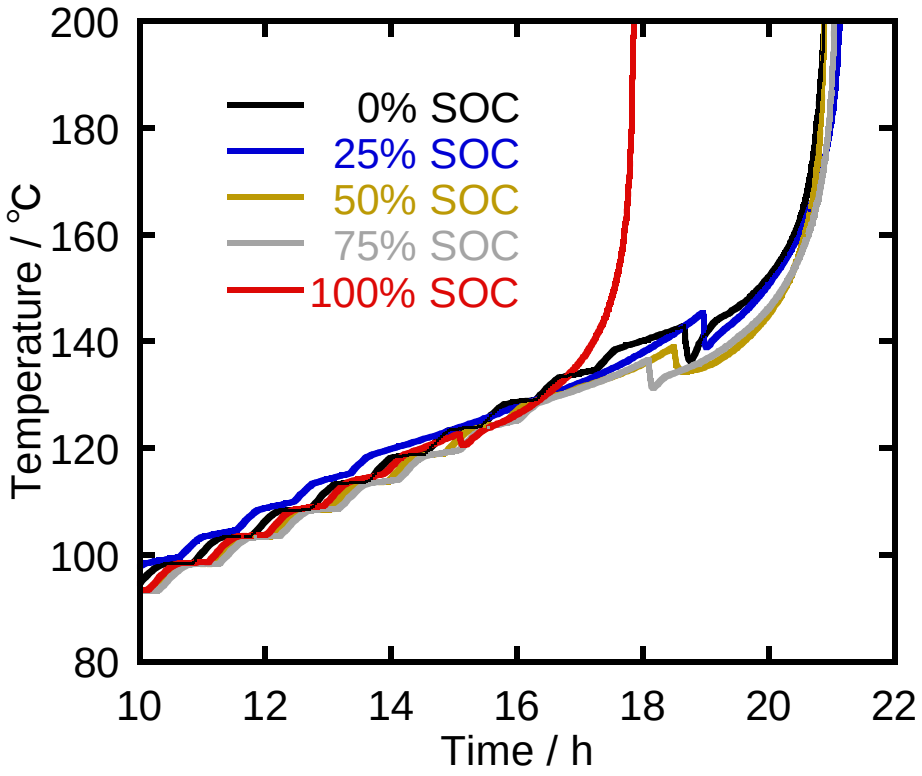

Fig. 6.2 ARC measurements of degraded cells at 0%, 25%, 50%, 75% and 100% SOC.

Table 6.2 Onset temperatures of self-heating and thermal runaway reactions of degraded cells

SOC (%)	Onset temperature of self-heating (°C)	Onset temperature of Thermal runaway (°C)
0	140.5	168.2
25	120.3	173.9
50	129.8	163.8
75	125.3	167.6
100	115.1	153.4

Figure 6.3 shows the thermal behavior of the degraded cells during the ARC measurements at 0%, 25%, 50%, 75% and 100% SOCs. Table 6.3 shows the onset temperatures of self-heating and thermal runway reactions. At 0% SOC, self-heating and thermal runaway reactions are observed.

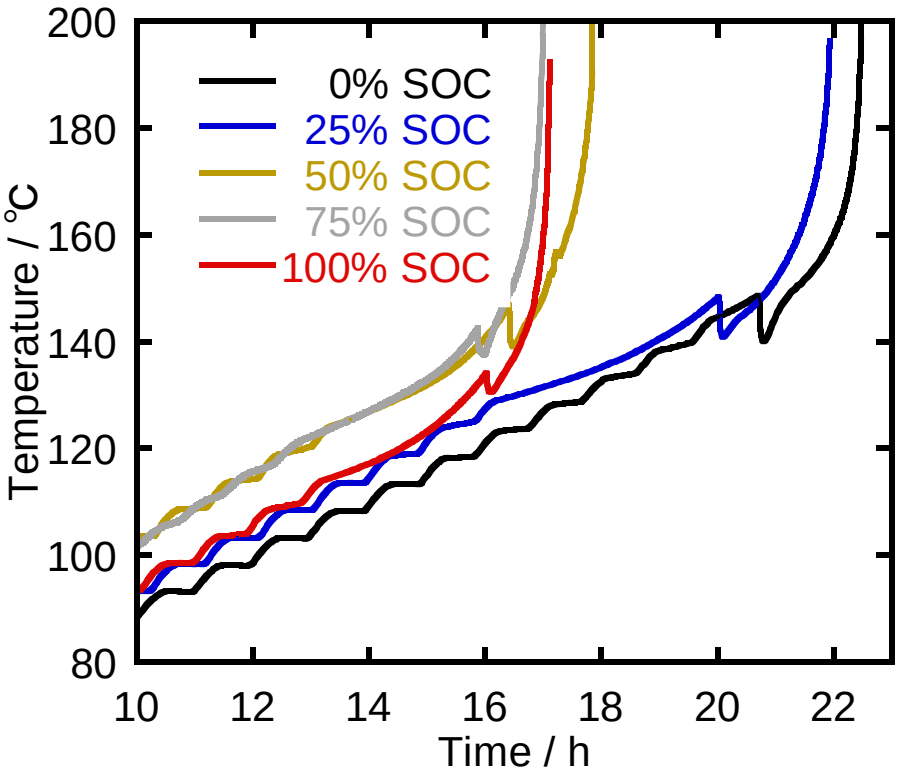

Fig. 6.3 ARC measurements of cycling degraded cells at 0%, 25%, 50%, 75% and 100% SOC.

Table 6.3 Onset temperatures of self-heating and thermal runaway reactions of cycling degraded cells

SOC (%)	Onset temperature of self-heating (°C)	Onset temperature of Thermal runaway (°C)
0	149.2	169.9
25	130.4	171.7
50	124.2	171.1
75	121.7	161.1
100	116.5	148.9

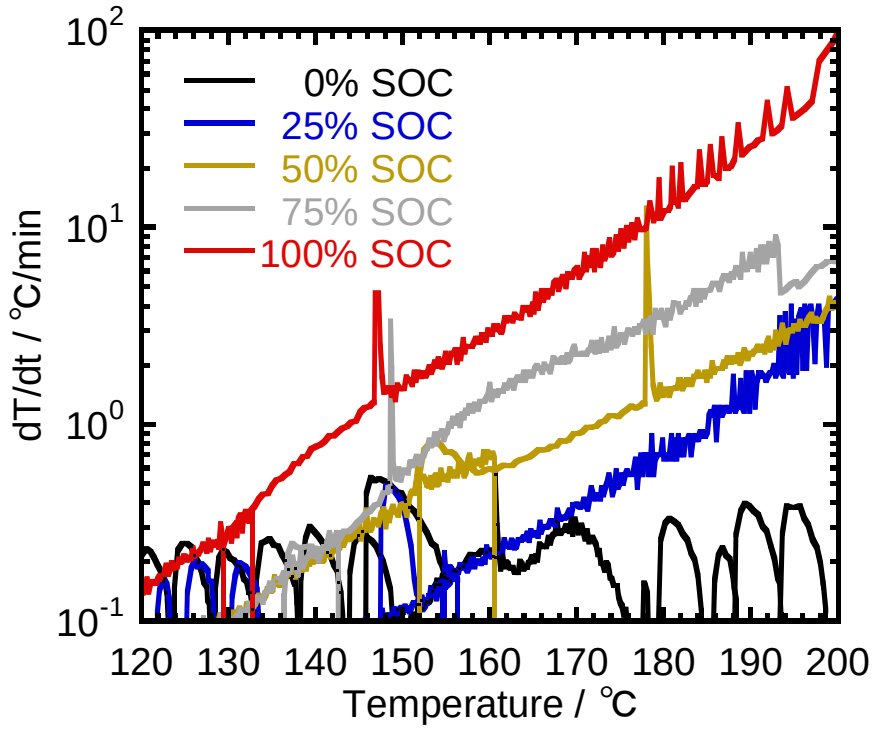

Fig. 6.4 Heating rate vs. temperature of non-degraded cells at 0%, 25%, 50%, 75% and 100% SOC.

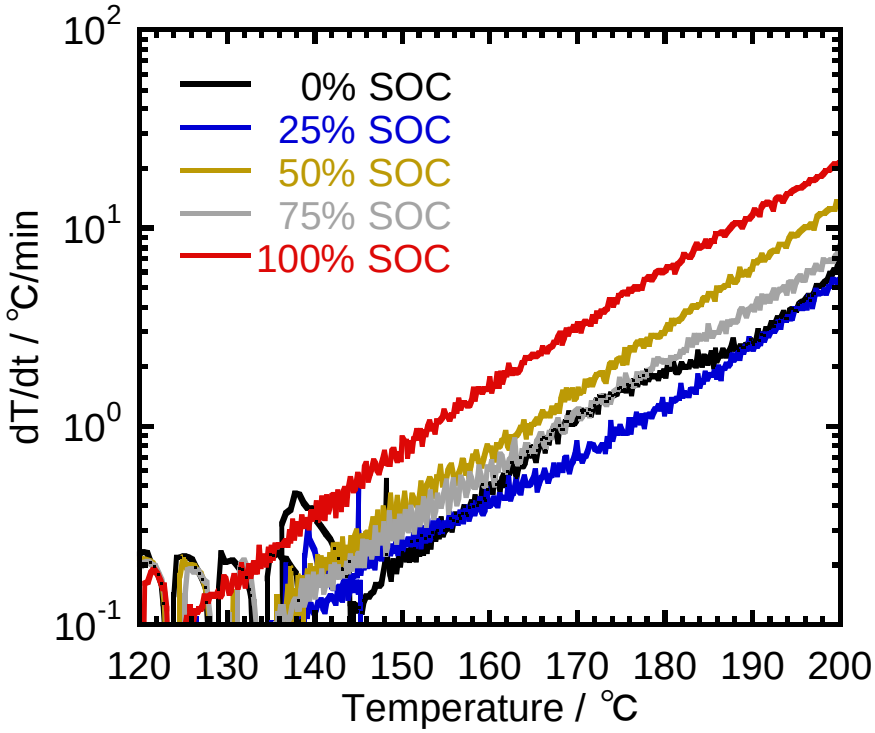

Fig. 6.5 Heating rate vs. temperature of degraded cells at 0%, 25%, 50%, 75% and 100% SOC.

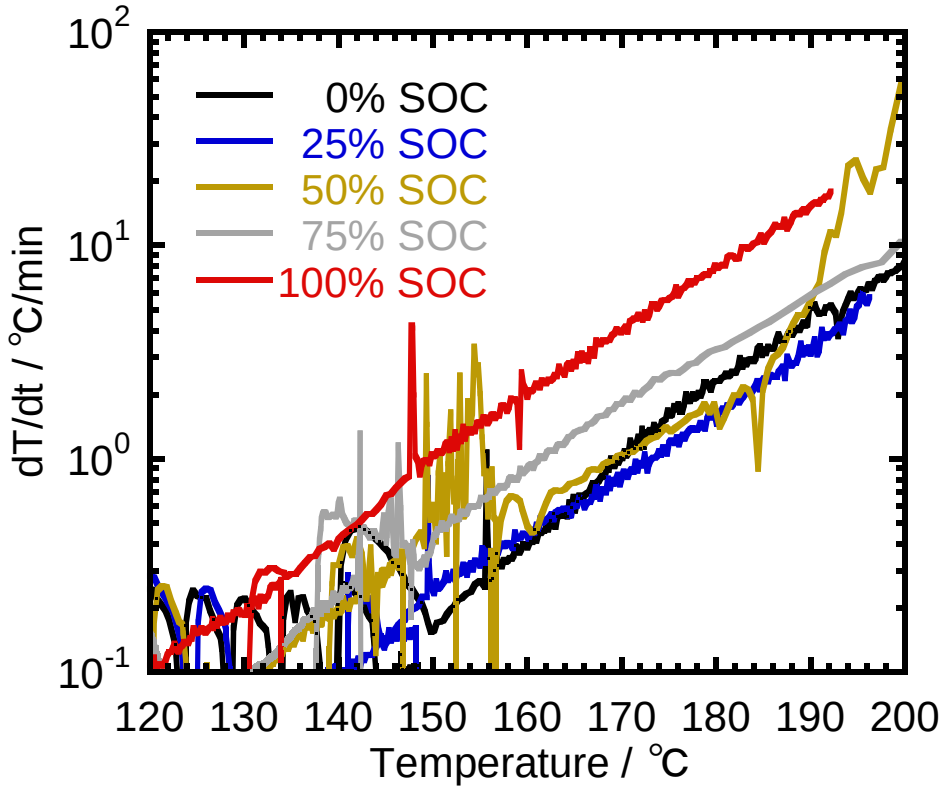

Fig. 6.6 Heating rate vs. temperature of cycling degraded cells at 0%, 25%, 50%, 75% and 100% SOC.

Figures 6.4 - 6.6 show the heating rate vs. temperature of the non-degraded and degraded cells at 0%, 25%, 50%, 75% and 100% SOC. By comparing the heating rates of these cells, it is observed that the cells before degradation release more heat than the cells after degradation. The capacity of the cells after degradation decreased an average of 54%, this drop in capacity is probable related with the amount of heat released by the cells after degradation. When the heating rate of a cell is higher than 0.05 °C min^{-1}, it is considered that a self-heating reaction has started. A thermal runaway behavior takes place when the self-heating rate of a cell is higher than 1 °C min^{-1} [2].

Non-degraded cells exhibited a thermal runaway behavior from 25% to 100% SOC, while the cells after degradation exhibited a thermal runaway behavior form 0%

to 100% SOC. Fig. 6.7 shows the impedance spectra of a Li-ion cell before and after degradation at 50% SOC. An increase in the size of the spectrum is observed after degradation, indicating that the thickness of solid electrolyte interphase (SEI), generated around the anode electro active material, increased after degradation. At 0% SOC before degradation, the cell did not go to thermal runaway, while the cell after degradation went to thermal runaway. A thermal runway reaction takes place when the exothermic reactions go out of control, the exothermic reactions occur when the SEI reacts with the electroactive material or electrolyte, this process generally takes place at the anode above 120 °C [10]. In the case of the cell after degradation at 0% SOC, the increment in thickness of SEI may accelerate the self-heating reactions until thermal runaway.

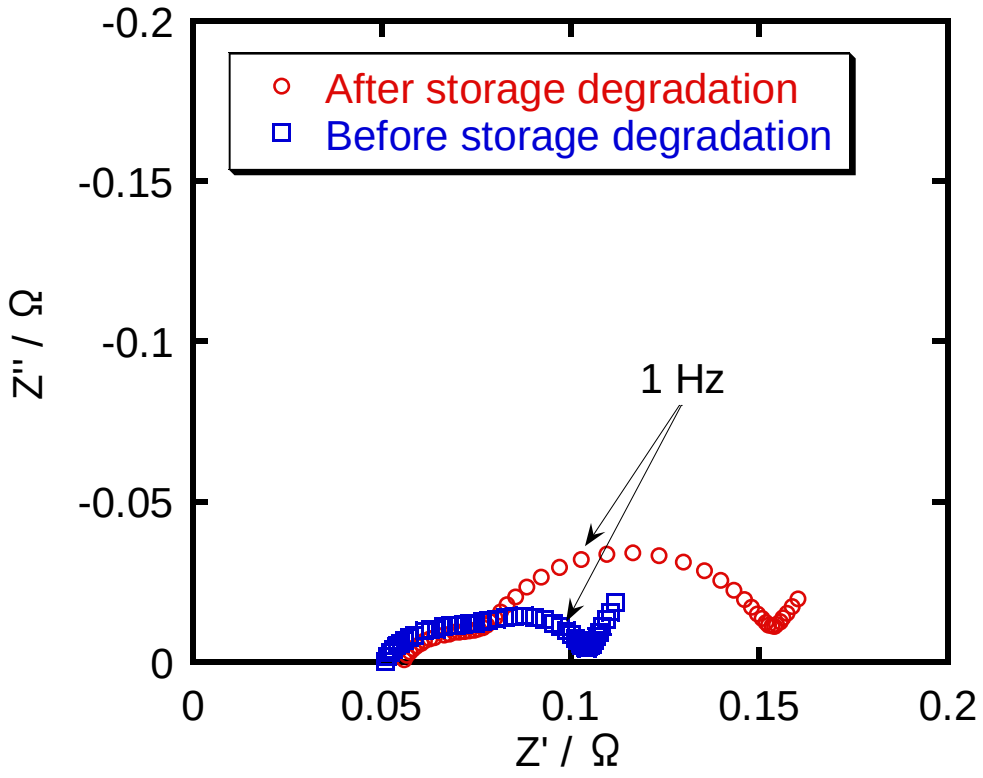

Fig. 6.7 Impedance spectra of a Li-ion secondary cell at 50% SOC before and after storage degradation.

Figs. 6.8 - 6.10 show the thermal mapping plots of non-degraded and degraded cells as a function of SOC. By summarizing the ARC results, it is possible to distinguish non-self-heating (blue bars), self-heating (yellow bars) and thermal runaway (red bars) regions as a function of temperature and SOC. In the non-self-heating region, any exothermic reaction occurs. In the self-heating region, exothermic reactions with a heating rate larger than 0.05 °C min^{-1} occur. In the thermal runaway region, the heating rate is larger than 1 °C min^{-1} [2]. These plots are useful to compare the thermal between non-degraded and degraded Li-ion cells.

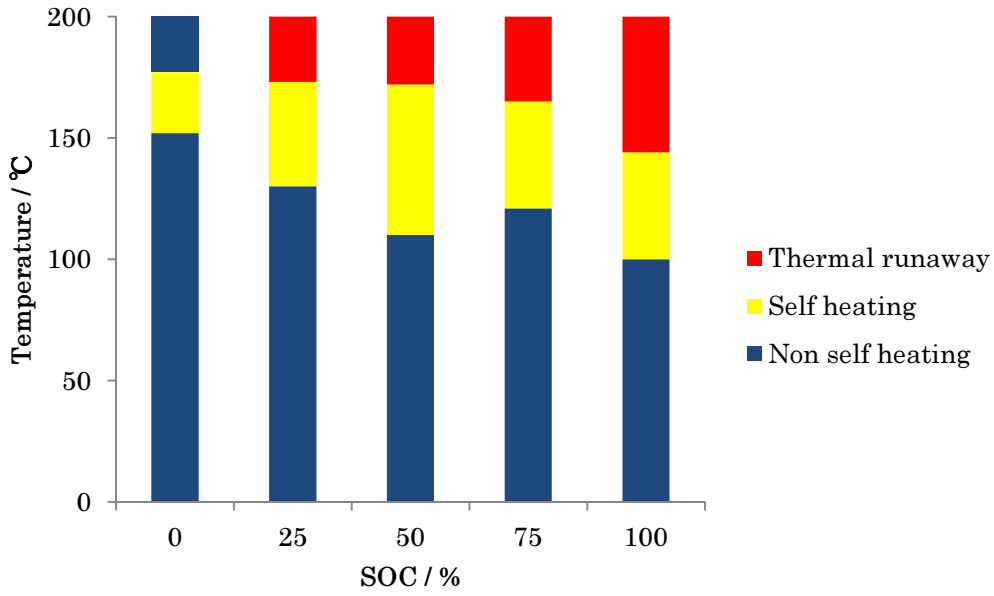

Fig. 6.8 Thermal mapping of a non-degraded cell as a function of SOC. Non-self-heating (blue), self-heating (yellow) and thermal runaway (red) regions are identified.

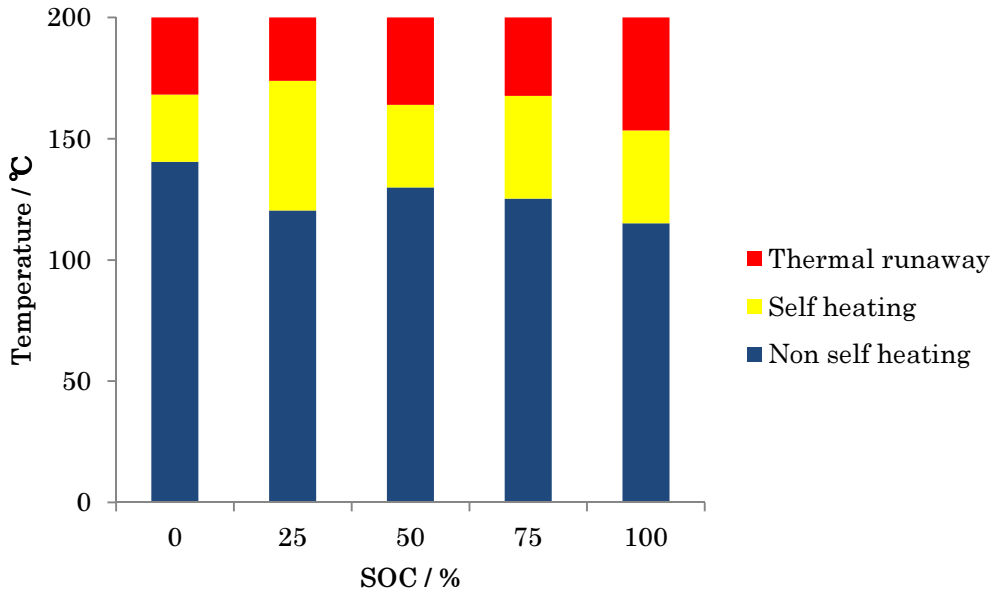

Fig. 6.9 Thermal mapping of a degraded cell as a function of SOC. Non-self-heating (blue), self-heating (yellow) and thermal runaway (red) regions are identified.

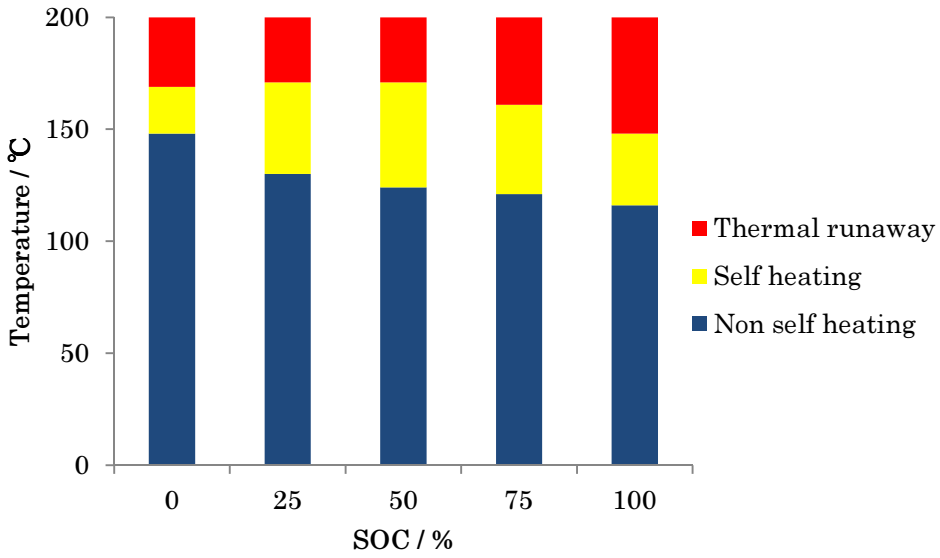

Fig. 6.10 Thermal mapping of a cycling degraded cell as a function of SOC. Non-self-heating (blue), self-heating (yellow) and thermal runaway (red) regions are identified.

By comparing the thermal mappings before and after degradation, some differences are observed at low state of charges (0% and 25% SOC). The onset temperatures of self-heating regions decrease after degradation, indicating that the cell after degradation become thermally unstable.

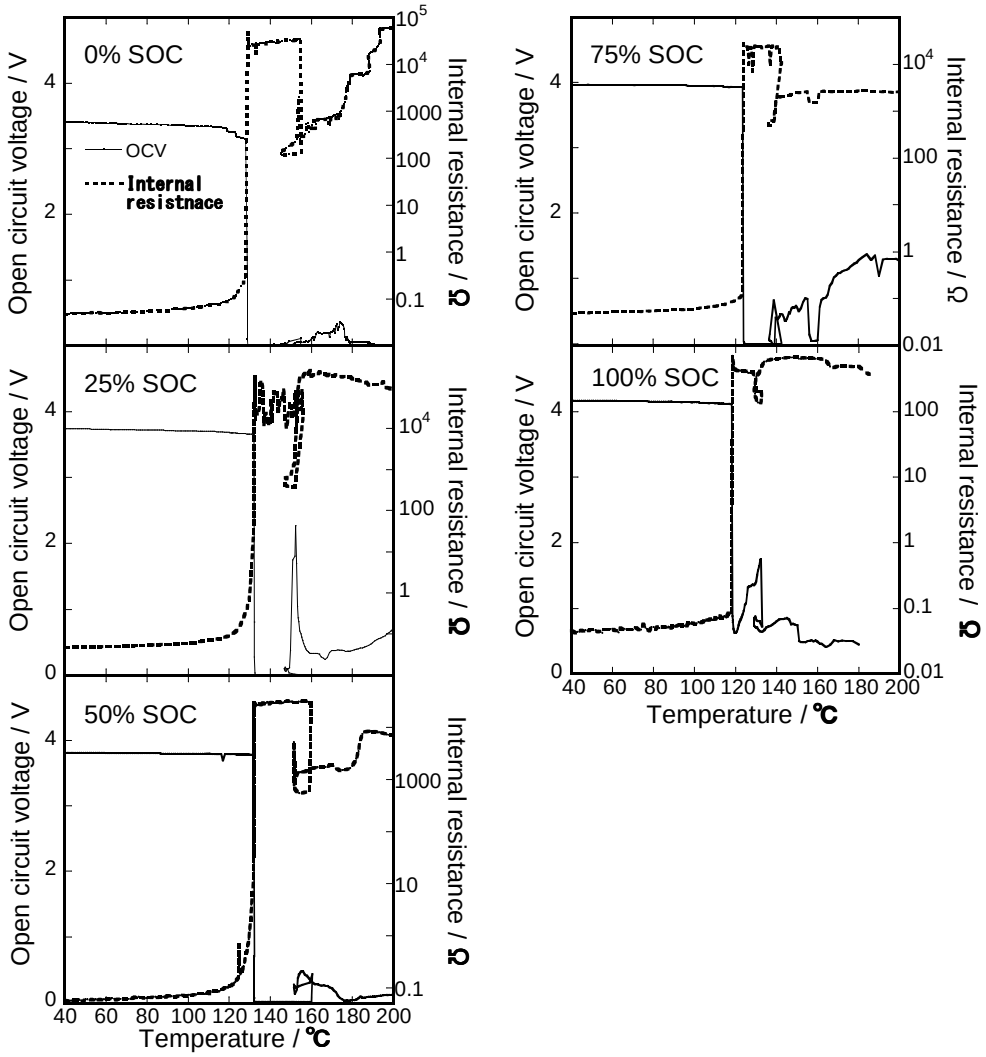

Fig. 6.11 Open circuit voltage and internal resistance of non-degraded cell during ARC measurements as a function of temperature at 0%, 25%, 50%, 75% and 100% SOC.

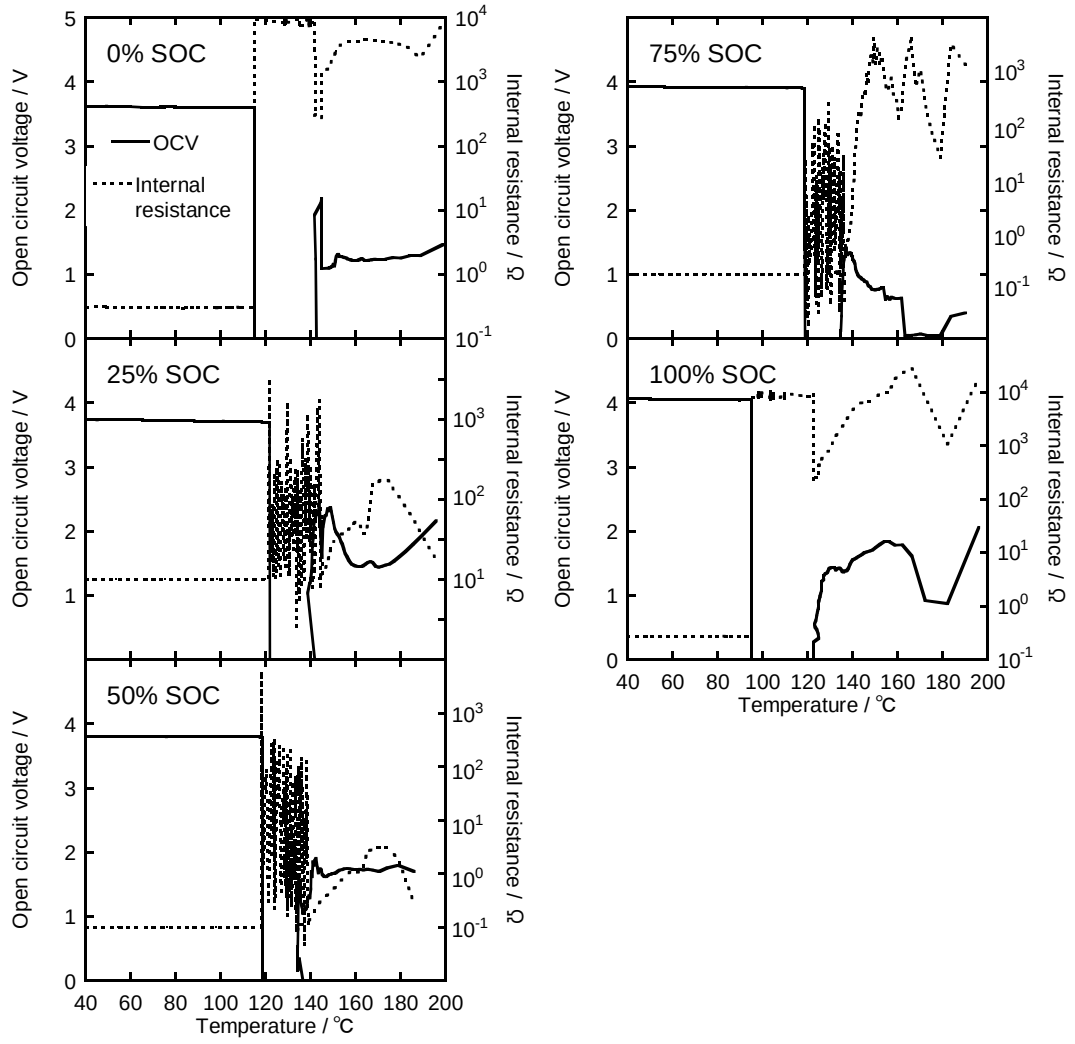

Fig. 6.12 Open circuit voltage and internal resistance of degraded cell during ARC measurements as a function of temperature at 0%, 25%, 50%, 75% and 100% SOC.

Figures 6.11 and 6.12 show the OCV and the internal resistance of the non-degraded and degraded cells as a function of temperature at 0%, 25%, 50%, 75% and 100% SOC. It is noticed that by increasing the temperature, the OCV decreases and the internal resistance increases. The OCV and the internal resistance start decreasing and increasing, respectively, at around 135 °C, this is likely due to the shutting down of the separator located between the cathode and anode materials [6,13]. A combination of

polyethylene (158 °C melting point) and polypropylene (125 °C) materials are used as separator in this work [13-16]. The separator has many tiny holes and Li-ions pass through them. A separator shuts down when the melting point of this is reached, then the tiny holes of the separator are closed and there is no Li-ion transfer between the electrodes, which causes a drop in the OCV and an increase in the internal resistance [17]. By comparing Fig. 6.11 and 6.12, some differences in the electrochemical behavior of the cells are noticed, which suggest that the state of charge and the type of cathode electroactive material are affecting the shutting down behavior of the cells.

6.4 Conclusions

By carrying out ARC measurements, the thermal behavior of non-degraded and degraded cells was compared using commercial 18650 Li-ion cells. The ARC results were used to make thermal mapping plots, where non-self-heating, self-heating and thermal runaway regions are identified as a function of state of charge and temperatures. The use of thermal mapping plots allows a practical comparison of the thermal behaviors of Li-ion cells before and after degradation. Impedance measurements showed that the SEI increase after degradation, causing that degraded cells become thermally unstable at low state of charges.

In parallel with the ARC measurements, the OCV and internal resistance of the cells were monitored. By increasing the temperature, an increase in the internal resistance and a decrease in the OCV were noticed.

References

[1] T. D. Hatchard, D. D. MacNeil, A. Basu, J. R. Dahn, J. Electrochem. Soc. 148 (2001) A755-A761.

[2] I. Uchida, H. Ishikawa, M. Mohamedi, M. Umeda, J. Power Sources 119–121(2003) 821-825.

[3] J.S. Gnanaraj, E. Zinigrad, L. Asraf, H.E. Gottlieb, M. Sprecher, D. Aurbach, Schmidt, J. Power Sources 119–121 (2003) 794-798.

[4] R.M. Spotnitz, J. Weaver, G. Yeduvaka, D.H. Doughty, E.P. Roth, J. Power Sources 163 (2007) 1080–1086.

[5] B.K. Mandal, A.K. Padhi, Z. Shi, S. Chakraborty, R. Filler, J. Power Sources 161 (2006) 1341–1345.

[6] H. Ishikawa, O. Mendoza, Y. Sone, M. Umeda, J. Power Sources 198 (2012) 236-242.

[7] C.-Y. Jhu, Y.-W. Wang, C.-Y. Wen, C.-M. Shu, Appl. Energy 100 (2012) 127-131.

[8] A. Eddahech, O. Briat, J-M. Vinassa, Energy 61 (2013) 432-439.

[9] P. Roder, N. Baba, H. Wiemhofer, J. Power Sources 248 (2014) 978-987.

[10] P. Roder, B. Stiaszny, J. C. Ziegler, N. Baba, P. Lagaly, H. Wiemhofer, J. Power Sources 268 (2014) 315-325.

[11] Y. Furushima, C. Yanagisawa, T. Nakagawa, Y. Aoki, N. Muraki, J. Power Sources 196 (2011) 2260-2263.

[12] E. P. Roth, D. H. Doughty, J. Power Sources 128 (2004) 308-318.

[13] G. Venugopal, J. Power Sources 101 (2001) 231-237.

[14] F. C. Laman, M. A. Gee, J. Denovan, J. Electrochem. Soc. 140 (1993) L51-L53.

[15] A. J. Bradley and R. E. White, J. Power Sources 70 (1998) 48-54.

[16] G. Venugopal, J. Moore, J. Howard, S. Pendalwar, J. Power Sources 77 (1999) 34-41.

[17] X. Liu, H. Kusawaka, S. Kuwajima, J. Power Sources 97-98 (2001) 661-663.

Chapter 7 "Thermal Behavior of Small and Large Laminated Li-ion secondary Cells"

7.1 Introduction

There are safety concerns related to the upsizing of Li-ion cells and the use of oxide based cathode materials, since oxygen release from the cathode material at high temperatures can accelerate the combustion reactions in the cell driving its components into fire or explosion. The thermal analysis of Li-ion secondary cells with different capacities is important for ensuring their safety and reliability.

The use of accelerating rate calorimetry (ARC) allows the thermal analysis of Li-ion cells [1-9]. In this work, the thermal behavior of laminated Li-ion cells with different capacities, 30 mAh and 700 mAh, are analyzed at different state of charges.

7.2 Experimental methodology

7.2.1 Li-ion cell specifications

Two laminated Li-ion cells with different capacities were used in this work. The cells used $LiCoO_2$ as cathode active material and graphite as anode active material. The electrolyte consisted of a solution of 1 M of $LiPF_6$ in ethylene carbonate and dimethyl carbonate (1:1, w/w). The capacity of the first cell is 30 mAh and the capacity of the second is 700 mAh.

7.2.2 Accelerating rate calorimetry

Before carrying out the ARC measurements, the cells were charged to the desired state of charge using a battery tester (KIKUSUI, PFX2011). Thermal runaway tests were carried out using an accelerating rate calorimeter (ARC) 2000^{TM} Columbia Scientific Industries. The cells were set to the desired SOC and placed inside the ARC

cavity. The cells were analyzed at 25% and 75% SOC.

To record the temperature of the cell, a thermocouple was placed on the surface of this. The calorimetry measurements were conducted following a Heat-Wait-Search method. During the heat-step, the cell is heated in periods of 5 °C follow by a waiting-step of 30 min and a searching-step of 5 min. If during the searching-step, a self-heating with a heating rate higher than 0.05 °C min^{-1} is detected, the calorimeter shifts to adiabatic mode and tracks the cell temperature until the end the self-heating reaction. If no self-heating is detected, the next heat-step is immediately initiated. The thermal runaway measurements were carried out until surface of the cell reached a temperature of 200 °C.

7.3 Results and discussion

Figure 7.1 shows the thermal behavior of the 30 mAh cells during the ARC measurements at 25% and 75% SOCs. Table 7.1 shows the onset temperatures of self-heating reactions of the 30 mAh. The onset temperatures decrease by increasing the state of charge.

Table 7.1 Onset temperatures of self-heating reactions of 30mAh cells.

SOC (%)	Onset temperature of self-heating (°C)	Onset temperature of Thermal runaway (°C)
25	172.5	-
75	179.7	-

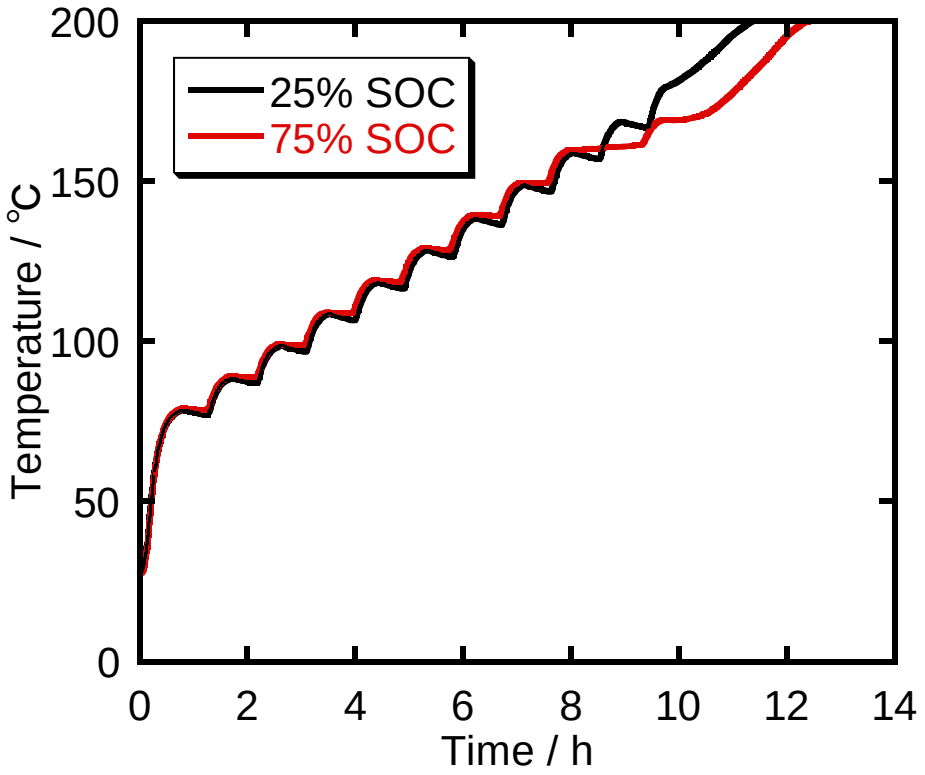

Fig. 7.1 ARC measurements of 30 mAh cells at 25% and 100% SOC.

Figure 7.2 shows the thermal behavior of the 700 mAh cells during the ARC measurements at 25% and 75% SOCs. Table 7.2 shows the onset temperatures of self-heating reactions of the 700 mAh. The onset temperatures decrease by increasing the state of charge.

Table 7.2 Onset temperatures of self-heating reactions of 700mAh cells.

SOC (%)	**Onset temperature of self-heating (°C)**	**Onset temperature of Thermal runaway (°C)**
25	144.3	-
75	133.3	189.9

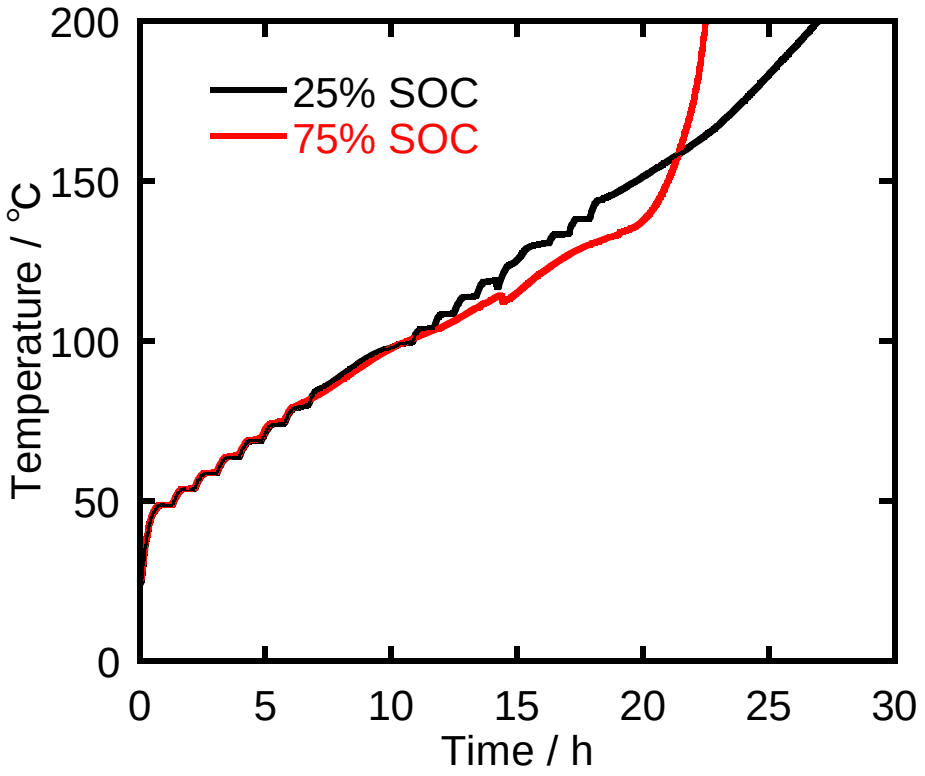

Fig. 7.2 ARC measurements of 700 mAh cells at 25% and 100% SOC.

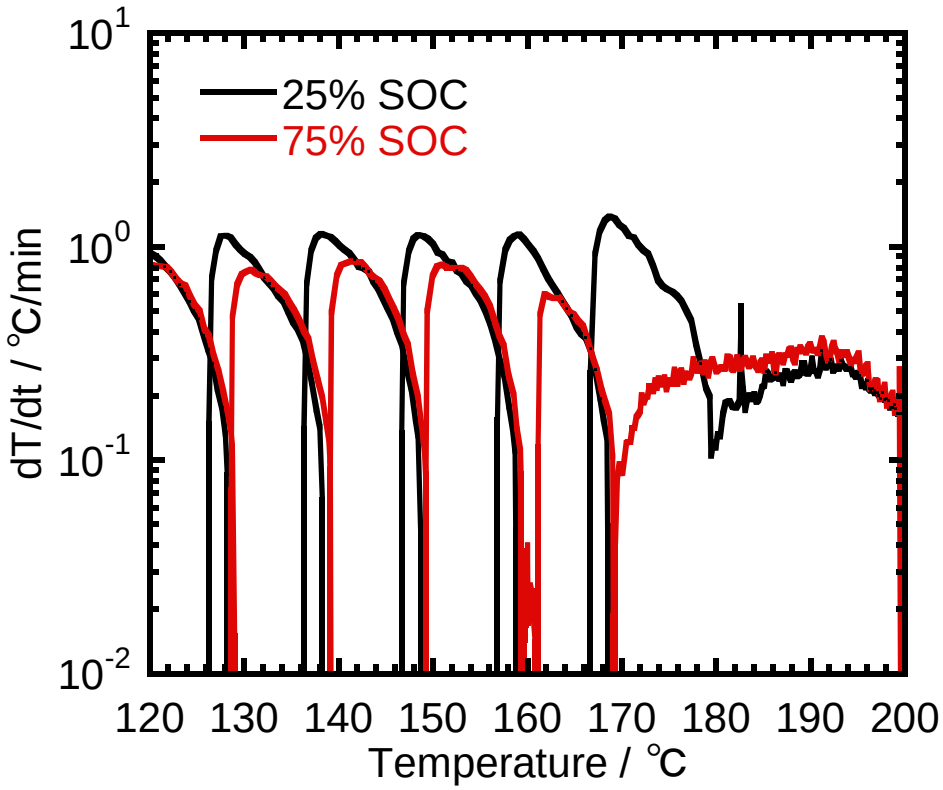

Fig. 7.3 Heating rate vs. temperature of 30 mAh cells at 25% and75% SOC 100%.

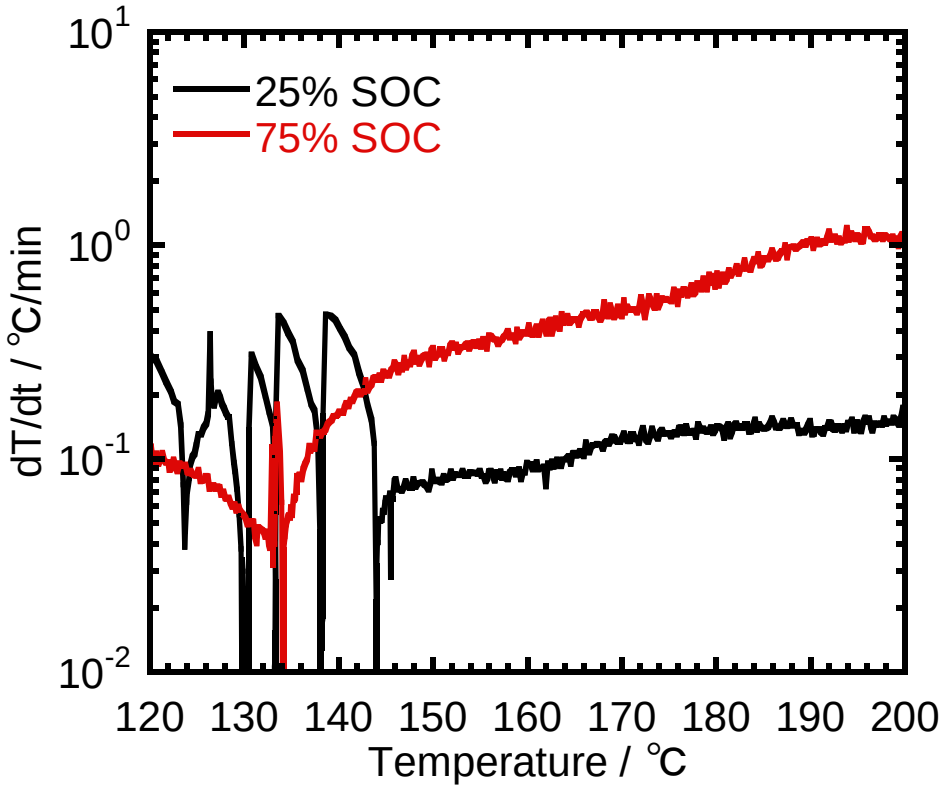

Fig. 7.4 Heating rate vs. temperature of 700 mAh cells at 25% and75% SOC 100%.

Figures 7.3 and 7.4 show the heating rate vs. temperature of the 30 mAh and 700 mAh Li –ion cells at 25% and 75% SOC. Li-ion cells with a capacity of 30 mAh did not exhibit a thermal runaway behavior. 700 mAh Li-ion cells release more heat and a thermal runaway behavior was observed in the case of 75% SOC. A Li-ion cell goes to thermal runaway, when this generates more heat than what can be dissipated [3, 8]. This results show that capacity of Li-ion cells impact the heat generation of these.

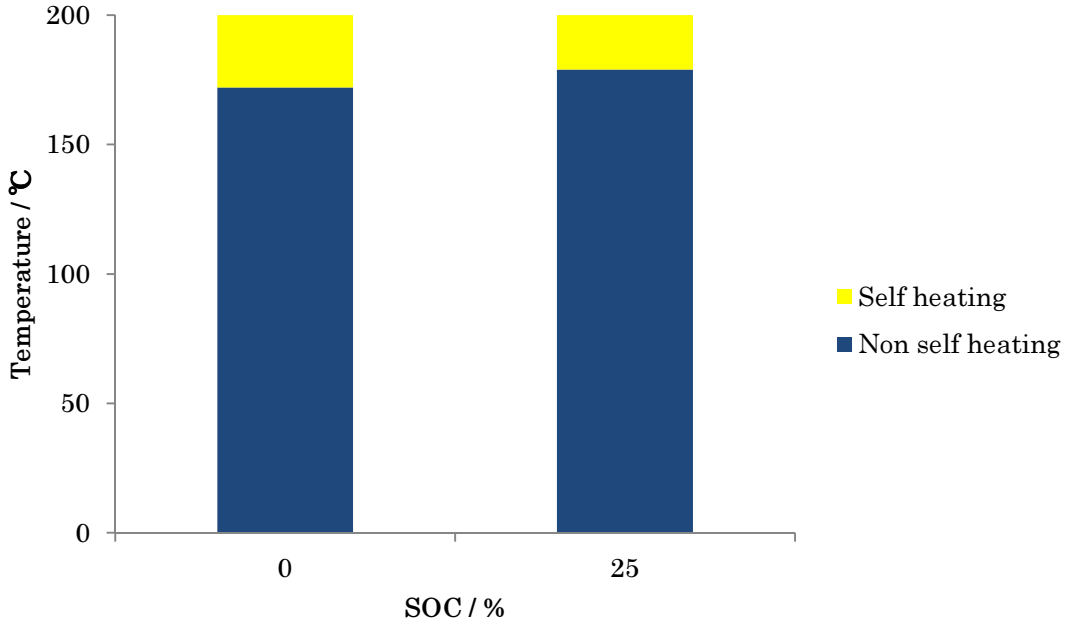

Fig. 7.5 Thermal mapping of 30 mAh Li-ion cell as a function of SOC. Non-self-heating (blue), self-heating (yellow) and thermal runaway (red) regions are identified.

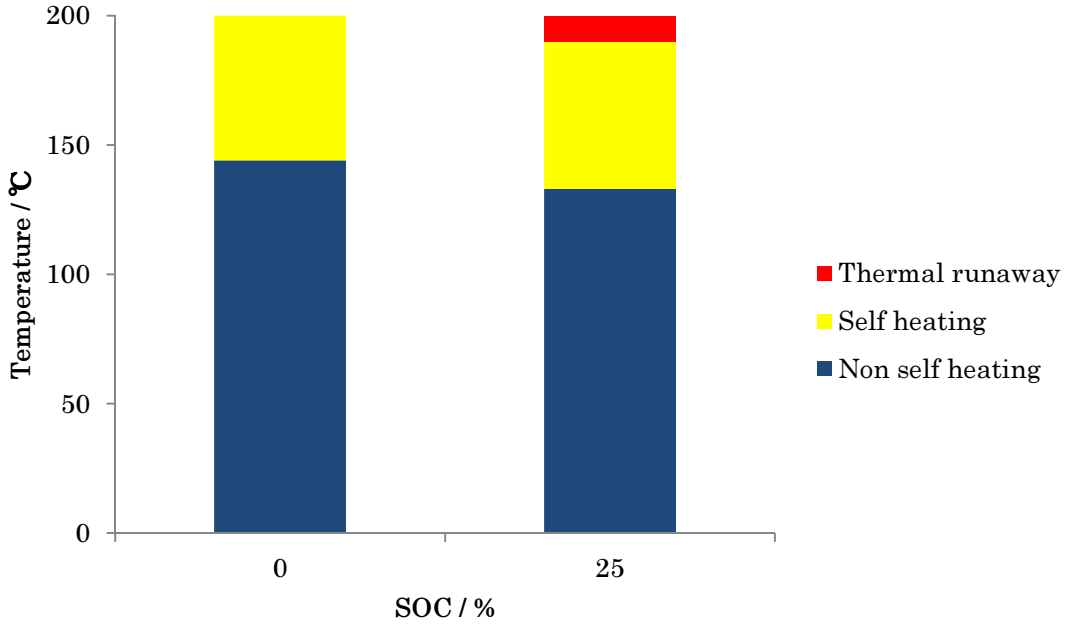

Fig. 7.6 Thermal mapping of 700 mAh Li-ion cell as a function of SOC. Non-self-heating (blue), self-heating (yellow) and thermal runaway (red) regions are identified.

Figures 7.5 and 7.6 show the thermal mapping plots of 30 mAh and 700 mAh Li-ion cells as a function of SOC. By summarizing the ARC results, it is possible to distinguish non-self-heating (blue bars), self-heating (yellow bars) and thermal runaway (red bars) regions as a function of temperature and SOC. In the case of 30 mAh cells, self-heating regions are observed without going to thermal runway. In the case of 700 mAh, self-heating regions are observed and a thermal runaway region is observed at 75% SOC. By comparing the onset temperatures of self-heating reactions of both cells, it is noticed that the self-heating reactions of 700 mAh tend to start at lower temperatures than the 30 mAh cells. This indicates that highly delithiated electroactive materials with high capacities become more reactive and tend to generate more heat that highly delithiated electroactive materials with low capacities [9, 10].

7.4 Conclusions

By carrying out ARC measurements, the thermal behavior of 30 mAh and 700 mAh Li-ion cells was compared. The ARC results were used to make thermal mapping plots, where non-self-heating, self-heating and thermal runaway regions are identified as a function of state of charge and temperatures.

700 mAh Li-ion cells are more thermally unstable than 30 mAh cells. Highly delithiated electroactive materials with high capacities tends to generate more heat than Highly delithiated electroactive materials with low capacities, and when the a Li-ion cell starts generating more heat than what can be dissipated, the cell will go to thermal runaway.

References

[1] I. Uchida, H. Ishikawa, M. Mohamedi, M. Umeda, J. Power Sources 119–121(2003) 821-825.

[2] J.S. Gnanaraj, E. Zinigrad, L. Asraf, H.E. Gottlieb, M. Sprecher, D. Aurbach, Schmidt, J. Power Sources 119–121 (2003) 794-798.

[3] B.K. Mandal, A.K. Padhi, Z. Shi, S. Chakraborty, R. Filler, J. Power Sources 161 (2006) 1341–1345.

[4] H. Ishikawa, O. Mendoza, Y. Sone, M. Umeda, J. Power Sources 198 (2012) 236-242.

[5] C.-Y. Jhu, Y.-W. Wang, C.-Y. Wen, C.-M. Shu, Appl. Energy 100 (2012) 127-131.

[6] A. Eddahech, O. Briat, J-M. Vinassa, Energy 61 (2013) 432-439.

[7] P. Roder, N. Baba, H. Wiemhofer, J. Power Sources 248 (2014) 978-987.

[8] R.M. Spotnitz, J. Weaver, G. Yeduvaka, D.H. Doughty, E.P. Roth, J. Power Sources 163 (2007) 1080–1086.

[9] Y. Furushima, C. Yanagisawa, T. Nakagawa, Y. Aoki, N. Muraki, J. Power Sources 196 (2011) 2260-2263.

[10] E. P. Roth, D. H. Doughty, J. Power Sources 128 (2004) 308-318.

Conclusions:

Conclusions of chapters 3 to 7 are summarized here:

Chapter 3 “Kinetic Analysis of Graphitized-Carbon-Based Electrode Reactions in Lithium-ion Secondary Cells Before and After Cycling Degradation”

The process of lithium-ion insertion/deinsertion into graphitized carbon was analyzed at different temperatures and state of charge by carrying out EIS measurements using a Li-ion secondary cell incorporating a reference electrode. The activation energy of Li-ion conduction, Li-ion desolvation and charge transfer reactions were analyzed before and after cycling degradation as a function of SOC and anode potential. The results were evaluated using the staging process of graphite.

Charge transfer, Li-ion conduction and Li-ion desolvation/solvation reactions originating from SEI were analyzed as a function of SOC and anode electrode potential. The activation energy of charge transfer depends on SOC and anode potential, indicating that the staging process of graphite is affecting the charge transfer reaction. On the other hand, the activation energies of Li-ion conduction and Li-ion solvation/desolvation are independent on SOC and anode potential, showing that the staging process of graphite does not affect the Li-ion conduction and Li-ion solvation/desolvation reactions.

Chapter 4 “Kinetic Comparison of $LiCoO_2$ and $LiMn2O_4$ Cathode Material Reactions in Li-ion Secondary Cells Incorporating a Reference Electrode”

By carrying out EIS and chronopotentiometric measurements, using Li-ion secondary cells incorporating a reference electrode, the kinetic characteristics of

$LiCoO_2$ and $LiMn_2O_4$ at different SOCs and temperatures were studied. It was to analyze kinetic characteristics of $LiCoO_2$ and $LiMn_2O_4$ as a function of cathode potential. The kinetic behavior of Li-ion conduction, Li-ion solvation/desolvation and charge transfer reactions of $LiCoO_2$ and $LiMn_2O_4$ and its dependency on the structural changes of cathode materials are studied. The charge transfer and Li-ion conduction reactions exhibit a dependency on the structural changes of cathode materials, while Li-ion solvation/desolvation reactions do not.

According to the behavior of reaction rate constant for Li-ion conduction reactions of $LiCoO_2$ and $LiMn_2O_4$, the SEI generated around $LiCoO_2$ electroactive material seems to be more thermally sensible than the one generated at $LiMn_2O_4$.

Chapter 5 “Cathode Material Comparison of Thermal Runaway Behavior of Li-ion Cells at Different State of Charges Including Over Charge”

By carrying out ARC measurements, the thermal behavior of $LiCoO_2$ and $LiMn_2O_4$ was compared using 18650 Li-ion cells. The ARC results were used to make thermal mapping plots, where non-self-heating, self-heating and thermal runaway regions are identified as a function of state of charge and temperatures. The use of thermal mapping plots allows a practical comparison of the thermal behaviors of the cells. The cell using $LiCoO_2$ as cathode material was found to be more thermally unstable than the cell using $LiMn_2O_4$. Both cathode materials exhibited a thermal runaway behavior at overcharge, however, the onset temperature for $LiMn_2O_4$ was higher than that of $LiCoO_2$, suggesting that $LiMn_2O_4$ is relatively stable when it is highly delithiated.

In parallel with the ARC measurements, the OCV and internal resistance of the

cells were monitored. By increasing the temperature, an increase in the internal resistance and a decrease in the OCV were noticed.

Chapter 6 “Thermal Runaway Behavior of Degraded and Non-degraded Commercial 18650 Li-ion Secondary Cells”

By carrying out ARC measurements, the thermal behavior of non-degraded and degraded cells was compared using commercial 18650 Li-ion cells. The ARC results were used to make thermal mapping plots, where non-self-heating, self-heating and thermal runaway regions are identified as a function of state of charge and temperatures. The use of thermal mapping plots allows a practical comparison of the thermal behaviors of Li-ion cells before and after degradation. Impedance measurements showed that the SEI increase after degradation, causing that degraded cells become thermally unstable at low state of charges.

In parallel with the ARC measurements, the OCV and internal resistance of the cells were monitored. By increasing the temperature, an increase in the internal resistance and a decrease in the OCV were noticed.

Chapter 7 “Thermal Behavior of Small and Large Laminated Li-ion secondary Cells”

By carrying out ARC measurements, the thermal behavior of 30 mAh and 700 mAh Li-ion cells was compared. The ARC results were used to make thermal mapping plots, where non-self-heating, self-heating and thermal runaway regions are identified as a function of state of charge and temperatures.

700 mAh Li-ion cells are more thermally unstable than 30 mAh cells. Highly delithiated electroactive materials with high capacities tends to generate more heat than

Highly delithiated electroactive materials with low capacities, and when the a Li-ion cell starts generating more heat than what can be dissipated, the cell will go to thermal runaway.

In this work, electrochemical and thermal properties of different types of Li-ion secondary cells were obtained at different state of degradation and state of charges by using electrochemical impedance spectroscopy and accelerating rate calorimetry.

According to the obtained results, the methodology used in this research can be useful to analyze the state of degradation and thermal behavior of Li-ion cells under extreme conditions. The proposed methodology can be applied to develop safe Li-ion cells with improved electrochemical and thermal properties to power large applications.

Further analysis on the thermal properties of electroactive materials should be carried out to analyze the impact of Li-ion cell degradation on the thermal stability of these materials. Entropy change analysis of electroactive materials before and after degradation could be useful to study the thermal stability of these materials.

List of papers and conferences

Papers:

- O. S. Mendoza-Hernandez, H. Ishikawa, Y. Nishikawa, Y. Maruyama, M. Umeda, *Cathode Material Comparison of Thermal Runaway Behavior of Li-ion Cells at Different State of Charges Including Over Charge*, Journal of Power Sources 280 (2015) 499-504.

- O. S. Mendoza-Hernandez, H. Ishikawa, Y. Nishikawa, Y. Maruyama, Y. Sone, M. Umeda, *Electrochemical Impedance Study of $LiCoO_2$ Cathode Reactions in a Lithium ion Cell Incorporating a Reference Electrode*, Journal of Solid State Electrochemistry (2015) DOI 10.1007/s10008-015-2741-y

- O. S. Mendoza-Hernandez, H. Ishikawa, Y. Nishikawa, Y. Maruyama, Y. Sone, M. Umeda, *State of Charge Dependency of Graphitized-Carbon-Based Reactions in a Lithium-ion Secondary Cell Studied by Electrochemical Impedance Spectroscopy*, Electrochimica Acta 131 (2014) 168-173.

Reference papers:

- H. Ishikawa, O. Mendoza, Y. Nishikawa, Y. Maruyama, M. Umeda, *Thermal Characteristics of Lithium ion Secondary Cells in High Temperature Environments Using an Accelerating Rate Calorimeter*, Journal of Renewable and Sustainable Energy 5 (2013) 043122.

- H. Ishikawa, Y. Nishikawa, O. Mendoza, Y. Maruyama, Y. Sone, M. Umeda, *Chronopotentiometric Investigation of Anode Deterioration in Lithium Ion Secondary Cell Incorporating Reference Electrode*, Electrochemistry 80(10) (2012) 762-764.

- H. Ishikawa, O. Mendoza, Y. Sone, M. Umeda, *Study of Thermal Deterioration of Lithium Ion Secondary Cells Using an Accelerating Rate Calorimeter and AC Impedance*, Journal of Power Sources 198 (2012) 236-242.

Conferences:

- "*Activation Energy Evaluation of Different Cathode Materials Used in Li-ion Secondary Cells*", 62nd Annual Meeting of the International Society of Electrochemistry, September 11-14, 2011. Niigata, Japan.

- *"Comparison of Thermal Runaway Behavior of Lithium Ion Secondary Cells Using Different Cathode Materials"*, 79th Spring meeting of The Electrochemical Society of Japan, March 29-31, 2012. Hamamatsu, Shizuoka, Japan.

- *"Electrochemical Impedance Spectroscopy Study of Cathode and Anode Reactions in a Three Electrode Lithium Ion Secondary Cell"*, 79th Spring meeting of The Electrochemical Society of Japan, March 29-31, 2012. Hamamatsu, Shizuoka, Japan.

- *"AC Impedance Study of The Active Materials Reactions in a Three Electrode Lithium Ion Secondary Cell"*, Pacific Rim Meeting on Electrochemical and Solid-State Science, October 7-12, 2012. Honolulu, Hawaii, USA.

- *"Chronopotentiometric Investigation of Anode Deterioration in Lithium Ion Secondary Cells Incorporating a Reference Electrode"*, Pacific Rim Meeting on Electrochemical and Solid-State Science, October 7-12, 2012. Honolulu, Hawaii, USA.

- *"Thermal Runaway Behavior of Lithium Ion Secondary Cells at Different State of Charges Including Overcharge"*, The 53rd Battery Symposium in Japan, November 14-16, 2012. Fukuoka, Japan.

- *"AC Impedance Study of Cathode and Anode Reactions Using a Three Electrode Lithium Ion Secondary Cell"*, The 53rd Battery Symposium in Japan, November 14-16, 2012. Fukuoka, Japan.

- *"Comparison of the $LiCoO_2$ and $LiMn_2O_4$ Reactions of a Three Electrode Li-ion Cell Using AC Impedance Measurements"*, 80th Spring Meeting of The Electrochemical Society of Japan, March 29-31, 2013. Sendai, Miyagi, Japan.

- *"Electrochemical Impedance Spectroscopy Study of Cathode Reactions of a $LiCoO_2$-Graphite Cell"*, 9th International Symposium on Electrochemical Impedance Spectroscopy, June 16-21, 2013. Okinawa, Japan.

- *"Evaluation of Different Cathode Materials Used in Li-ion Cells Incorporating a Reference Electrode"*, 64th Annual Meeting of the International Society of Electrochemistry, September 8-13, 2013. Santiago de Queretaro, Mexico.

- *"Thermal Analysis of Degraded 18650 Li-ion Secondary Cells Using an Accelerating Rate Calorimeter"*, The 54rd Battery Symposium in Japan, October 7-9, 2013. Osaka, Japan.

- *"Thermal Behavior of Degraded and Non-degraded 18650 Li-ion Secondary Cells Measured by Accelerating Rate Calorimetry"*, 81th Spring Meeting of The Electrochemical Society of Japan, March 29-31, 2014. Osaka, Japan.

- *"Thermal Analysis of Lithium Ion Secondary Cells Before and After Degradation"*, The 3rd International GIGAKU Conference, June 20-22, 2014. Nagaoka, Niigata, Japan.

- *"Thermal Behavior of Degraded and Non-degraded 18650 Li-ion Secondary Cells Measured by Accelerating Rate Calorimetry"*, The 55rd Battery Symposium in Japan, November 19-21, 2014. Kyoto, Japan.

Motivation:

Our planet is facing environmental problems and I want to contribute to the solution of these problems by developing technology that helps to keep a balance between comfort and nature. The increase of world population and urbanization can represent a threat to the global environment and a shortage of limited natural resources if appropriate measures are not taken.

The combination of natural sources of energy with energy storage devices is an excellent alternative to reduce the emissions generated by traditional power generation systems. Li-ion secondary cells have dominated the field of advanced power sources and have replaced the use of other batteries, particularly in the case of powering large applications such as electric vehicles (EV) or hybrid electric vehicles (HEV).

A wider spread use of EVs and HEVs depends on the development of Li-ion secondary cells. These cells require a long cycle and calendar life, high performance and safe operation. The safety of the cells should not be influenced by the degradation of these, but there are still some concerns regarding to the performance of degraded Li-ion cells.

This research studies the electrochemical and thermal properties of different types of Li-ion secondary cells with the aim of developing safe Li-ion cells with a long calendar life and high performance.

Acknowledgements

This work would not have been possible without the guidance, help and support of many persons who in one way or another contributed in the preparation of my research. I would like to thank everyone who has helped me along the way. Particularly: Professor Minoru Umeda for receiving me in his laboratory and providing me an opportunity to conduct my research under his guidance, Professor Yoshitsugu Sone, for his kind support and guidance, Professor Sayoko Shironita, for her kind support and help, my present and past lab mates for their support, particularly: Ishikawa san, Nishikawa san, Maruyama san, Taniguchi san and Konakawa san.

I would like to thank professors Yukiko Takahashi, Hiroshi Matsubara, Tatsuro Imabuko and Nobuo Saito for their comments and for having evaluated my work.

I would like to thank Doctoral Safety Paradigm Course professors for their kind support and for the opportunity to do an internship in Germany.

I would also like to thank the Ministry of Education, Culture, Sports, Science and Technology of Japan for having supported my studies in Japan.

Lastly, I would like to thank my wife, Kanae, my little Nati and my family for their unconditional love and support.